Charged Current Interactions at HERA

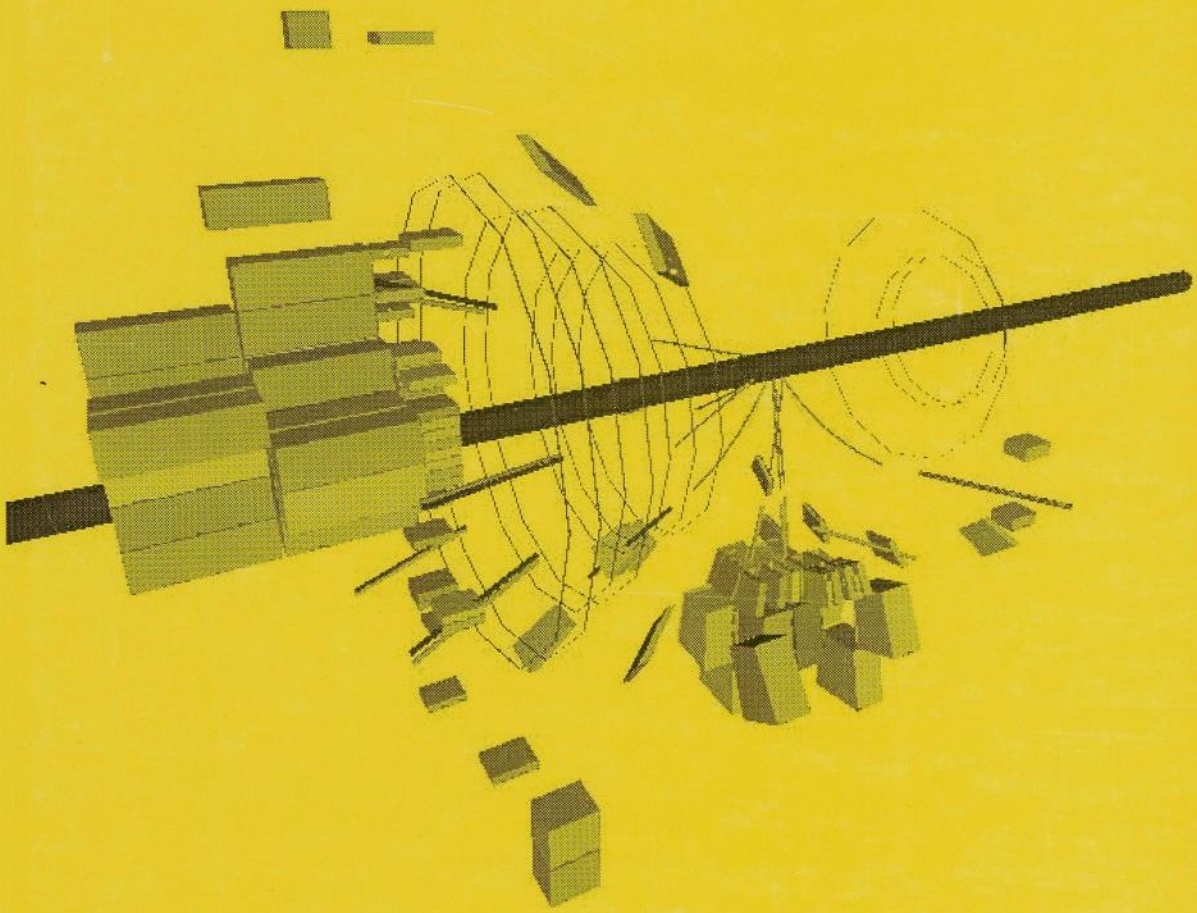

Andrés Kruse

Charged Current Interactions at HERA

Academisch Proefschrift

Ter verkrijging van de graad van doctor
aan de Universiteit van Amsterdam
op gezag van de Rector Magnificus Prof. Dr. J. J. M. Franse
ten overstaan van een door het College voor Promoties
ingestelde commissie, in het openbaar te verdedigen
in de Aula der Universiteit
op donderdag, 18 februari, 1999 te 11.00 uur

door

Andrés Kruse
geboren te Riberalta, Bolivia

Promotor: Prof. Dr. J. J. Engelen
Co-Promotor: Dr. P. M. Kooijman

Faculteit der Wiskunde, Informatica, Natuur- en Sterrenkunde

The work described in this thesis is part of the research programme of "het Nationaal Instituut voor Kernfysica en Hoge Energie Fysica (NIKHEF)" in Amsterdam, the Netherlands. The author was financially supported by "de Stichting voor Fundamenteel Onderzoek der Materie (FOM)", which is funded by "de Nederlandse Organisatie voor Wetenschappelijk Onderzoek (NWO)".

for Elaine

Contents

Chapter 1

Introduction

1.1 The World and what Physics knows of it

Ever since man could think he has been curious to know about the physical world and why it is the way it is. Indeed, what he really wanted to know were the origin of and reasons for his existence but that is religion and not subject of this thesis. The curiosity about the physical world usually had very practical reasons - to know about the reasons and time of the seasons was good for a farmer, to know how to determine the true gold content of a crown good for a king. The increased knowledge about the physical world slowly led to demystification of nature and this is one of the big achievements of science: A clap of thunder did in fact not mean that a weather god was in a bad mood but simply that there was a sudden discharge of electrostatic charge built up between earth and a cloud. Since the discovery of more complex properties of nature mankind began to believe however, that eventually physicists would know the answer to everything and physics has become a replacement for religion for many - it has many of the properties of a religion, it has its own language, mathematics, it has priests who talk with each other in that strange language and who make predictions about the world which turn out to be true. Many non-scientists suffer from the illusion that it should therefore naturally also answer the very religious questions about the why and wherefor of the human existence. From a scientist's point of view, however, it is clear that all we really do is to describe the little bit of nature that is accessible to us, nothing more: We build telescopes to study the stars and the cosmos, we make statistical analyses of the behavior of children in problem families, and we build devices to study the physical world at very small distances. This brings us closer to the subject of this thesis.

1.2 Structure of Matter

To investigate the underlying structure of matter it is necessary to have a probe of sufficient resolving power. To do this physicists have utilized the method of scattering particles from a target which one wishes to study. The resolving power is proportional to the absolute value of the four momentum transfer. In this way it was possible for Rutherford to establish the existence of a small nucleus inside a large atom. Subsequent experiments showed that the nucleus was a bound system of protons and neutrons, collectively called nucleons. In 1968 the first deep inelastic scattering experiment was performed which for the first time was able to probe the structure of the nucleon: It was shown to consist of point-like constituents which

were somewhat later identified as the quarks Gell-Mann and Zweig had proposed to explain the symmetries observed between hadrons. A dynamical theory of the interactions of quarks through a quantized gluon field, Quantum-Chromodynamics (QCD), could successfully explain the observed proton structure and its dependence on the relevant kinematical variables.

With the advent of data from the *HERA* accelerator the range of the kinematical variables probed by experiments has increased enormously. Quark and gluon densities have been measured down to momenta as small as 10^{-5} times the proton momentum and to distance scales as small as 10^{-3} times the proton diameter.

The proton is now accurately described as an incoherent sum of quarks and gluons, whose momentum density functions obey the QCD prescribed evolutions.

This thesis describes the first observations of charged current deep inelastic scattering using a charged lepton beam. This allows a complementary and independent investigation into the structure of the proton and, more generally speaking, into the interactions between leptons and quarks.

1.3 Thesis Overview

In this thesis we will first introduce deep inelastic positron proton scattering and in particular charged current scattering from a theoretical point of view. We will also show some of the results obtained by other experiments and show the potential of the *HERA* machine for this kind of physics. We will then describe the *HERA* machine and the *ZEUS* detector in detail with emphasis on the components that were used for the analysis of the data presented in this thesis. The data are positron-proton scattering events as measured in 1994. We will then introduce the Monte Carlo simulation used for the analysis. Charged current event analysis consists of two steps, first the events need to be selected and then they can be analyzed. Because of the low cross section of the CC interaction the selection of events is a difficult task and the selection procedure used in this analysis is described in detail in two chapters. The analysis of the results and comparison to the expectation is then performed in the next chapter. The thesis ends with a summary. The three appendices describe work related to the *ZEUS UCAL* data acquisition and second level trigger system as well as the *ZEUS* global second level trigger system that was performed by the author while at *DESY* in Hamburg from 1992 to 1994.

Chapter 2

The Charged Current Process

2.1 Introduction

In deep inelastic scattering (DIS) we probe the constituents of the proton with a virtual boson: γ, Z^0 or $W^{\pm}$. In the case of neutral boson exchange (γ, Z^0) we speak of Neutral Current (NC) scattering, the exchange of a charged vector boson W^+ or W^- is called Charged Current (CC) scattering. Figure 2.1 shows the Feynman diagram for this process. We denote with l (l') the incoming (outgoing) lepton with four momenta k (k'), $q \equiv (k - k')$, P the initial state proton with four momentum p and H the hadronic final state.

It is conventional to describe the kinematics of the scattering with Lorentz scalars. The four momentum transfer

$$Q^2 \equiv -(k - k')^2 = -q^2 \tag{2.1}$$

gives the length scale at which we probe

$$\lambda = 1/\sqrt{Q^2} \tag{2.2}$$

The maximum Q^2 is given by the center-of-mass energy squared of the lepton-proton system

$$s \equiv (p + k)^2 \tag{2.3}$$

Further the inelasticity,

$$y \equiv \frac{q \cdot p}{k \cdot p} \tag{2.4}$$

is, in the proton rest frame, the fraction of the energy transferred from the lepton to the struck quark.

Another convenient variable

$$x \equiv \frac{Q^2}{2q \cdot p} \tag{2.5}$$

gives the fraction of the proton four momentum carried by the struck quark.

Only two of the variables x, Q^2 and y are needed to fully describe the kinematics. For $s \gg {m_P}^2$ (m_P is the proton mass) the following relation between the above quantities holds

$$Q^2 = xys \tag{2.6}$$

The invariant mass of the hadronic final state is given by

$$W^2 = Q^2 \frac{1 - x}{x} + m_p^2 \tag{2.7}$$

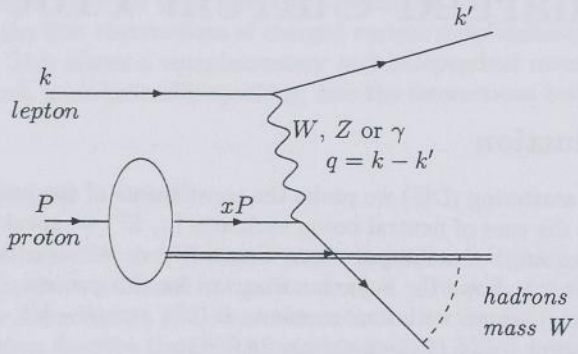

Figure 2.1: Feynman diagram for deep inelastic lepton proton scattering.

In terms of these variables the cross section for neutral current scattering is given by

$$\frac{d^2\sigma_{NC}}{dxdQ^2}(e^{\pm}p) = \frac{4\pi\alpha^2}{xQ^4}(y^2xF_1(x,Q^2) + (1-y)F_2(x,Q^2) \mp (y - \frac{y^2}{2})xF_3(x,Q^2)) \tag{2.8}$$

The structure functions xF_1, F_2 and xF_3 stem from general parameterization of the hadronic tensor [1].

For the naive quark parton model with massless quarks $2xF_1 = F_2$ and the structure functions F_2 and xF_3 can be written as

$$F_2(x,Q^2) = \sum_q A_q(Q^2)(xq(x) + x\bar{q}(x)) \tag{2.9}$$

$$xF_3(x,Q^2) = \sum_q B_q(Q^2)(xq(x) - x\bar{q}(x)) \tag{2.10}$$

with $q(x), \bar{q}(x)$ being the quark and anti-quark densities in the proton respectively and $A_q(Q^2)$, $B_q(Q^2)$ describing the coupling of quark of flavor q to the exchanged vector boson. $A_q(Q^2)$ can be written as

$$A_q(Q^2) = e_l^2 e_q^2 + 2|e_l||e_q|v_l v_q(\frac{1}{4\sin^2\theta_W \cos^2\theta_W})(\frac{Q^2}{Q^2 + M_Z^2})$$

$$+(v_l^2+a_l^2)(v_q^2+a_q^2)(\frac{1}{4\sin^2\theta_W\cos^2\theta_W})(\frac{Q^4}{(Q^2+M_Z^2)^2}) \quad (2.11)$$

with e_l, v_l, a_l and e_q, v_q, a_q the charge, vector and axial-vector coupling of the initial lepton and scattered quark respectively.

$B_q(Q^2)$ can be expressed as:

$$\begin{aligned} B_q(Q^2) &= 2|e_l||e_q|a_l a_q(\frac{1}{4\sin^2\theta_W\cos^2\theta_W})(\frac{Q^2}{Q^2+M_Z^2}) \\ &+4v_l a_l v_q a_q(\frac{1}{4\sin^2\theta_W\cos^2\theta_W})(\frac{Q^4}{(Q^2+M_Z^2)^2}) \end{aligned} \quad (2.12)$$

One can identify taking the first term of equation (2.8) and equations (2.11) and (2.12) the propagator terms for the exchange of a γ $(1/Q^4)$, the Z^0 $(1/(Q^2+M_Z^2)^2)$ and the interference of Z^0 and γ exchange $(1/(Q^2(Q^2+M_Z^2)))$.

For charged current scattering the cross section is:

$$\frac{d^2\sigma_{CC}}{dxdQ^2}(e^{\pm}p) = \frac{\pi\alpha^2}{8\sin^4\theta_W}\frac{1}{(Q^2+M_W^2)^2}((1+(1-y)^2)W_2^{\pm} \mp (1-(1-y)^2)W_3^{\pm}) \quad (2.13)$$

W_2 and W_3 are the sum and difference respectively of the quark and anti-quark densities. Since charge is conserved at the $W^{\pm}q$ vertex only those quarks which actually contribute to the cross section are taken:

$$\begin{aligned} W_2^+ &= x\sum_i (d_i(x)+\bar{u}_i(x)) \\ W_2^- &= x\sum_i (u_i(x)+\bar{d}_i(x)) \\ W_3^+ &= x\sum_i (d_i(x)-\bar{u}_i(x)) \\ W_3^- &= x\sum_i (u_i(x)-\bar{d}_i(x)) \end{aligned} \quad (2.14)$$

Again one can identify in equation (2.13) the propagator term for the $W^{\pm}$ exchange $(1/(Q^2+M_W^2)^2)$.

Clearly, when comparing the cross section for charged and neutral current scattering one can readily see that for relatively small Q^2 CC scattering is significantly less probable than NC scattering. The CC cross section is relatively flat for Q^2 up to the mass of the $W^{\pm}$ squared.

It is important to note that in the naive quark parton model the structure functions are independent of Q^2. When gluon radiation of the quarks and splitting of gluons into quark anti-quark pairs are taken into account (QCD improved quark parton model), the parton density functions become indeed dependent on Q^2. The dependence is described in leading order QCD by the *DGLAP* [2] equations:

$$\frac{dq_f(x,Q^2)}{dlogQ^2} = \frac{\alpha_s(Q^2)}{2\pi}\int_z^1 (q_f(z,Q^2)P_{qq}(\frac{x}{z}) + G(z,Q^2)P_{qg}(\frac{x}{z}))\frac{dz}{z} \quad (2.15)$$

$$\frac{dG(x,Q^2)}{dlogQ^2} = \frac{\alpha_s(Q^2)}{2\pi}\int_z^1 (G(z,Q^2)P_{gg}(\frac{x}{z}) + \sum_f (q_f(z,Q^2)+\bar{q}_f(z,Q^2))P_{gq}(\frac{x}{z}))\frac{dz}{z} \quad (2.16)$$

Here $G(x,Q^2)$ is the gluon density in the proton and the "splitting functions" $P_{ij}(y)$ give the probability of obtaining a parton i from parton j where parton i has a fraction y of the momentum of parton j.

With these equations it is possible to calculate the parton density functions at all Q^2 if they are given at a certain Q_0^2. In next to leading order the equations become more cumbersome and the densities become dependent on the renormalization scheme. Within each scheme, however, the parton densities should be universal functions applicable to any interaction. In particular it should be possible to use parton density functions extracted from NC scattering to calculate CC scattering and visa versa.

2.2 Parton Density Functions

NC data from *ZEUS* and *H1* have been used to extract the parton densities (q, $\bar{q}$ and G) of the proton. An example of data from *ZEUS* and *NMC* are shown in figures 2.2 and 2.3 together with the *PDF* fit which uses the *DGLAP* evolution [2] done by the *ZEUS* experiment. The figures have been taken from [3].

Many other groups have performed fits such as *GRV* [4], *CTEQ* [5] and *MRS* [6] which are available as *PDFLIB* [7]. These groups have used more data than just DIS but give an equally good description of *ZEUS* data.

The subject of this thesis is charged current positron proton scattering. As seen from equation (2.14) the charged current process selects a subset of quarks inside the proton. This allows investigation of the flavor decomposition of the parton densities.

Previous data on CC scattering stem from ν scattering ([8, 9, 10]). The energy of the ν beam is restricted to about 300 GeV which yields an s-value of about 600 GeV^2 compared to the 90200 GeV^2 available at *HERA*. An example of the structure functions for νp scattering is shown in figure 2.4. The data have been taken from [8]. The curve shows the CTEQ4D parameterization of the measured structure function. The agreement is not more than reasonable. This is most likely due to the transformation of the measured data to one fixed Q^2 for which the authors use a power law behavior with a fixed slope below $x = 0.2$ and a different slope above $x = 0.2$. However the overall features and magnitude are still reasonably described by the parameterization.

Fixed target experiments reach up to a Q^2 of about 25 GeV^2 for measurements on protons and of Q^2 of approximately 100 GeV^2 and $x > 0.1$ for measurements on Fe targets.

The current parton density functions which fit the NC data predict total cross sections for NC and CC scattering at *HERA* of

$$\sigma_{nc}^{tot}(Q^2 > 1\mathrm{GeV}^2) = 1.15\,\mu\mathrm{b}$$
$$\sigma_{cc}^{tot}(Q^2 > 1\mathrm{GeV}^2) = 38.7\,\mathrm{pb}$$

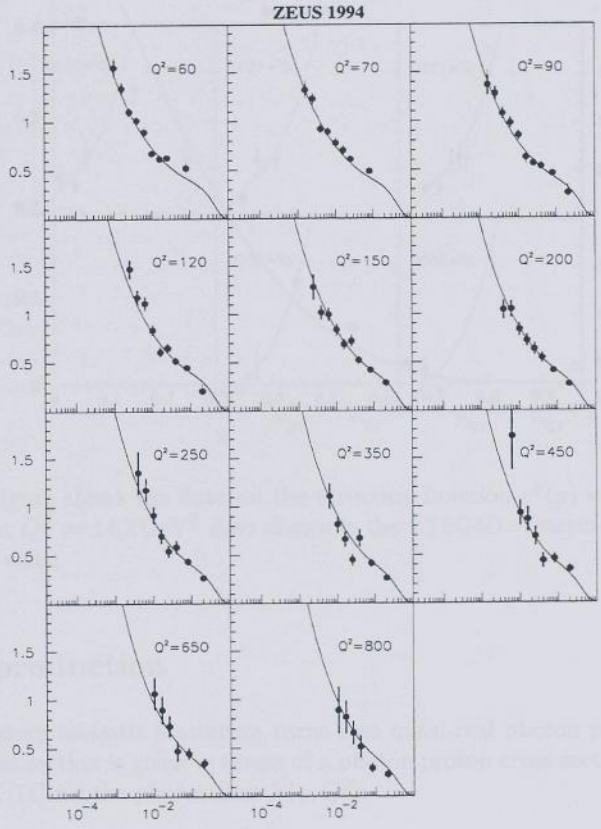

Figure 2.2: Structure function F_2 for various values of Q^2 ($60\,\mathrm{GeV}^2 < Q^2 < 800\,\mathrm{GeV}^2$) as a function of x as measured by the *ZEUS* collaboration. The curves indicate a QCD NLO fit to the data. The Q^2 values are indicated in GeV^2.

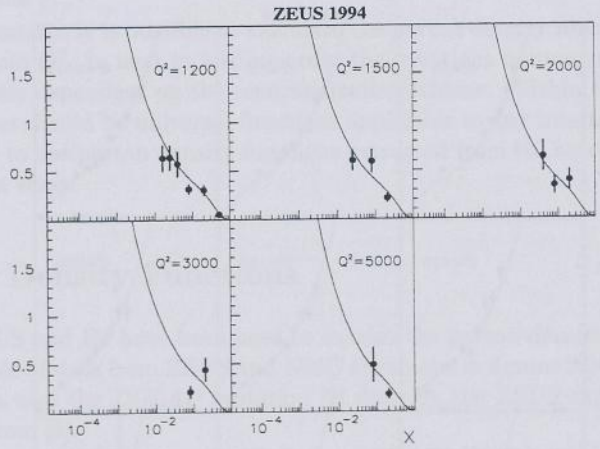

Figure 2.3: Structure function F_2 for various values of Q^2 ($1200\,\mathrm{GeV}^2 < Q^2 < 5000\,\mathrm{GeV}^2$) as a function of x as measured by the *ZEUS* collaboration. The curves indicate a QCD NLO fit to the data. The Q^2 values are indicated in GeV^2.

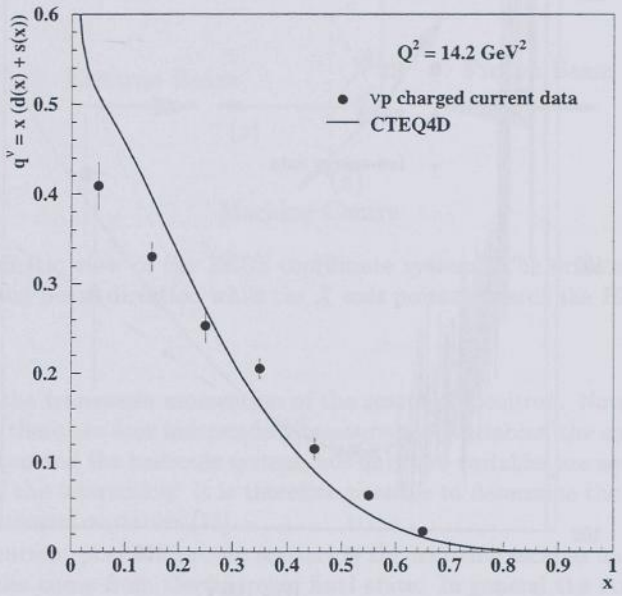

Figure 2.4: The figure shows the data on the structure function $q^\nu(x) = (x * (d(x) + s(x)))$ as measured by [8] at $Q^2 = 14.2\,\mathrm{GeV}^2$ Also shown is the CTEQ4D structure function parameterization at this Q^2 value.

2.3 Photoproduction

At very low Q^2, deep inelastic scattering turns into quasi-real photon proton scattering. The lepton proton cross section is given in terms of a photon proton cross section by the Weizsäcker-Williams formula [11] for the photon flux $F(y, Q^2)$:

$$\begin{aligned} \frac{d^2\sigma_{ep}(s)}{dydQ^2} &= \sigma_{tot}^{\gamma p}(ys) \cdot (1 + \delta_{RC}) \cdot F(y, Q^2) \\ &= \sigma_{tot}^{\gamma p}(ys) \cdot (1 + \delta_{RC}) \cdot \frac{\alpha}{2\pi Q^2}\left(\frac{1 + (1-y)^2}{y} - \frac{2(1-y)}{y} \cdot \frac{(m_e y)^2}{Q^2(1-y)}\right) \end{aligned} \quad (2.17)$$

The factor $(1 + \delta_{RC})$ takes into account QED radiative corrections to the e-p Born cross section. δ_{RC} is small ($< 5\%$) over most of the phase space. The photon proton cross section has been measured over a wide range of center-of-mass energy and is in the range of $100\,\mu$b to $200\,\mu$b as shown in figure 2.5. This translates into a positron proton cross section with $W > 10\,\mathrm{GeV}$ and for Q^2 from the kinematical limit to about $1\,\mathrm{GeV}^2$ of $40\,\mu$b.

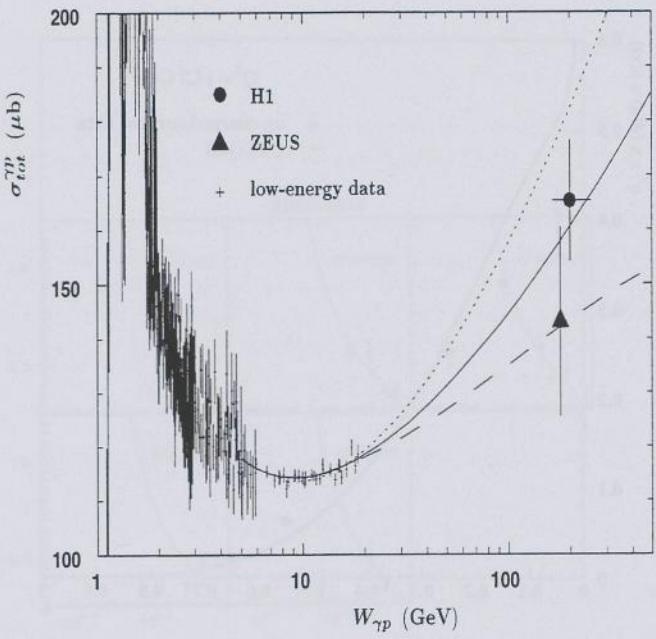

Figure 2.5: The figure shows the total photoproduction cross section $\sigma_{tot}^{\gamma p}$ in dependence of the center-of-mass energy of the γp system. Shown are the values measured by *ZEUS* and *H1*, and low energy measurements of many other experiments. The figure has been taken from [12].

2.4 Event Kinematics Reconstruction

The *ZEUS* coordinate system is shown in figure 2.6.

The reconstruction of the kinematic variables for neutral current scattering can easily be done if the outgoing positron scattering angle θ and energy E are measured. Equations (2.1), (2.4) and (2.5) then read

$$Q^2 = 2AE(1+\cos\theta) \tag{2.18}$$

$$y = 1 - \frac{E}{2A}(1-\cos\theta) \tag{2.19}$$

$$x = \frac{A}{P}\frac{E(1+\cos\theta)}{(2A - E(1-\cos\theta))} \tag{2.20}$$

with P the energy of the incoming proton and A the energy of the incoming positron. From equation equations (2.18) and (2.19) one can easily derive:

$$Q^2 = \frac{p_{Te}^2}{1-y} \tag{2.21}$$

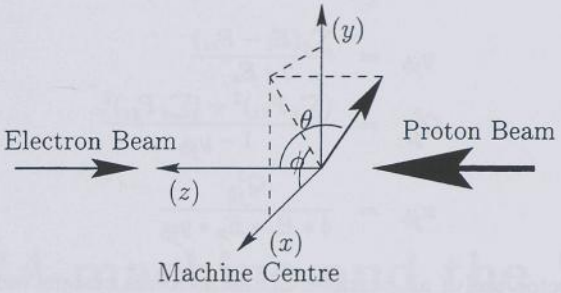

Figure 2.6: Schematic view of the *ZEUS* coordinate system. The orientation of the Z axis is given by the proton beam direction while the X axis points towards the *HERA* machine center.

where p_{Te} is the transverse momentum of the scattered positron. Note that the problem is over determined, there are four independent measurement variables, the energy and direction of the scattered lepton and the hadronic system, but only two variables are needed to fully describe the kinematics of the interaction. It is therefore possible to determine the kinematics from any two of the measurement variables [13].

For charged current positron proton scattering the neutrino escapes undetected, so the only detectable particles come from the hadronic final state. In general the struck quark is ejected from the proton and will together with the remnant of the proton hadronize into a final state which typically will consist of a jet proximately in the direction of the struck quark and a jet in the proton remnant direction.

In this case we can determine the kinematic variables from the energy and momenta of the final state particles. Denoting the sum of the four momenta of the final state particles by p' then the momentum transfer vector is given by $q = (p - p')$. The variable y then follows from

$$\begin{aligned} y &= \frac{p \cdot (p - p')}{p \cdot k} \\ &= \frac{P \sum_h (E_h - p_{Zh})}{2PA} \\ &= \frac{\sum_h (E_h - p_{Zh})}{2A} \end{aligned} \tag{2.22}$$

where the sum runs over all final state particles in the hadronic system. Because of conservation of transverse momentum we can use equation (2.21) to determine Q^2 by replacing p_{Te}^2 by p_{Th}^2:

$$p_{Th}^2 = \left(\sum_h p_{Xh}\right)^2 + \left(\sum_h p_{Yh}\right)^2 \tag{2.23}$$

where again the sum runs over all final state particles in the hadronic system. Finally the value of x can be obtained from equation (2.6). In this way we arrive at the Jacquet-Blondel variables [14] for the reconstruction of the kinematic variables:

$$y_{jb} = \frac{\sum_i (E_i - P_{zi})}{2 * E_e} \tag{2.24}$$

$$Q^2_{jb} = \frac{(\sum_i P_{xi})^2 + (\sum_i P_{yi})^2}{1 - y_{jb}} \tag{2.25}$$

$$x_{jb} = \frac{Q^2_{jb}}{4 * E_e * E_p * y_{jb}} \tag{2.26}$$

For an ideal detector and if all particles of the hadronic system were measured the above formulas would exactly return the event kinematics variables. In reality however the energy of the particles can only be determined with a finite precision. Moreover the particles lose energy while traversing material before hitting the calorimeter. For this reason the Jacquet-Blondel estimators tend to return a smaller value than the true one for Q^2 and x.

It is interesting to note that the Jacquet-Blondel estimators are not so sensitive to particles escaping through the beam pipe hole, as these particles usually carry small P_t and $(E_{tot} - P_z)$.

It is useful to introduce another variable which is the hadronic angle γ_{had}. In the quark parton model γ_{had} gives the polar angle of the struck quark:

$$\cos\gamma_{had} = \frac{{P_t}^2 - (E_{tot} - P_z)^2}{{P_t}^2 + (E_{tot} - P_z)^2} \tag{2.27}$$

Chapter 3

The *HERA* machine and the *ZEUS* detector

3.1 The *HERA* Particle Accelerator

The "Hadron-Elektron-Ring-Anlage" (*HERA*) was built from 1984 to 1992 at the "Deutsche Elektronen Synchrotron" (*DESY*) laboratory in Germany and is the world's largest Electron-Proton collider.

HERA consists of two storage rings, one for protons and one for electrons (or positrons). It is built below surface in a near-circular tunnel of 6.336 km circumference. It has four experimental underground halls, of which two are used by general purpose electron-proton collision experiments, *H1* [15] and *ZEUS* [16]. The other two are used by *HERMES* which uses the electron beam on a polarized gas target to study the origin of nucleon spin and *HERA-B* which studies CP violation in B-meson decays using the proton beam on an internal wire target. Both of these experiments use the beams parasitically.

In the proton ring super conducting magnets are used to store the protons which have an energy of 820 GeV. The electron ring has super conducting *R.F.* cavities to accelerate the electrons and during storage to compensate for the loss of energy due to synchrotron radiation. The electron beams have an energy of 27.52 GeV.

At the *H1* and *ZEUS* experimental halls a combination of dipole and quadrupole magnets is used to bring the two beams into head-on collision and to provide the final focus for the beams.

Figure 3.1 shows a schematic view of *HERA* and its pre-accelerators, table 3.1 lists the main design parameters for *HERA*.

3.1.1 Bunch Structure

Both the positron and proton beams are stored in a total of 220 *R.F.* buckets. This yields a bunch structure of the beam with a time between two successive e-p bunch collisions of 96 ns.

Not all of the 220 bunches are filled. This allows background studies to be performed. Events that occur when only a positron or only a proton bunch pass the detector can be used to evaluate the background from beam gas interactions. Whereas times when neither proton nor positron pass the detector allow investigation of the noise characteristics of the detector and of the backgrounds due to cosmic rays.

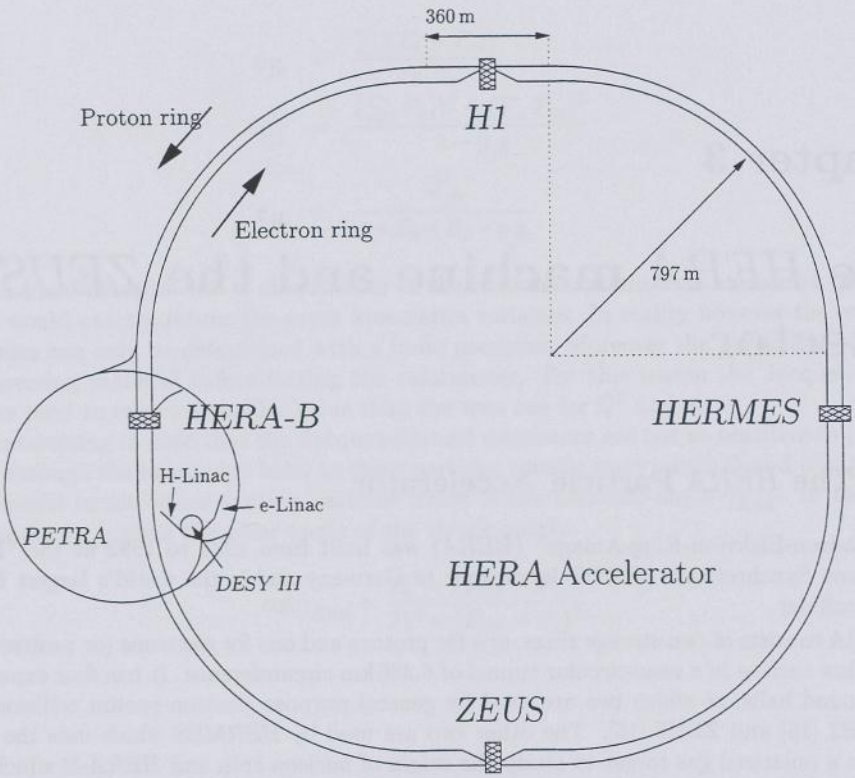

Figure 3.1: Schematic view of the *HERA* collider and its pre-accelerators, the linear accelerators for electrons (or positrons) and protons, the *DESY III* accelerator ring and *PETRA*. The locations of the experiments are also indicated.

3.2 The *ZEUS* Detector

The *ZEUS* detector is a multi purpose *e-p* collision detector. Like other high energy collider experiments the *ZEUS* detector consists of layers of sub-detectors which surround the interaction point. Since the positron and proton beam momentum are so different the detector is asymmetric with respect to the beam direction. Figure 3.2 shows cross sectional views of the *ZEUS* detector. The innermost detector is the vertex detector (*VXD*), followed by the central tracking detector (*CTD*). In the forward direction the tracking is complemented by a forward drift chamber (*FTD*) and transition radiation detector (*TRD*) and in the rear direction a planar drift chamber (*RTD*) is installed. The tracking detectors are surrounded by a super conducting solenoid (*COIL*) which produces a magnetic field of 1.432 Tesla. The next layer consists of the Uranium scintillator calorimeter (*UCAL*). The flux return yoke (*YOKE*) for the solenoidal field is instrumented as backing calorimeter (*BAC*) capable of detecting leakage of particles from the *UCAL*. The inside and outside of the return yoke are instrumented with muon chambers (*FMUON*, *BMUON* and *RMUON*), the forward muon chamber (*FMUON*) is complemented by a toroidal magnet. In the

HERA beams	Electron	Proton
Center of mass energy	314 GeV	
Nominal energy	30 GeV	820 GeV
Relative energy spread $\Delta E/E$	10^{-3}	10^{-4}
Injection energy	12 GeV	40 GeV
Luminosity per interaction point	1.6×10^{31} cm^{-2}s^{-1}	
Average current	58 mA	163 mA
Particles per bunch	3.65×10^{10}	10^{11}
Number of bunches	220	220
Maximum number of filled bunches	210	210
Beam crossing angle	head-on collision, 0 mrad	
Bunch crossing interval	96 ns $\simeq 28.8\,m$	
Bunch length at maximum energy (σ_z)	0.85 cm	19 cm
Beam width at the interaction points (σ_x)	0.286 mm	0.28 mm
Beam height at the interaction points (σ_y)	0.06 mm	0.058 mm
Synchrotron radiation loss per turn	125 MeV	6×10^{-10} MeV
Polarization time at 30 GeV	35 min	-
Filling time	15 min	20 min

Table 3.1: Main design parameters of the *HERA* machine.

rear of the *ZEUS* detector the *Vetowall* detector is installed. Close to the beam collimator *C5*, *ZEUS* has a detector (*C5*) which is used to monitor the beam quality and timing. Further away from the interaction point and not shown in figure 3.2 is the luminosity monitor (*LUMI*).

A detailed and complete description of the *ZEUS* detector can be found in [17]. We will concentrate further only on the sub-detectors that were used for the charged current event selection and analysis: *CTD*, *UCAL*, *BMUON*, *RMUON*, *FMUON*, *Vetowall*, *C5* and the luminosity monitor *LUMI*.

3.2.1 Central Tracking Detector (*CTD*)

The Central Tracking Detector (*CTD*) is a cylindrical drift chamber with nine super layers of eight sense wire layers each. Five of the super layers (odd numbered) have wires parallel to the chamber axis, four layers (even numbered) have stereo layers with wires tilted under a small angle (5° or 7°) with respect to the beam. The single wire hit resolution of the *CTD* is 170 μ m. The chamber covers an angular range of $15° < \theta < 164°$. The *CTD* is read out by two independent readout systems, the "Z-by-timing" and the *FADC* system. The "Z-by-timing" system is used for the layers with the parallel wires and uses the difference between the arrival times of the pulses at the two ends of a wire to determine the Z coordinate. Its Z resolution is about 4 cm. Using the *FADC* system, the combination of the axial and stereo wire information allows the reconstruction of the Z vertex of a track with a precision of 1 mm.

3.2.2 Uranium Scintillator Calorimeter (*UCAL*)

The *ZEUS* high resolution calorimeter is constructed of layers of depleted Uranium and Scintillator. It consists of three sections, forward (*FCAL*), barrel (*BCAL*) and rear (*RCAL*). The

forward (*FCAL*) and rear (*RCAL*) calorimeter consist of two halves which can be retracted in order to avoid radiation damage due to beam losses during beam injection.

The *FCAL* and *RCAL* are subdivided in modules of 20 cm width and varying height arranged as shown in figures 3.3 and 3.4. The tallest module has an active height of 4.6 m. Each module consists of towers with a frontal area of $20 \times 20\,\mathrm{cm}^2$. Each tower is segmented in depth in an electromagnetic section (*EMC*) of $25\,X_0$ and one (*RCAL*) or two (*FCAL*) hadronic (*HAC*) sections. The total depth of the *FCAL* is $7\,\lambda$ and that of the *RCAL* is $5\,\lambda$. The *EMC* sections of the *FCAL* and *RCAL* are further divided vertically in cells of $5 \times 20\,\mathrm{cm}^2$ and $10 \times 20\,\mathrm{cm}^2$ frontal area respectively. A layer of $3 \times 3\,\mathrm{cm}^2$ silicon diodes (*HES*) is placed inside the *EMC* sections at a depth of $3\,X_0$ to aid in the separation of hadronic and electromagnetic showers.

The *BCAL* consists of 32 "pie shaped" modules arranged concentrically around the beam at a distance of 1.32 m (see figure 3.2). Each module has a length of 3.2 m and subtends 11.25° in azimuth. The modules are tilted by 2.5° to avoid projective cracks between modules. Each module is subdivided in 14 non projective *HAC* towers, each of which are segmented in two sections in depth. The *HAC* towers are preceded by an *EMC* section divided in 53 cells which have a projective geometry. The perpendicular depth of the *EMC* is $23\,X_0$ and the total perpendicular depth of the *BCAL* is $5\,\lambda$.

The entire *UCAL* thus consists of 5918 cells. The scintillation light of each cell is guided to the back of the calorimeter via two wavelength shifter (*WLS*) guides, one on either side of each cell. Each *WLS* is read out by a photomultiplier (*PMT*). To reduce the effects of the cracks between modules, in particular the generation of Cherenkov light in the *WLS*, sheets of 4 mm of lead are placed between all the modules.

The energy resolution of the *UCAL* is $\sigma(E)/E = 0.18/\sqrt{E}$ for electromagnetic showers and $\sigma(E)/E = 0.35/\sqrt{E}$ for hadronic showers where the shower energy E is in GeV.

The timing resolution of each individual channel is given by

$$\sigma(T) = 0.4 + 1.4/(E_{ch}^{0.65})(ns) \tag{3.1}$$

where $E_{ch}[GeV]$ is the energy recorded in the channel (see [18]).

The radioactivity of the depleted Uranium causes a constant current drawn by the *PMT*s. The current is proportional to the cell size and used to calibrate the absolute energy scale of the calorimeter [19].

The *UCAL* readout system consists of two systems, one for the *FLT* and one for the *SLT* and higher level triggers. The signal for the *FLT* is split off on the detector and analogue sums of several cells are made. The *SLT* readout system has the higher precision of the full digitized readout.

3.2.3 Forward Muon Chamber

The forward muon chamber (*FMUON*) consists of a toroidal magnetized iron region, interleaved with sections of drift chambers, limited streamer tubes and time of flight counters. The outer diameter of the toroids is 6 m, the magnetic field 1.7 Tesla. The forward muon chambers provide a momentum measurement of muons of energies up to 100 GeV down to low angles.

Barrel and Rear Muon Chamber

In the barrel (*BMUON*) and rear (*RMUON*) muon systems the magnetic field of the iron *YOKE* is used to perform a momentum measurement. Each chamber consists of two layers of limited

streamer tubes with wires and perpendicular readout strips mounted on the inside and outside of the iron *YOKE*. For the barrel detector, the wires are in the beam direction, for the rear detector in the Y direction. The hit position resolution is better than 1 mm. The barrel and rear muon detector can be used to measure the momentum of prompt muons but also cosmic muons.

3.2.4 *Vetowall* and *C5* Detector

The *Vetowall* detector is an iron wall of 0.9 m thickness, placed in the upstream proton beam direction closing the accelerator tunnel. It has scintillator counters on both sides of the wall. The *C5* detector consists of 0.5 cm of lead, sandwiched between scintillators, placed around the *C5* beam collimator, at $z = -3.15\,\mathrm{m}$.

3.2.5 Luminosity Detector

In order to do a cross section measurement at a collider experiment the luminosity has to be determined. In order to do so the rate of a process with a well known cross section is measured. This process also has to have a high cross section to be used online so that the beam optics can be modified for maximum luminosity. At *HERA* the hard photon bremsstrahlung produced in the Bethe-Heitler process $ep \to ep\gamma$ [20] is used.

The *ZEUS* luminosity monitor (*LUMI*) consists of two calorimeters, one, for detecting the scattered photon is placed near the proton beam pipe at $Z = -107\,\mathrm{m}$, the other one, for detecting the scattered positron is placed at $Z = -34.7\,\mathrm{m}$. The acceptance for photon detection is 99 % for $E_\gamma > 5\,\mathrm{GeV}$. The positron acceptance is more difficult to estimate because the positrons have to traverse several magnets before reaching the calorimeter, but it is about 70 % for $10\,\mathrm{GeV} < E_e < 17\,\mathrm{GeV}$. The coincidence rate of the two calorimeters is used as a cross check for the luminosity determined from the photon counter only.

The luminosity detector of *ZEUS* and its operation are described in detail in [21, 22].

The data used for this thesis is the positron-proton data of 1994, for which *HERA* delivered a luminosity of $5.11\,\mathrm{pb}^{-1}$. Of this luminosity, *ZEUS* could trigger $3.3\,\mathrm{pb}^{-1}$, the difference being mainly due to the time necessary for the beam conditions to stabilize at the beginning of each run. Some losses were due to miscellaneous detector problems.

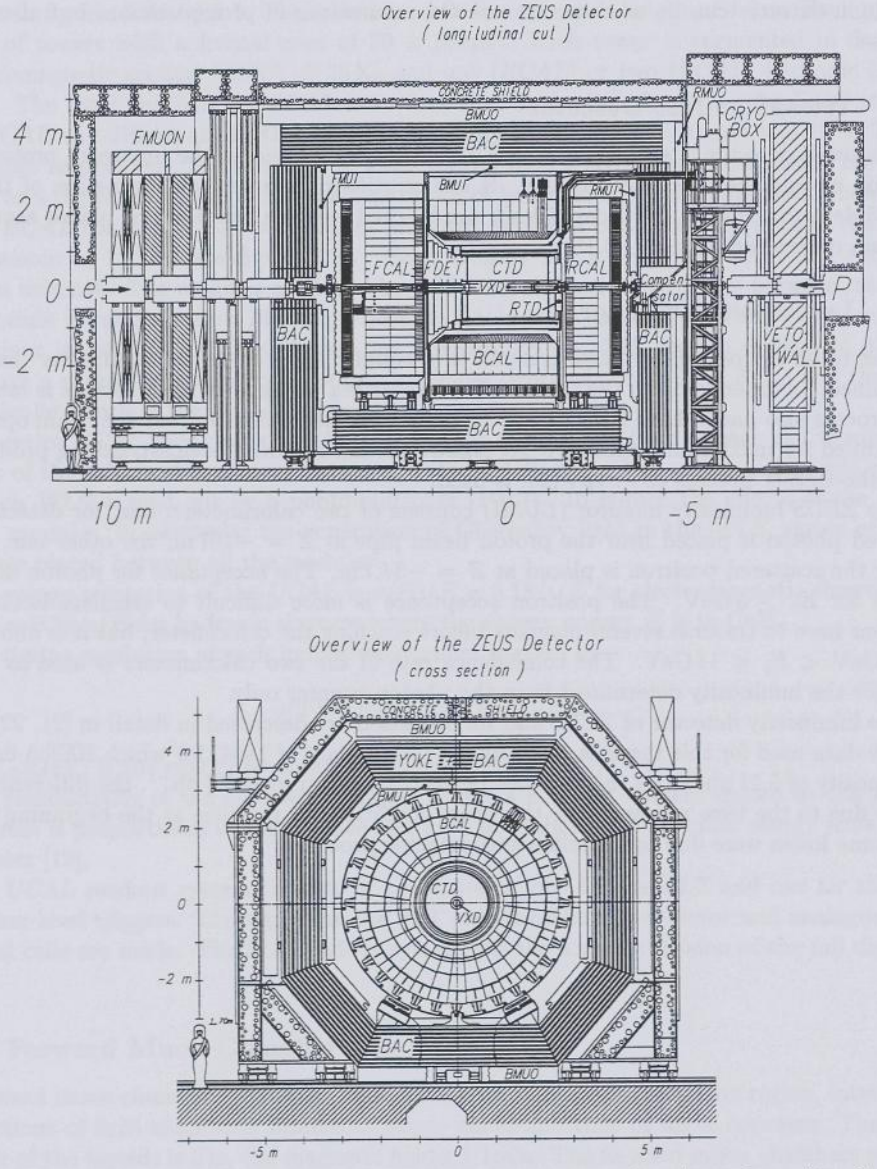

Figure 3.2: Cross section of the *ZEUS* detector along the beam line (top picture) and perpendicular to it (bottom picture).

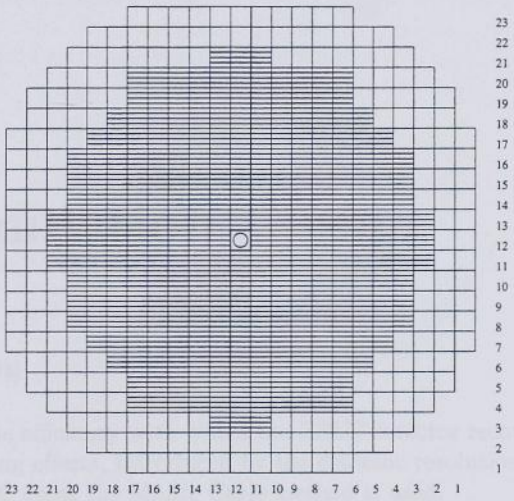

Figure 3.3: Schematic view of the front face of the *FCAL*.

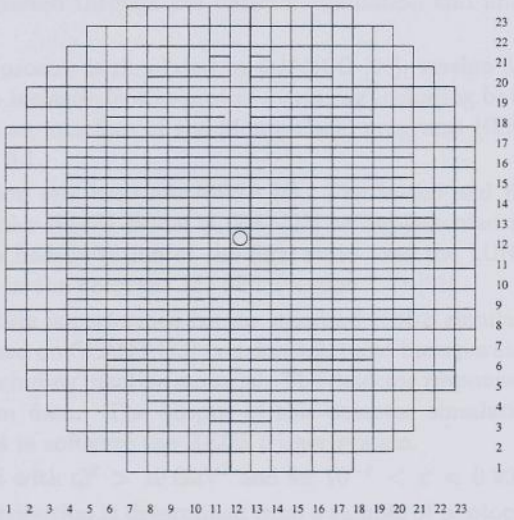

Figure 3.4: Schematic view of the front face of the *RCAL*.

Chapter 4

Event Simulation

4.1 Introduction

In order to determine the efficiency with which the *ZEUS* detector reconstructs CC events, and to determine the smearing effects, introduced by the detector resolution, on the reconstruction of the kinematics of a CC event the Monte Carlo method is used.

4.2 Monte Carlo Simulation

Events are generated by a generator program that simulates the hard scattering process. The output of the generator is passed through a program simulating the hadronization. The generated particles are then passed through the detector simulation and finally through the trigger simulation program.

The hard scattering process is simulated by DJANGO [25], version 6.2. The event generator DJANGO simulates deep inelastic lepton-proton scattering including both QED and QCD radiative effects. DJANGO is an interface of the Monte Carlo programs HERACLES [26] version 4.4 and LEPTO [27] version 6.1.

The structure function sets used are MRSA [6]. The initial and final state QCD cascade is simulated using the color dipole model (CDM) [28] as implemented in the program Ariadne (version 4.06) [29]. The hadronization of the final state uses the LUND string fragmentation model [30] implemented in the program JETSET (version 7.4) [31].

The detector simulation is performed by the standard *ZEUS* simulation program MOZART [32]. This program is based on GEANT [33] (version 3.21) and incorporates a detailed description of the *ZEUS* detector, including inactive material. The detector responses have, where necessary, been tuned to test-beam data. The output of this detector simulation program is fed into ZGANA, which simulates in software the *ZEUS* trigger system.

Events are generated with $Q^2 > 10\,\mathrm{GeV}^2$ and for $10^{-4} < x < 0.999$.

The event vertex distribution is determined from a sample of photoproduction data taken in the period for which we analyze the charged current data. For these events the vertex finding efficiency is high ($\sim 80\,\%$) and no bias on the distribution of the z position of the vertex is introduced.

We generate 2853 events which corresponds to a total luminosity of $75\,\mathrm{pb}^{-1}$.

4.3 Measurement of Event Kinematics

The measurement of the event kinematics is performed with the Jacquet-Blondel variables (see (2.24)), but instead of summing over particles, the sums are calculated from the energy deposits in the calorimeter and the angle of the center of the calorimeter cells with respect to the measured vertex, i.e.:

$$E_{tot} - P_z = \sum_{cell} E_{cell}(1 - \cos\theta_{cell}) \tag{4.1}$$

$$y_{jb} = \frac{E_{tot} - P_z}{2A} \tag{4.2}$$

$$P_x = \sum_{cell} E_{cell} \sin\theta_{cell} \cos\phi_{cell} \tag{4.3}$$

$$P_y = \sum_{cell} E_{cell} \sin\theta_{cell} \sin\phi_{cell} \tag{4.4}$$

$$P_t^2 = ({P_x}^2 + {P_y}^2) \tag{4.5}$$

Note that for CC interactions the energy in all cells stems by definition from the hadronic final state.

4.4 Detector Resolution

The Monte Carlo data can be used to show the detector resolution for the CC events. Figure 4.1(a) and (b) show the detector response for $(E_{tot} - P_z)$ and P_t respectively. The reconstructed value is shown on the vertical, the true value on the horizontal axis. Clearly the reconstructed value is systematically lower than the true value. This stems from the fact that the particles have to pass through inactive material before reaching the *UCAL* and thus lose energy. Figure 4.2(a) shows the P_t resolution as function of P_t. The resolution is about 30 % for small P_t ($P_t < 10\,\mathrm{GeV}$) and less than 20 % for larger P_t values. Figure 4.2(b) shows the quality of the vertex reconstruction - only events for which a vertex is reconstructed are shown. The vertex resolution is about 20 cm.

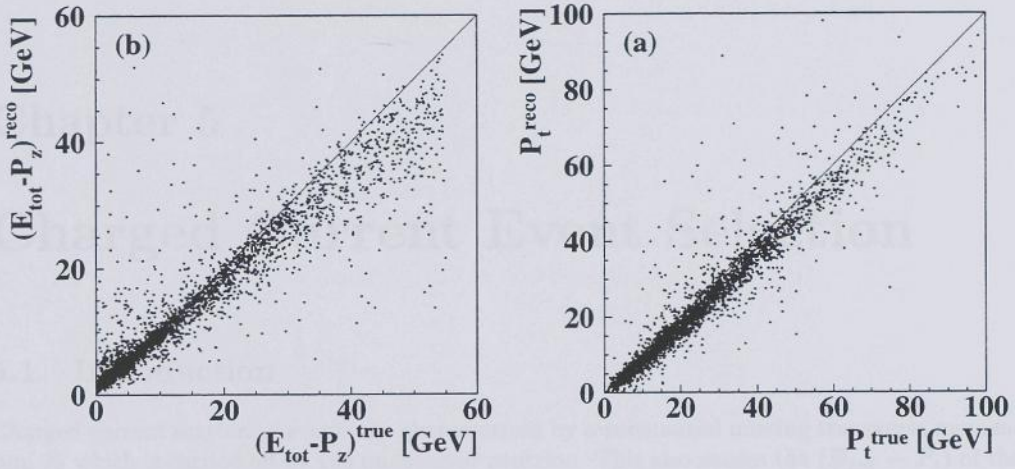

Figure 4.1: The detector response for $(E_{tot} - P_z)$ (a) and P_t reconstruction (b). The reconstructed value is shown on the vertical, the true on the horizontal axis.

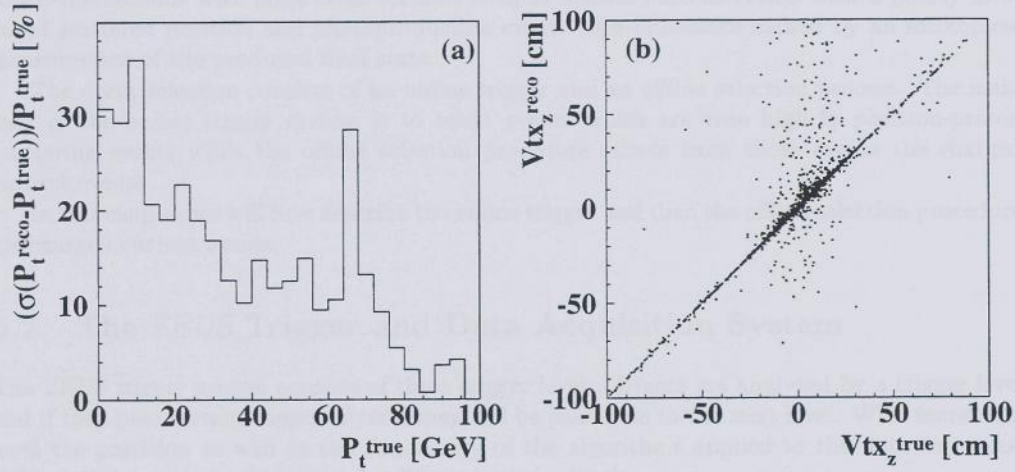

Figure 4.2: The detector resolution for P_t reconstruction (a) and response for vertex reconstruction (b). The reconstructed value is shown on the vertical, the true on the horizontal axis.

Chapter 5

Charged Current Event Selection

5.1 Introduction

Charged current scattering events are characterized by a substantial missing transverse momentum $P\!\!\!/_t$ which is carried off by the undetected neutrino. This also causes the $(E_{tot} - P_z)$ of the event to be lower than the $2E_e$ which should be measured for fully contained events. Furthermore the events should have characteristics consistent with the event having originated from the nominal interaction point.

The selection criteria are thus designed to extract events with the above characteristics. Some additional cuts are necessary to remove events which are caused by detector malfunctions. Moreover, cosmic ray muons, either alone or overlaying a bona fide e-p-interaction need to be rejected. Finally cuts are needed to remove events which are due to resolution effects in e-p-interactions with large cross sections such as neutral current events with a poorly measured scattered positron and photoproduction events with imbalance caused by an incomplete measurement of the produced final state.

The event selection consists of an online trigger and an offline selection process. The main task of the online trigger system is to select events which are true high-$P\!\!\!/_t$ positron-proton scattering events while the offline selection procedure selects from those events the charged current events.

In this chapter we will first describe the online trigger and then the offline selection procedure for charged current events.

5.2 The *ZEUS* Trigger and Data Acquisition System

The *ZEUS* trigger system consists of three trigger levels. Events are analyzed by a trigger level and if they pass certain trigger criteria they will be passed on to the next level. With increasing level the precision as well as the complexity of the algorithms applied to the data increases. Table 5.1 gives an overview over the different trigger levels.

5.2.1 First Level Trigger

The first level trigger (*FLT*) is a fully pipelined system implemented in hardware which analyses the data produced by the *ZEUS* detector at the *HERA* bunch crossing frequency of 10 MHz. The trigger logic and cuts are configured such that the rate of positive decisions is kept below

Level	Input Rate	Output Rate	Quantities and Algorithms
FLT	$10\,MHz$	< 1 kHz	coarse gain resolution and segmentation, massively parallel, dedicated hardware
SLT	$< 1\,kHz$	< 100 Hz	full resolution and segmentation, massively parallel, software programmable algorithms
TLT	$< 100\,Hz$	< 5 Hz	full resolution and segmentation, complex algorithms

Table 5.1: Comparison of *ZEUS* trigger levels.

$1\,kHz$, the maximum input rate of the *SLT*. The *FLT* has the uncalibrated detector data only available in coarse gain resolution, and its algorithms can only calculate global event properties.

5.2.2 Second Level Trigger

The second level trigger system (*SLT*) has the full detector resolution and segmentation available but is a massively parallel system of transputers which operate each on a small region of the detector data and combine their results in a tree-like structure. Algorithms are implemented in software but only have limited access to the data of neighboring regions. This puts considerable constraints on the possible trigger algorithms. Moreover, it has to operate at 1 kHz, so only relatively simple calculations are possible. The *SLT* uses partly calibrated detector information and a simple tracking algorithm is available.

5.2.3 Third Level Trigger

The third level trigger system (*TLT*) uses the full detector resolution and segmentation. It consists of a farm of workstations which receive full events. The algorithms have access to all data and so the only limit on the complexity of the algorithms is given by the fact that the *TLT* has to operate at 100 Hz. The *TLT* uses partly calibrated data and full tracking information is available.

5.2.4 Reconstruction

The first three trigger levels reject events, while at a fourth "reconstruction" step the data are reconstructed with the latest calibration information. This reconstruction is performed on archived event data. The data are then made available for further analysis.

5.3 Trigger Selection of Charged Current Events

$\not{P}_t$ is calculated on all trigger levels and in the offline event selection programs. At the first level trigger the calculation is based on calorimeter trigger towers which each contain several calorimeter cells. The result is therefore less accurate than the calculation of $\not{P}_t$ at higher trigger levels where the full readout information is available. Moreover the calculation is based on uncalibrated detector information. The cut imposed is $\not{P}_t > 9$ GeV. Figure 5.1 shows the

distribution of P_t for the Monte Carlo data sample with and without the *FLT*-cut as well as the ratio of both distributions, the turn on curve for the *FLT*: The *FLT* trigger turn on is quite slow, only at about 18 GeV is it fully efficient for charged current events.

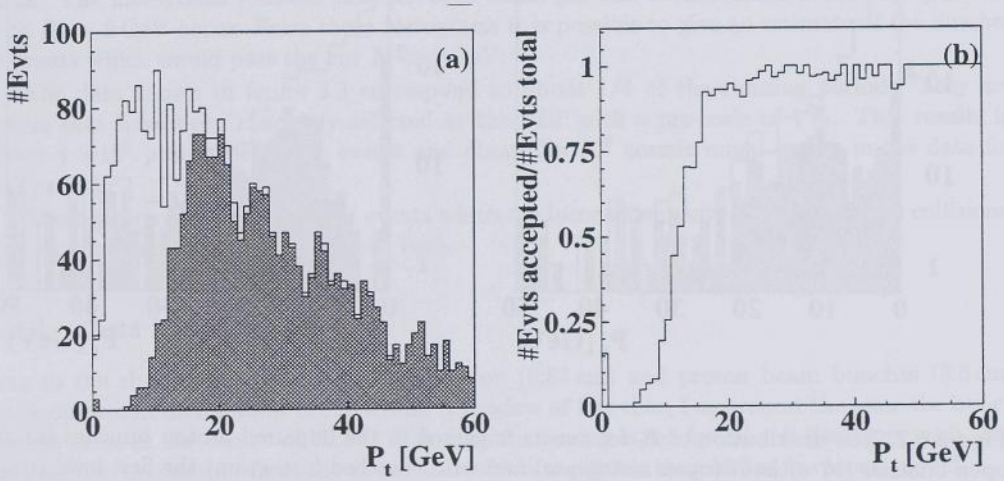

Figure 5.1: Figure (a) shows the distribution of P_t for the Monte Carlo data sample with $Q^2 > 10\,\mathrm{GeV}^2$ without any additional cuts (open histogram) and after the first level trigger cut which is based on P_t(shaded histogram) . The *FLT* uses calorimeter trigger towers which contain several calorimeter cells. Figure (b) shows the ratio of the distributions in figure (a), the turn on curve for this trigger.

The second and third level trigger calculation of P_t is more accurate because here the full readout information and granularity of the *UCAL* are available.

The *DST* selection programs have the calibrated detector information available. Furthermore P_t is calculated using the reconstructed vertex which yields the most accurate results possible.

Figure 5.2 shows the distribution of P_t for random events triggered in the unpaired and open bunches before and after the first level trigger P_t cut. There are many events at P_t close to zero, which are due to empty triggers by the *FLT*. These events are rejected at the *SLT*.

5.4 Trigger Rejection of Non Positron-Proton Collision Events

Common to all *ZEUS* physics data analyses is the need for the rejection of events which stem from non positron-proton collisions. At a nominal *HERA* luminosity of $1.6 \times 10^{31}\,\mathrm{cm}^{-2}s^{-1}$ the event rate due to deep inelastic positron-proton scattering is only about 10 Hz while the rate of background events is in the order of 100 kHz.

If the trigger $P_t > 9\,\mathrm{GeV}$ as described in section 5.3 were the only trigger used to identify charged current events a large number of background events present at *HERA* would be picked up.

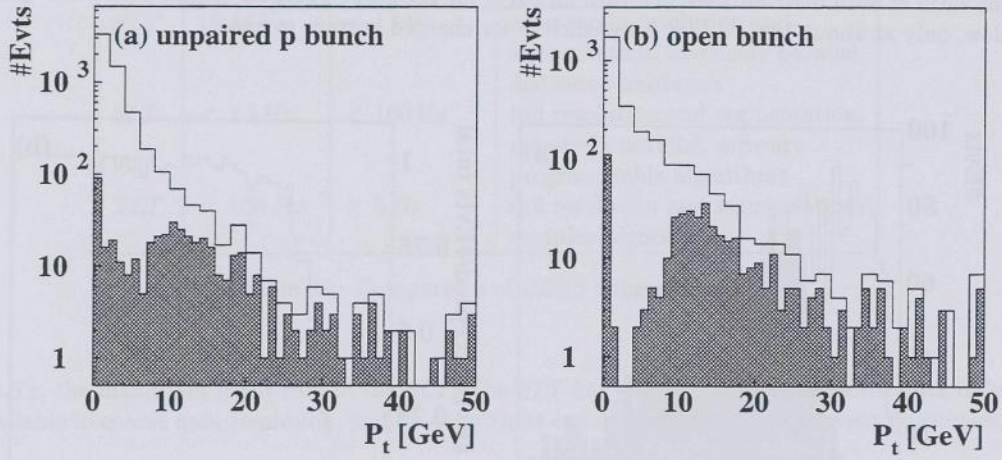

Figure 5.2: The distribution of P_t for events triggered in the unpaired proton bunches (a) and open bunches (b) without (open histogram) and with (hatched histogram) the first level trigger P_t-cut. The events at low P_t stem from events for which the *FLT* has fired but no energy was recorded (empty triggers)

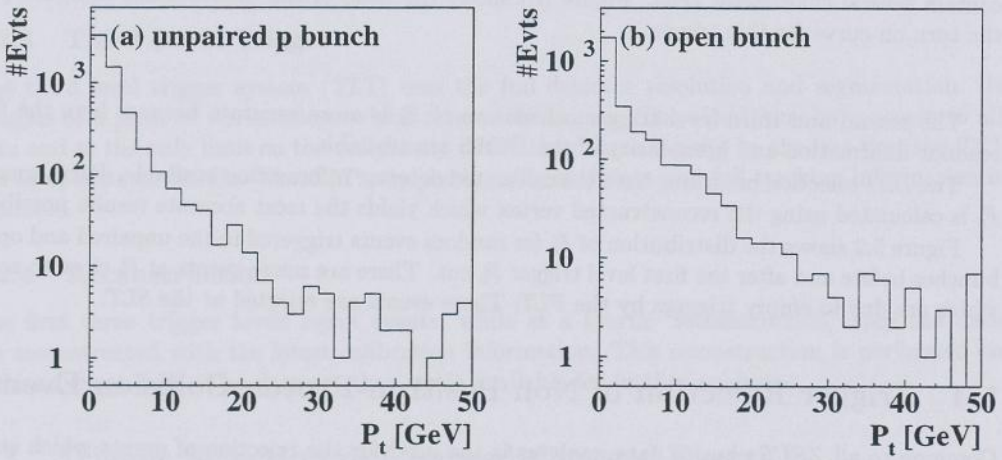

Figure 5.3: The distribution of P_t for events triggered in the unpaired proton bunches (a) and open bunches (b) which pass the first level trigger, excluding the P_t-cut. The histograms indicate that for both beam-gas as well as cosmic muon events many events with $P_t > 9\,\text{GeV}$ occur.

To illustrate the problem the P_t distribution of a random selection of events which have passed the first level trigger excluding the P_t cut for unpaired proton and open bunches is shown in figure 5.3. Triggers in the open bunch are mostly due to cosmic muons traversing the detector, while the triggers in the unpaired proton bunch stem from proton beam-gas interactions. The histograms indicate that for both beam-gas and cosmic muon events many events with $P_t > 9\,\text{GeV}$ occur. From those histograms it is possible to give an estimate of the number of events which would pass the cut $P_t > 9\,\text{GeV}$:

The data shown in figure 5.3 correspond to about 1/4 of the running period. They are events that have been randomly selected at the *SLT* with a pre-scale of 1 %. This results in about 4×10^6 proton beam gas events and about 3×10^6 cosmic muon events in the data for this period.

The trigger system rejects most events which are inconsistent with positron-proton collisions. The various cuts are briefly described here.

5.4.1 Cuts based on Timing

Due to the short bunch length of the positron (0.83 cm) and proton beam bunches (8.5 cm) positron-proton interactions occur within a window of less than 1 ns around the time the bunch centers cross in the center of *ZEUS*. The detector timing is set for all sub-detectors such that for particles originating from the nominal interaction point a time of 0 ns is reconstructed.

Any event which occurs outside of *ZEUS* can therefore be recognized if a sub-detector reports an event time outside a window around 0 ns. This is illustrated in figure 5.4 for a beam-gas collision event.

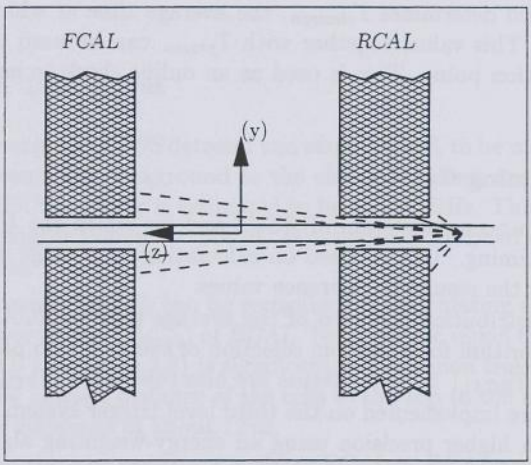

Figure 5.4: Schematic 2D view of a beam gas event. Shown here is the beam pipe (horizontal parallel lines) and a part of the *FCAL* and *RCAL* (hatched structures). The nominal vertex is at $(0, 0)$. The particles originating from the beam-gas event that occurred behind the *RCAL* also hit *FCAL*. Since *FCAL* and *RCAL* are about 5 m apart the average time of *FCAL* and *RCAL* for such an event differs by about 15 ns.

A rejection cut on the event time is orthogonal to the cuts used to accept events for a physics analysis and does not introduce any bias. The online trigger system uses the information from the *Vetowall*, the *C5* and *UCAL* to reject events based on timing.

Vetowall FLT Timing Cut

For the *Vetowall* detector (see section 3.2.4) a coincidence of two opposing plates within a short time window (±8 ns) is considered as a hit. When a hit occurs within a time window of ±8 ns centered at 25 ns before the bunch crossing time of the event the event is vetoed.

C5 FLT Timing Cut

For the *C5* detector (see section 3.2.4) a hit requires coincidence of the two opposing scintillator plates within a short time window (±1 ns). An event is vetoed if the hit occurs within a time window of ±3 ns centered around 8 ns before the bunch crossing time. Any activity from an event occurring at the nominal interaction point would have a time later by 8 ns and the *C5* timing resolution is 1 ns.

The *C5* detector is also used to make fine adjustments of the *ZEUS* data acquisition system internal clock to the *HERA* clock. Since all sub-detectors have a known and fixed time offset to each other the only quantity to be determined is the exact time with respect to the *ZEUS* time at which the interactions occur inside *ZEUS*. This is done by measuring the average time at which the proton bunches pass the *C5* detector, T_{proton}. This time is then corrected for the time of flight distance from the *C5* detector to the nominal interaction point, resulting in a time offset. This offset is small, typically less than 1 ns. It is measured before data taking starts and used as a constant time offset by the *ZEUS* higher level triggers.

The *C5* detector also determines $T_{electron}$, the average time at which the positron bunches pass the *C5* detector. This value, together with T_{proton} can be used to calculate the average location of the interaction point. This is used as an online check to ensure stable data taking conditions.

UCAL Beam-Gas Timing Cuts

Beam gas events which occur upstream of *ZEUS* and for which the *UCAL* is hit are rejected using the calorimeter timing. This is based on calculating an average event time in the *UCAL* regions and comparing the results to reference values.

In figure 5.5 the distribution is shown of the average time in *RCAL*, T_{RCAL}, as calculated by the *UCAL SLT* algorithm for a random selection of events which pass the first level trigger. Events are rejected if $|T_{RCAL}| > 8\,ns$. Events are also rejected if $(T_{FCAL} - T_{RCAL}) > 8$ ns.

More timing cuts are implemented on the third level trigger system. Here the average event time is calculated with higher precision using an energy-weighting algorithm and tighter cuts are used. At the *TLT* the systematic time shift of the *ZEUS* detector with respect to the bunch crossing time which is calculated by the *C5* detector (see section 3.2.4) is taken into account.

The *TLT* also uses the error on the time average to reject events (see section 3.2.2 for $\sigma(T)$). Time averages are calculated by the *TLT* as error weighted averages and both the average time and the error on that time measurement are used:

One of the cuts is based on the global event time T_{global} which is an average over the time reported by all calorimeter channels. An event is rejected if T_{global} is outside a window around

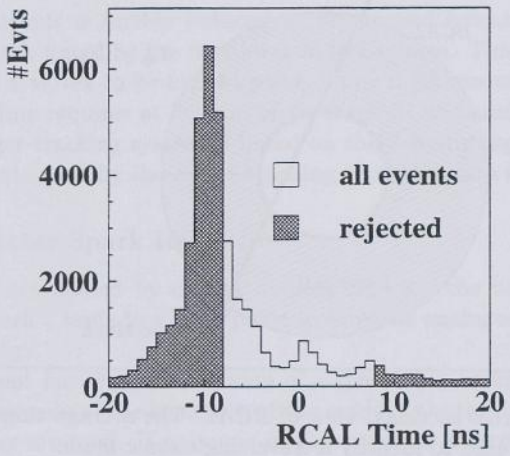

Figure 5.5: The distribution of the average *RCAL* time for events at the second trigger level. Events in the hatched area ($|T_{RCAL}| > 8$ ns) are rejected.

zero given by the maximum of 8 ns and $3\sigma(T_{global})$. This ensures that events with a poorly measured time average are still accepted. Table 5.2 list all timing cuts used at the *TLT*.

UCAL Cosmic Muon Timing Cut

Cosmic muons that traverse the *ZEUS* detector can cause high P_t to be measured by the calorimeter. Therefore these events are background to the charged current events. The rate of cosmic muons traversing the *ZEUS* detector is estimated to be about $20Hz$. This rate poses a significant problem in the *ZEUS* trigger system, so cosmic rejection is performed on both the second and third level trigger system.

A cosmic muon traversing *BCAL* can be recognized by calculating the average time in both the upper (T_{up}) and lower halves (T_{down}) of *BCAL*. For a cosmic muon the time difference, given the dimensions of *BCAL* (see figure 3.2) is significant: If the muon traverses *BCAL* from top to bottom in the center the average distance of the cells in the top to the bottom half is about 4 m which results in a time difference of about 12 ns.

The cut requires that there be no energy in either *FCAL* or *RCAL* and more than 1 GeV is deposited in both the upper and lower half of *BCAL*. Events are rejected if $|T_{up} - T_{down}| > 10$ ns. The cut is illustrated in figure 5.6.

Events are also rejected if $T_{FCAL} > 8$ ns, this rejects events where an out-of-time cosmic muon traverses the *FCAL* as well as events stemming from positron beam-gas collisions.

Table 5.2 lists the various timing cuts used on all trigger levels to reject events which have a time inconsistent with positron-proton collisions at the nominal interaction point.

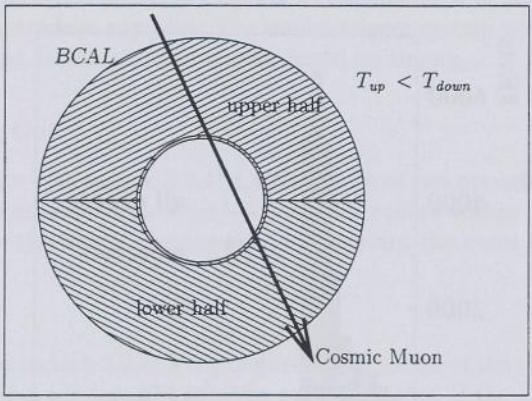

Figure 5.6: Schematic cross sectional view of *BCAL*. The average time in the upper and lower halves of *BCAL* can be used to identify a traversing cosmic muon.

Trigger Level	Timing Cut	rejected event type
Level-1	*Vetowall* timing cut.	beam-gas
	C5 timing cut.	beam-gas
Level-2	veto if $\lvert T_{RCAL}\rvert > 8\,\text{ns}$	beam-gas + cosmics
	or $\lvert T_{FCAL} - T_{RCAL}\rvert > 8\,\text{ns}$	beam-gas
	or $T_{FCAL} > 8\,\text{ns}$	beam-gas + cosmics
Level-3	veto if $\lvert T_{RCAL}\rvert < max(6\text{ns}, 3\sigma(T_{RCAL}))$	beam-gas + cosmics
	or $\lvert T_{FCAL}\rvert < max(6\text{ns}, 3\sigma(T_{FCAL}))$	beam-gas + cosmics
	$\lvert T_{global}\rvert < max(8\text{ns}, 3\sigma(T_{global}))$	beam-gas + cosmics

Table 5.2: The table lists the various timing cuts used by the *ZEUS* trigger system.

5.4.2 Second Level Trigger Beam-Beampipe Wall Collision Rejection

At the *SLT* $\not\!\!P_t$ is calculated both with the first ring of calorimeter cells around the *FCAL* beam pipe hole and without. An additional cut is placed on $\not\!\!P_t$ without the first ring of calorimeter cells to reject beam-beampipe wall collision events. This class of events is described in more detail in section 5.5.6. This cut which is placed at 8 GeV only removes very few events of the CC Monte Carlo event sample (1 %) because of the higher $\not\!\!P_t$ cut at the *FLT* and *SLT* level (see section 5.3).

5.4.3 Second Level Trigger Empty Event Rejection

The *FLT* calorimeter trigger sometimes triggers even though no energy is recorded by the readout system. This is due to noise in the calorimeter-*FLT* electronics. On the second level trigger system these events are rejected because they fail the $\not\!\!P_t$-cut which is repeated here: $\not\!\!P_t > 9\,\text{GeV}$.

5.4.4 Second Level Trigger Track Requirement

The rate of beam gas events is further reduced on the second level trigger by requiring that there be any charged track found by the first level trigger system. This requirement is not very different from requiring a vertex to be found by the offline track reconstruction program.

To find a vertex offline requires at least a single track to be found. The only difference is that the first level trigger tracking system is based on the Z-by-timing system rather than the more accurate *FADC* data used by the offline tracking reconstruction system.

5.4.5 *SLT* Calorimeter Spark Rejection

Photomultiplier sparks are caused by charge buildup between the base and the housing. A sudden discharge, a "spark", leads to a large pulse seen by the analogue readout electronics and fakes the deposit of energy.

The fact that an event has triggered because of a spark that occurred in a photomultiplier can easily be detected because of the structure of the readout electronics. For every calorimeter cell two photomultipliers are used. If only one of them records a large energy while the other one does not a spark is the most likely cause of the energy deposit.

The first level trigger system can not detect or reject a spark event because it operates on *analogue* sums of the photomultiplier pulses of a super-tower, in general some 10 photomultipliers. The FLT is not capable of distinguishing between an energetic particle that hit the super-tower and a spark in one photomultiplier.

The second level trigger system however has access to the full readout information but only on a per-cell, not a per-photomultiplier basis. The algorithm is based on the fact that for the calculation of average event times, the number of individual channels with energy above 200 MeV is known. An event is rejected if the event was only triggered by the *UCAL* in the *FLT* and if there is only a single channel with energy above 200 MeV and the energy in each of the calorimeter sections, when the energy of the cell with the sparking photomultiplier is removed, is small. A more detailed description of the spark rejection at the *SLT* can be found in [34].

5.4.6 Second Level Trigger Summary

Figure 5.7 shows the distribution of R_t for random events triggered in the unpaired and open bunches before and after the second level trigger cuts. The number of events in the open and unpaired bunches is reduced considerably.

5.4.7 *TLT* Cosmic and Halo Muon Rejection

At the third level trigger a more complicated muon finder algorithm is used [35]. Here a rough muon track reconstruction is performed and compared to central tracking detector tracks. Also, since for the muon traversing the calorimeter the time when it traversed a given cell can be measured, this is used to further improve the efficiency and purity.

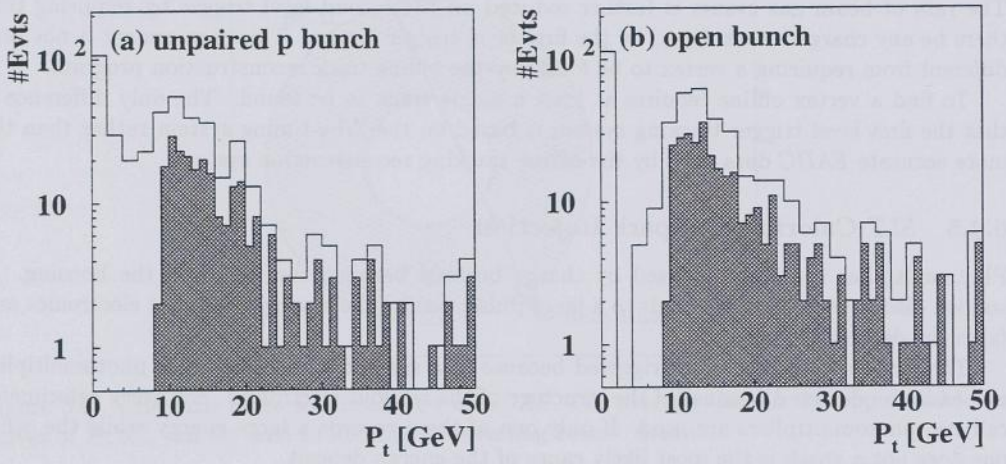

Figure 5.7: The distribution of P_t for events which have passed the first level trigger cuts and were triggered in the unpaired proton bunches (a) and open bunches (b) without (open histogram) and with (hatched histogram) the second level trigger cuts.

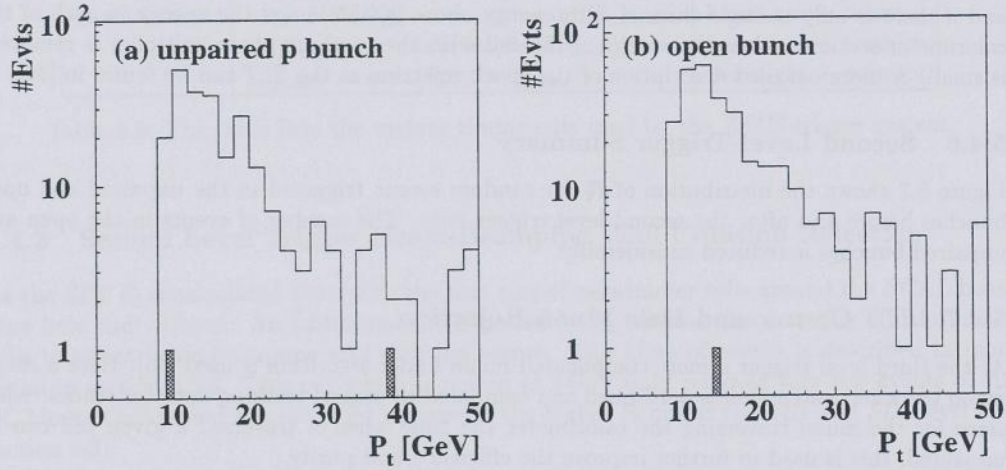

Figure 5.8: The distribution of P_t for events which have passed the first and second level trigger cuts and were triggered in the unpaired proton bunches (a) and open bunches (b) without (open histogram) and with (hatched histogram) the third level trigger cuts.

5.4.8 *TLT* Calorimeter Spark Rejection

The spark rejection strategy followed in the third level trigger system is to remove calorimeter cell data if the imbalance between the energies recorded by the two photomultipliers is too large: Test beam results show that for a particle hitting the calorimeter at any position and angle the cell imbalance which is defined as

$$|\frac{E_L - E_R}{E_L + E_R}|, E_L\ (E_R) : \text{Energy recorded in left (right) channel} \tag{5.1}$$

is smaller than 0.9. The third level trigger system simply omits all cells with an imbalance bigger than 0.9. This way, events with sparks are rejected.

5.4.9 Third Level Trigger Summary

Figure 5.8 shows the distribution of $\not{P}_t$ for random events triggered in the unpaired and open bunches before and after the third level trigger cuts. The number of events in the open and unpaired bunches is reduced considerably and only very few events are left. The data used for figure 5.8 are randomly selected and correspond only to a fraction of the running period. The data have to be scaled up by about 5×10^4 to reflect the true number of background events left in the sample.

5.4.10 Online Trigger Summary

In total 81540 events pass all trigger levels. Figure 5.9(a) shows a distribution of $\not{P}_t$ for the Monte Carlo event data without any cuts (open histogram) and after all trigger cuts (hatched histogram). Figure 5.9(b) shows the efficiency of the *ZEUS* online trigger system depending on $\not{P}_t$: The *ZEUS* trigger is about 90% efficient for charged current events with $\not{P}_t > 15\,\text{GeV}$. Figure 5.10 shows the $\not{P}_t$ spectrum for Monte Carlo and data events normalized to the same luminosity. Clearly there are still a lot of background events present in the data sample. These are rejected during the offline selection process to be discussed below.

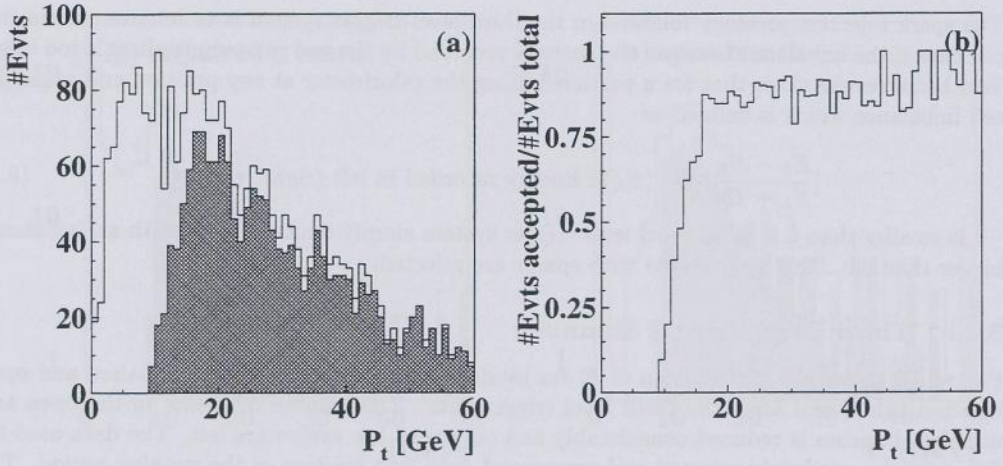

Figure 5.9: Figure (a) shows the distribution of P_t for the Monte Carlo data sample without any cuts (open histogram) and after the *ZEUS* online trigger cuts (*FLT*, *SLT* and *TLT*). Figure (b) shows the turn on of the *ZEUS* trigger for charged current events: *ZEUS* is about 90% efficient for charged current events with $P_t > 15\,\mathrm{GeV}$.

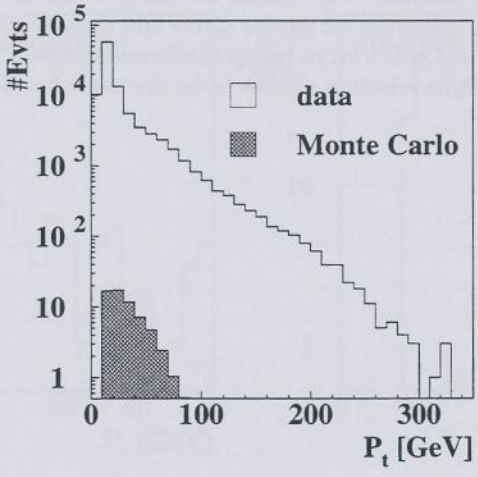

Figure 5.10: The distribution of P_t for the data after the trigger cuts (*FLT*, *SLT* and *TLT*) (open histogram) and for Monte Carlo events (hatched histogram) normalized to the same luminosity. It is clear that there are still a lot of background events in the sample.

5.5 Offline Charged Current Event Selection

5.5.1 Introduction

The online trigger uses algorithms which are safe and suitable for a wide range of different physics event samples. It is for this reason that they can not reject all non e-p background, as can be seen in figures 5.8 and 5.10. Further rejection is needed. All cuts are described in the following subsections in the order they are applied to the data.

5.5.2 Detector Effects

For a successful analysis the *ZEUS* sub-detectors whose data are used in the analysis have to work properly. This is determined by data quality monitoring, a procedure in which the detector response to normal or special test events is monitored and compared to expectations. As output a list of data taking runs is produced for which the detector behaved as expected. Only these runs are used in the analysis. The runs accepted correspond to a total luminosity of $2.573\,\mathrm{pb}^{-1}$, i.e. 78 % of the total.

5.5.3 Calorimeter Noise and Readout Holes

The *ZEUS* calorimeter readout system has been designed and developed such that the effect of electronics noise is minimized, but electronics noise exists and can cause large P_t. Data taking periods during which the calorimeter electronics noise caused cells to pass the offline threshold cuts are excluded for this analysis.

The *UCAL* readout system posesses two independent readout channels for a single cell. Thus the number of "dead" cells is kept very small. Data taking periods during which a readout cell in the *EMC* section of the calorimeter was inoperational, i.e. with both channels of the same cell dead, are excluded for this analysis. This is done in order to reduce the possibility for a neutral current event to fake a charged current event when the scattered positron hits this dead cell.

5.5.4 Vertex Requirement

The calculation of the event kinematics requires that for the events a vertex has been reconstructed. This is the first cut applied to the event data which also removes beam-gas and cosmic muon events. The total number of events excluded by this cut is 76252 events and 5288 events remain in the sample.

5.5.5 Calorimeter Sparks

Events due to *UCAL* sparks are rejected on the second and third level trigger through special algorithms (see section 5.4.6 and section 5.4.8) which are safe for all types of physics events that occur at *HERA*. Consequently the rejection is not fully efficient. Moreover the trigger system does not take into account channels which are switched off because of a malfunction. For such a channel the imbalance (see (5.1)) is zero and so the cell (and therefore the event) is not rejected. Since the energy of the other channel is unknown it is not safe to simply assume the energy in the other channel is zero and thus the imbalance 1 because this would simply remove all cells with one dead channel. For the charged current analysis it is useful to consider why a spark event enters the charged current event sample: It is because the spark channel increases the P_t

of the event. The spark events where the spark occurred in a cell with one disabled readout channel can therefore be found with the following algorithm: First the cell with maximum P_t is identified. If the cell imbalance (see section 5.4.8) is bigger than 0.7 or if one of the channels is disabled and the event would have $P_t < 9\,\text{GeV}$ (the trigger cut) if that cell was removed, the event is rejected.

Figure 5.11 shows the P_t distribution for all events that have passed the cuts described so far if the spark cell is removed. The events at $P_t < 9\,\text{GeV}$ are rejected.

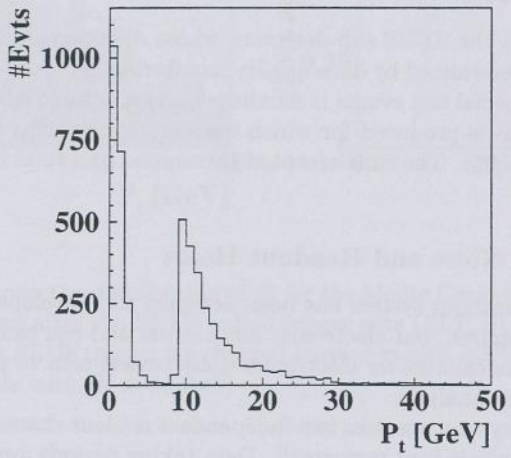

Figure 5.11: The figure shows the P_t distribution for all events that have passed the cuts described so far if the spark cell is removed. The events at $P_t < 9\,\text{GeV}$ are rejected.

Through this cut 3518 events are rejected and 1770 events remain in the sample.

5.5.6 Proton Beam Wall Collisions

Off-axis protons from the proton beam can collide anywhere in *HERA* with the beam pipe or other objects. Due to the final bend and focus of the machine magnets before the intersection region it is possible that these interactions take place at such a position that they cause energy deposits which pass all timing cuts and pass the trigger rejection cuts.

Events stemming from beam-wall collisions constitute a particularly difficult background because the vertex of such collisions is not near the center of the beam pipe but displaced at the beam-pipe wall. As a result particles which would disappear down the forward beam pipe hole for a beam-gas event can now hit the detector and fake large $\not{P}_t$. This is illustrated in a schematic view in figure 5.12. Also an off-axis proton intrinsically has non negligible $\not{P}_t$.

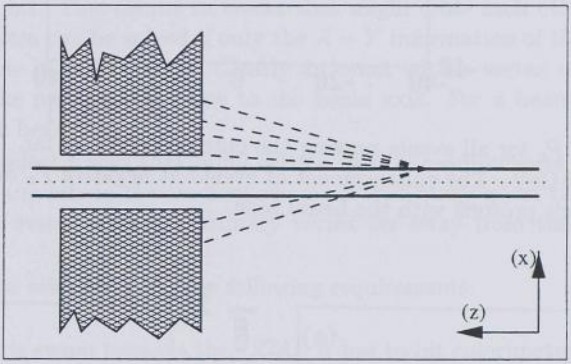

Figure 5.12: Schematic view of a beam wall collision event. Shown is the beam pipe (parallel lines) with the nominal beam trajectory (dotted line) and a part of the *FCAL* (hatched structures). The vertex is displaced in X-direction by the radius of the beam pipe. As a result the calorimeter measures a P_x, much higher than the true P_x.

The second and higher level triggers reject a large fraction of these events by calculating $\not{P}_t$ without the first ring of calorimeter cells around the *FCAL* beam pipe hole and requiring that this value be bigger than 8 GeV. However, a small fraction of events still passes this criterion.

This can be seen when the transverse momentum in the X and Y direction is plotted. In figure 5.13 the distribution P_y versus P_x for all events that pass all cuts described so far is shown. The distribution should be symmetric around $(0,0)$ but a clear enhancement is visible around $P_x = -20\,\text{GeV}$ and $P_y = 0\,\text{GeV}$ i.e. in the plane of the *HERA* machine.

The fact that this enhancement is due to off-axis protons colliding with the beam pipe can be shown using the event vertex. The vertex reconstruction normally uses a pseudo beam particle at $(x, y, z) = (0, 0, undefined)$. For the primary vertex finding all tracks that are incompatible with this "pseudo beam particle" are discarded. This method improves the reconstruction of the primary vertex position in particular for events with very few charged particle tracks but introduces a bias for events with primary event vertex not near the beam axis.

In figure 5.14 (a) the vertex position in the $X - Y$ plane is shown when the vertex reconstruction is run without this "pseudo beam particle".

Most events have the primary vertex still in the center but now there is a clear enhance-

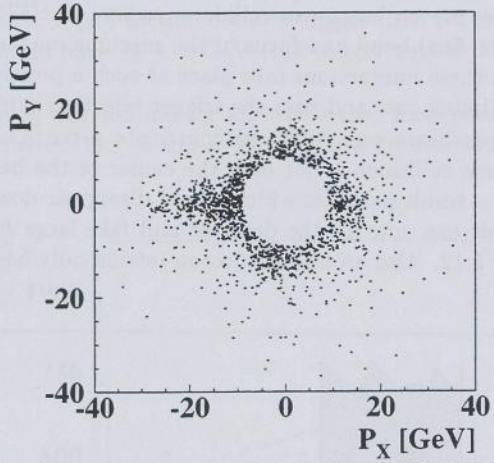

Figure 5.13: P_y vs. P_x for all events passing the cuts described so far. The plot only contains events with $P_t < 40\,\mathrm{GeV}$. The enhancement of events at negative P_x and moderate P_y is due to collisions of off-axis protons with the beam pipe.

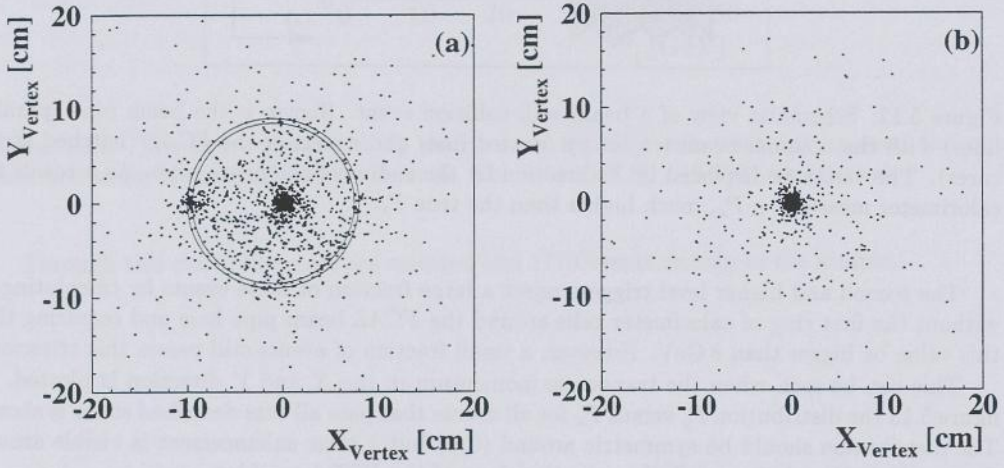

Figure 5.14: Vertex position in the $X-Y$ plane for all data events (figure (a)) and Monte Carlo events (figure (b)) passing the cuts described so far. The vertex reconstruction is performed without a "pseudo beam particle", thus allowing for vertices far away from the beam axis. In figure (a) an enhancement of the number of events can be observed near the beam pipe (The beam pipe is indicated by two circles.). The distribution for the Monte Carlo events (figure (b)) shows that the reconstructed vertex is not always close to the beam axis. It is therefore not possible to use the vertex position as a cut criterion.

ment of events visible around $X = -10\,\text{cm}$ and $Y = 0\,\text{cm}$. In fact there is an enhancement of events along a circle with center at $X = -1\,\text{cm}$ and $Y = 0\,\text{cm}$ and radius of 9 cm.These are the coordinates of the inner beam pipe in ZEUS. The effect is clearly visible for all running periods.

The vertex calculated without the beam particle can not be used for rejecting beam wall events, however. In figure 5.14 (b) the vertex distribution is shown for charged current Monte Carlo events that pass all the cuts described so far. This distribution indicates that one should not use the vertexing to reject beam wall events. The problem stems from the topology of charged current events: Most charged current events are single jet events and for those almost all charged particles are scattered off within a narrow cone. For such a configuration the tracking resolution has to be very good to assure a good vertex resolution if the pseudo beam particle is not taken into account.

But for small scattering angles the track Z resolution is rather poor because only few, if any, stereo layers are hit. This results in tracks that might cross each other far away from the beam axis. This problem can be solved if only the $X-Y$ information of the tracks is used. The resolution in this plane is much better. Clearly an event with a vertex on the beam axis will have most of its tracks passing very close to the beam axis. For a beam wall event only few tracks are close to the beam axis.

It is necessary to select tracks that fulfill certain quality requirements: For some beam wall events there are so many hits in the tracking chamber that many ghost tracks are constructed. The same is true for events with the primary vertex far away from the nominal interaction region.

Good tracks can be selected using the following requirements:

1. When the track is swum towards the *UCAL* it has to hit calorimeter cells with energy.

2. The track has to be well within the *CTD*: $45° < \theta < 135°$.

3. The track fit quality has to be good: $PROB(\chi^2, NDF) > 0.1$.

4. Track momentum $P > 0.1\,\text{GeV}$.

5. Radius of curvature of track $R > 20\,\text{cm}$.

Because of the homogeneous magnetic field inside *ZEUS* parallel to the beam axis a track can be approximated by a helix in three dimensions or a simple circle in the $X-Y$ plane. One of the parameters of the helix is the distance of closest approach ρ_H of the helix to the beam axis as depicted in figure 5.15.

In figure 5.16 ρ_H is shown for good tracks in charged current Monte Carlo and real data. Most of the tracks in the Monte Carlo event sample come closer than 0.5 cm to the beam axis. For real data many tracks stay far away from the beam axis.

In figure 5.17 the ratio of good tracks that are closer than 0.5 cm to the beam axis over the total number of good tracks is shown for charged current Monte Carlo data and real data.

Events with a ratio bigger than 0.4 are kept. Figure 5.18 shows the distribution P_y versus P_x for all events which pass the cut described above. The enhancement visible in figure 5.13 has disappeared.

Through this cut 1077 events are rejected and 693 events remain.

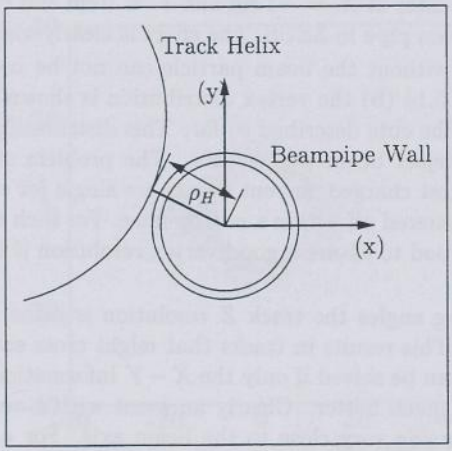

Figure 5.15: A track in the central tracking detector can be approximated by a helix in three dimensions or a circle in the $X - Y$ plane as shown in this figure. Shown is also one of the parameters of the helix, ρ_H, the distance of closest approach to the beam axis.

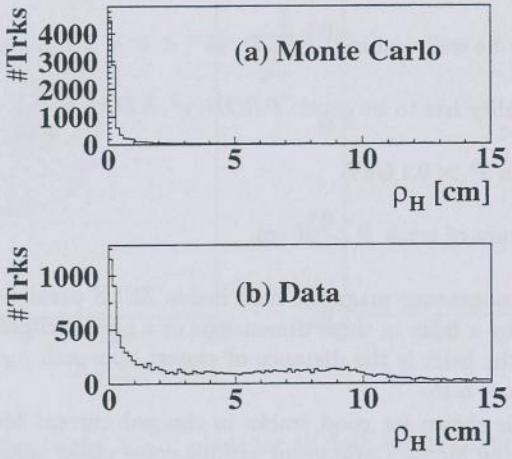

Figure 5.16: Closest approach of the track helix to the beam axis for all "good tracks" in charged current Monte Carlo events (a) and real data (b). For charged current Monte Carlo events most tracks come very close to the beam axis while for real data many tracks stay far away from the beam axis.

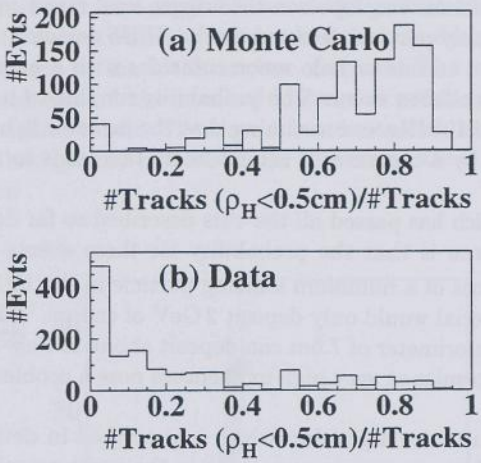

Figure 5.17: Ratio of number of good tracks that come closer than 1 cm to the beam axis over the total number of good tracks for Monte Carlo (a) and real data events (b). Events with a ratio bigger than 0.4 are kept.

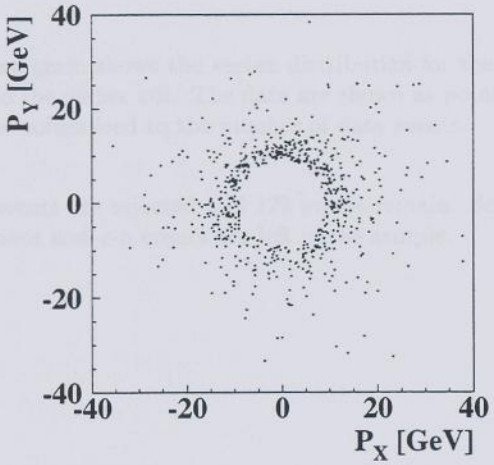

Figure 5.18: P_y vs. P_x for all events after applying the beam wall collision cut described in the text. The enhancement of the number of events visible in figure 5.13 has disappeared.

5.6 Offline Cosmic and Halo Muon Rejection

The muon rejection algorithms employed on the trigger level reject most of the events in which a traversing muon is the only particle detected by the *ZEUS* detector. However, there are events in which the traversal of a cosmic or halo muon coincides with a beam-gas background or even genuine positron proton collision event. The probability for this to happen is not small: Given the bunch crossing rate of 10 MHz and assuming that the detector is hit by a beam related event at a rate of 150 kHz and by a cosmic at a rate of 20 Hz this leads to a rate of overlap events of 0.3 Hz.

The event sample which has passed all the cuts described so far does not contain that many overlap events. The reason is that the probability for these events to have high $\not{P}_t$ is small: Given the mean energy loss of a minimum ionizing particle in the *UCAL* $\frac{dE}{dX} = 20\frac{MeV}{cm}$ a muon that traverses $1m$ of material would only deposit 2 GeV of energy. A halo muon which traverses the entire length of the calorimeter of $7.6m$ can deposit about 15 GeV and can then indeed cause $\not{P}_t > 9$ GeV. However, cosmics at very high momentum pose a problem because bremsstrahlung can cause large $\not{P}_t$.

A sophisticated muon finder algorithm which is described in detail in chapter 6 is used to reject the cosmic and halo muon events remaining in the event sample.

Through this cut 489 events are rejected and 204 events remain. After this cut no events remain in the unpaired bunches. This indicates that the background due to non e-p collisions is small.

5.7 Vertex Cut

Events that survive the cuts so far have a reliable vertex determination. In figure 5.19 the vertex distribution is shown for the events which have passed all the cuts described so far together with Monte Carlo events normalized to the total number of events. The vertex distributions agree. The data show a large peak around the nominal interaction point and another peak close to 70 cm due to the proton satellite bunch. There are a few events with large $|z|$ which are probably due to remaining non e-p background in the sample. To remove these events we select events if $-25\,\text{cm} < Z_{vtx} < +30\,\text{cm}$.

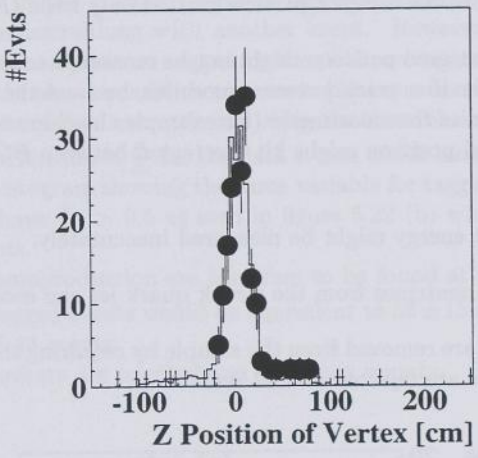

Figure 5.19: The open histogram shows the vertex distribution for the Monte Carlo data after applying all the cuts up to the vertex cut. The data are shown as points with statistical errors. The Monte Carlo data are normalized to the number of data events.

Through this cut 25 events are rejected and 179 events remain. Scanning of the remaining events shows that no obvious non-e-p events are left in the sample.

5.8 Background from Neutral Current Events

The occurance of neutral current events in the sample can be demonstrated by the $(E_{tot} - P_z)$-distribution in figure 5.20. The entries in the peak around 50 GeV correspond to neutral current events while the peak at low $(E_{tot} - P_z)$ corresponds to charged current and photo-production events.

Neutral current events can fake large $\not{P}_t$ for several reasons:

- High momentum particles of the proton remnant jet can escape through the beam pipe hole, carrying substantial P_t. Most of the NC-background events are in fact of this type and they cause the peak around 50 GeV in figure 5.20. For these events $(E_{tot} - P_z)$ is well measured because the escaped particle carried only little $(E_{tot} - P_z)$.

- The energy of the scattered positron might not be measured correctly because the positron enters the calorimeter in a crack between modules, because the scattered positron might hit an inactive region of the calorimeter (for example the chimney region in the *RCAL*) or because the scattered positron might hit the region between *BCAL* and *RCAL* or *BCAL* and *FCAL*.

- The struck quark jet energy might be measured inaccurately.

- Final state muon or neutrinos from the struck quark jet can escape the detector.

Neutral current events are removed from the sample by requiring that $E_{tot} - P_z < 35\,\text{GeV}$. Through this cut 87 events are rejected and 92 remain.

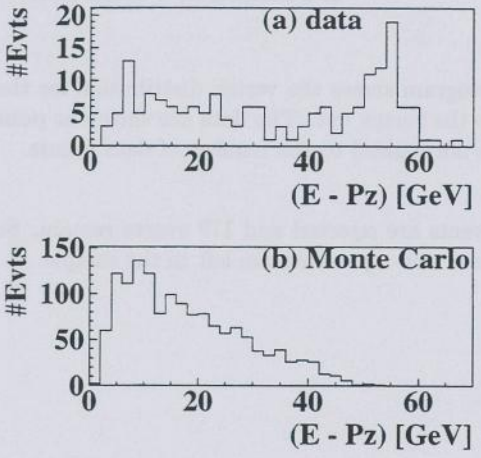

Figure 5.20: $(E_{tot} - P_z)$ for the events which pass all the cuts so far for data (upper histogram) and Monte Carlo (lower histogram). The entries in the peak around 50 GeV correspond to neutral current events while the entries at lower $(E_{tot} - P_z)$ correspond to charged current and photoproduction events.

5.9 Background from Photoproduction Events

The occurance of photoproduction background events in the sample can be shown with the luminosity monitor. In figure 5.21 the P_t distribution of the events remaining in the sample are shown. Of these 11 events are tagged by the luminosity monitor positron tagger as genuine photoproduction events. These are shown as a hatched histogram. We tag an event as photoproduction if $(E_{tot} - P_z)$ of that event, together with the energy detected in the luminosity monitor positron tagger (see section 3.2.5) is close to $2E_e$:

$$40\,\text{GeV} < E_{tot} - P_z + 2E_{\text{LumiElTagger}} < 70\,\text{GeV} \tag{5.2}$$

and no accompanying γ in the photon tagger is observed which excludes that these events stem from overlay of bremsstrahlung with another event. However, only about 20 % of the photoproduction events have a positron tagged by the positron tagger because of acceptance, so it is not possible to use the above condition to remove photoproduction background.

The background can be shown more clearly using the distribution in the variable $\frac{P_t}{E_t}$. Figure 5.22(a) shows the distribution of $\frac{P_t}{E_t}$ for the data events which have passed the cuts described so far with the hatched histogram showing the same variable for tagged photoproduction events. Charged current events have $\frac{P_t}{E_t} > 0.5$ as seen in figure 5.22 (b) which shows the distribution for the Monte Carlo events.

The events due to photoproduction are therefore to be found at low $\frac{P_t}{E_t}$: We find 43 events with $\frac{P_t}{E_t} < 0.5$. The 11 tagged events would be equivalent to 55 ± 15 in total which is consistent with the measurement of 43 events.

Through this cut 43 events are rejected and 49 events remain.

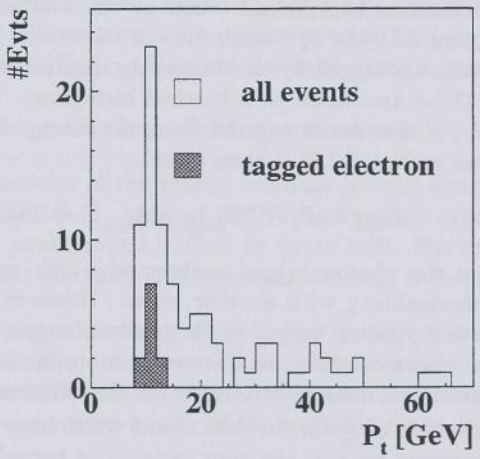

Figure 5.21: P_t for the data events remaining in the sample. The hatched histogram shows of those events the ones for which 40 GeV $< E_{tot} - P_z + 2E_{\text{LumiElTagger}} <$ 70 GeV, they correspond to photoproduction events.

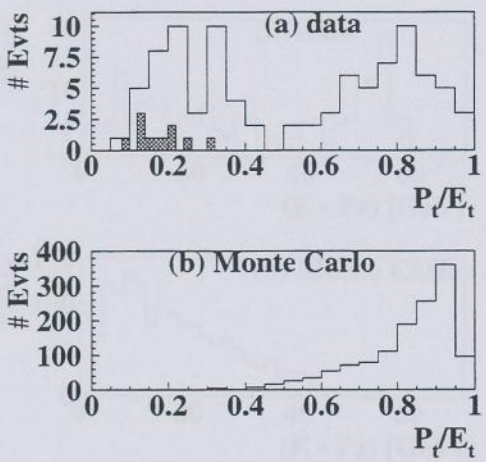

Figure 5.22: The distribution of $\frac{P_t}{E_t}$ for events that have passed the selection cuts described in section 5 for data (a) and Monte Carlo events (b). The hatched histogram in figure (a) shows tagged photoproduction events still in the data sample. Those events have been selected by requiring 40 GeV $< E_{tot} - P_z + 2E_{\text{LumiElTagger}} <$ 70 GeV.

5.10 Event Selection Summary

Table 5.3 gives a summary of the various selection steps required to select the final charged current event sample. It is interesting to note that for the Monte Carlo events the by far largest individual reason for loss of acceptance stems from the *FLT*. This is not a surprise, however, considering that the Monte Carlo events have been generated starting at a very low Q^2 of $10\,\mathrm{GeV}^2$. The P_t cut at the *FLT* corresponds to a cut at about $100\,\mathrm{GeV}^2$ to $300\,\mathrm{GeV}^2$.

Trigger Level	MC % accepted of total	Data % accepted in this step	Data % accepted of total	Data # remaining
Level-1	69.8	100.0	100.0	107560345
Level-2	63.2	2.1	2.1	2283932
Level-3	63.2	3.5	7.5×10^{-2}	81540
Vertex Req.	62.4	6.4	4.9×10^{-3}	5288
Spark	62.4	33.5	1.6×10^{-3}	1770
Beam-Wall	58.0	39.2	6.4×10^{-4}	693
Cosmic & Halo	58.0	29.4	1.9×10^{-4}	204
Vertex Cut	50.3	87.7	1.7×10^{-4}	179
Neutral Current	45.8	51.4	8.5×10^{-5}	92
Photoproduction	44.7	53.3	4.5×10^{-5}	49

Table 5.3: Acceptance of the different trigger and selection steps. Shown are only numbers for runs for which the detector was in a good state (see section 5.5.2).

Chapter 6

Muon Finder

6.1 Introduction

The charged current event sample is contaminated with overlapping events. These can either be due to cosmic ray or "halo" muons together with a normal *e-p*-interaction or beam-gas event.

Halo muons are muons created by interactions upstream of the detector, which traverse the detector from *RCAL* to *FCAL* at a large radius. These halo muons can produce large P_t because they traverse the *BCAL* parallel to the scintillator plates. The pulse height registered can then be many factors larger than one would expect from a muon, due to the significantly increased sampling along the muon track.

Cosmic muons arrive predominantly from above and traverse the detector from top to bottom. These are in general no problem as the minimum ionizing energy deposit will not generate a large transverse momentum. There are exceptions to this though. A cosmic muon can enter *FCAL* or *RCAL* or to a lesser extent *BCAL* from above and again travel parallel to the scintillator plates, giving large apparent energy, and then in general as they are "off center" a large P_t. Another possibility for a cosmic muon to produce large P_t is that the high energy muon produces a bremsstrahlung photon in the *UCAL*, before exiting the detector. Also events with multiple muon tracks form a significant background.

Figures 6.1 through 6.3 and figure 6.8 show examples of the different background categories mentioned above.

These events can not be detected by the algorithms employed so far, as these algorithms assume that the halo muon or cosmic is alone in the detector. When the halo or cosmic muons overlay a genuine *e-p* event the information from the underlying *e-p*-event masks the information of the muon and thus render the algorithms useless.

The muon finder (MUFFIN) described in this chapter attempts (and succeeds) to find these muons. The principle of the program is to search for a topology of calorimeter cells within normal events, which is consistent with a muon traversing the detector. The characteristic topology is a series of aligned cells (i.e. high energy muons traverse the detector in straight or almost straight lines). When a muon candidate is found the event is removed from the CC sample if by removing the muon candidate energy deposits the event no longer passes the CC selection cuts. The detector elements that are important in the muon finder are the muon chamber system (*FMUON*, *BMUON* and *RMUON*), the calorimeter (*FCAL*, *BCAL* and *RCAL*) and the central tracking system (*CTD*).

In current physics analyses visual scanning is an accepted method to remove this source of background. This method has several disadvantages though:

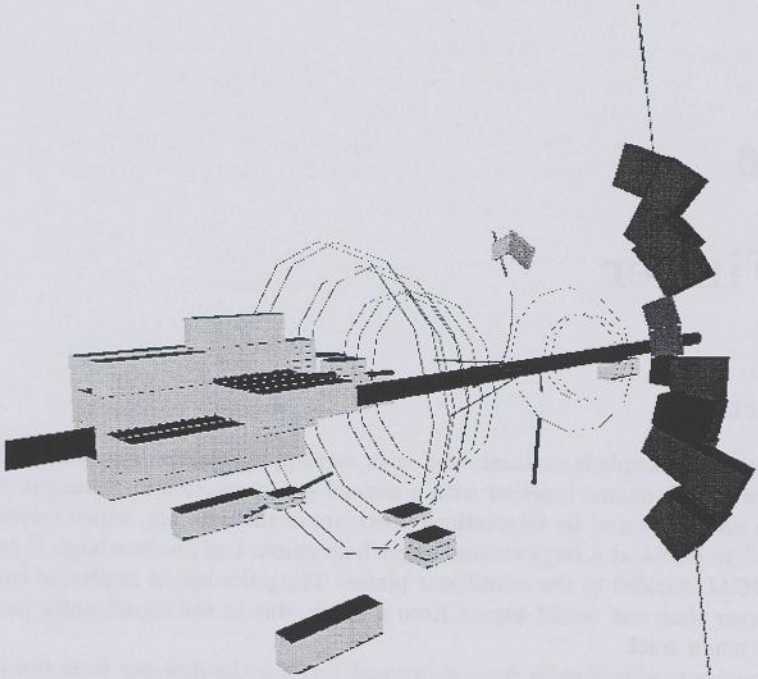

Figure 6.1: Example of a cosmic muon traversing the *ZEUS* detector together with what appears to be a beam-gas event. On the left side the cells surrounding the *FCAL* beam pipe region are shown. On the right side the cosmic muon which traverses the *BCAL* can be seen. In the middle of the picture tracks stemming from the beam-gas event are drawn.

- The number of events a physicist can scan for an analysis is limited.
- Visual scanning has a high efficiency but the efficiency is not constant.
- It is difficult to estimate the efficiency and purity of the visual scan method.

The following will be a detailed description of the muon finder program.

6.2 The Muon Finder Algorithm

A traversing muon deposits energy in detector elements along its flight path. The pattern of hit detector elements is usually isolated from the overlap event because of the high granularity of the *ZEUS* detector and the low occupancy of most events. During visual scan the trained physicist identifies such a pattern easily because it usually forms a straight line. [1]

[1] It would sound like a good idea to use a specialized pattern finder program based on a neural net to identify a cosmic muon event. This however is very difficult because the net would be far too big - it would have to contain all *ZEUS* detector elements as entry neurons and would thus require a huge number of cosmic muon events to

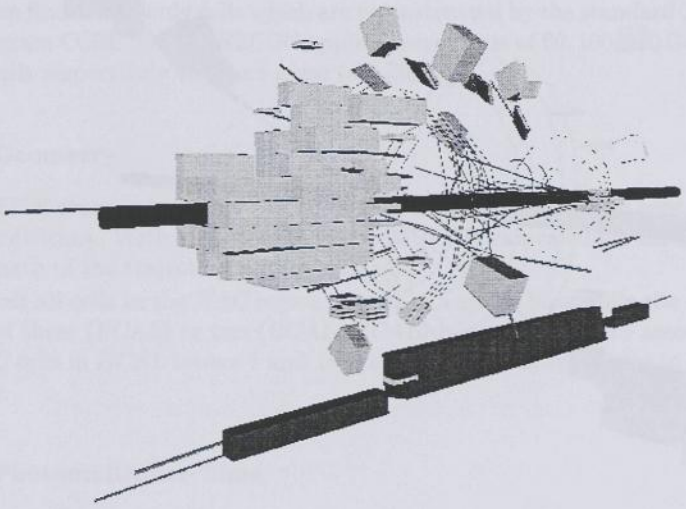

Figure 6.2: Example of a halo muon traversing the *ZEUS* detector all the way from *RCAL* through *FCAL* together with what appears to be a beam-gas event, originating inside the detector volume.

MUFFIN tries to find all patterns of hit detector elements which form a straight line. It uses tracks from the muon detectors and calorimeter condensates (see section 6.3.1) to find these patterns. For each pattern a set of parameters is calculated and compared to the parameters describing a traversing muon. If MUFFIN were to use a brute force method and just calculate all combinations of tracks and condensates it would take too much time to evaluate an event. Instead MUFFIN uses several tricks to speed up the search for a candidate pattern:

- MUFFIN stops after a single traversing muon has been identified by the trigger conditions.
- MUFFIN temporarily removes all detector hits which belong to a traversing muon candidate from the event. Only if the remaining event fails the trigger conditions for the event (e.g. the CC $\not{P}_t$ cut), the candidate pattern is further evaluated. This algorithm is based on the assumption that the event consists of a background event that would normally not pass the trigger and a traversing muon which is responsible for the event passing the trigger.
- MUFFIN uses ray tracing algorithms to speed up the most time consuming part of the processing which is to find the cells which are hit by a muon trajectory. Upon initalization

train. But then it would only be able to recognize single cosmic muon events, a detection of a cosmic muon overlapping with a beam-gas or true collision event would be extremely difficult.

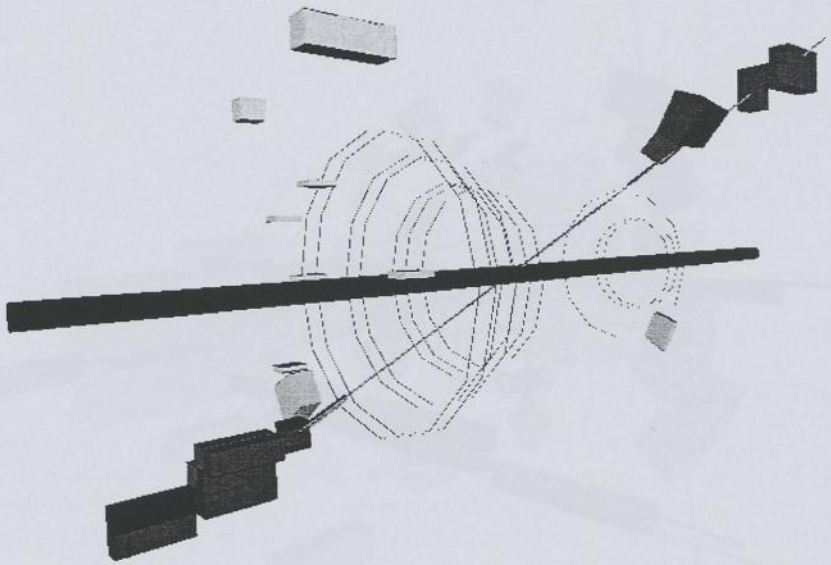

Figure 6.3: Example of a cosmic muon traversing the *ZEUS* detector. The muon hit cells in *RCAL*, *BCAL* and *FCAL*. Its trajectory passes through the beam-pipe. The reason that this event was identified and rejected by MUFFIN is that the timing of the two condensates was compatible with a particle traveling between them.

MUFFIN creates 27 evenly distributed volumes "containers" (three in each coordinate direction) which contain the entire calorimeter. Each of these volumes contains again 27 volumes, "boxes". Each of those boxes contains calorimeter cells. When MUFFIN tries to find the cells hit by a muon it first checks which "containers" are hit by the muon and then inside each hit container it checks which "boxes" are it. Only then will it check cell by cell.

In order to test whether a cell is hit MUFFIN has two radii available, the radius of the largest sphere around the cell center that is fully contained in the cell r_{inner} and the radius of the smallest sphere around the cell center that contains the cell r_{outer}. By testing the distance of the cell center to the trajectory d MUFFIN can determine quickly whether the trajectory hits the cell ($d <= r_{inner}$) or not ($d > r_{outer}$). Only for the remaining cases ($r_{inner} < d <= r_{outer}$) MUFFIN performs a precise geometric check testing whether the trajectory hits any of the cells surfaces.

6.3 Muon Finder Input Data

6.3.1 *UCAL* Cells

Energy Cuts

The muon finder uses only cells which are reconstructed by the standard *ZEUS* offline reconstruction program CCRECON. CCRECON applies energy cuts of 60, 100, 110 GeV for *EMC*, *HAC*1 and *HAC*2 cells respectively to reject noise (see [36]).

UCAL Geometry

For MUFFIN every calorimeter cell consists of several boxes which contain the uranium scintillator sandwiches. With this representation MUFFIN can calculate for a traversing particle the exact length of the trajectory within each cell.

Almost all cells in the *HAC* region consist of a single box, while the cells in the *EMC* region consist of three (*FCAL*) or two (*BCAL*, *RCAL*) boxes to take into account the *HES* gap. Only the *HAC* cells in *BCAL* towers 1 and 14 are constructed of two boxes to construct their volumes precisely.

UCAL Photomultiplier Time

The calorimeter data as stored by the reconstruction program contain the time reported by the digital cards. A time-of-flight correction has been applied to this time online so that the reported time is zero for a particle coming from a collision at the nominal interaction point. This is ideal for the trigger system because it can simply select good events by requiring the average event time to be close to zero.

A traversing muon however is obviously not coming from the nominal interaction point, so in order to allow a measurement of the velocity of the muon the correction is undone.

Whenever calculations involving the time measured in the calorimeter are performed MUFFIN uses the individual photomultiplier time as well as the energy reported by this photomultiplier to calculate an error on the time. For the error calculation it uses the same formula that is used inside the standard offline reconstruction program (see (3.1)).

UCAL Readout Holes

MUFFIN considers the calorimeter to consist only of the good cells in an event: If a muon traverses an inactive cell MUFFIN does not expect energy from this cell.

UCAL Photomultiplier Sparks

Standard analyses of *ZEUS* data usually remove all calorimeter cells with a large imbalance (see (5.1)) from the event data. MUFFIN instead keeps all those cells. The reason is that the probability for a coincidence of a spark and a background muon is very low. So if there is a cell with large imbalance this is more likely due to the muon than to a spark, for example because of a muon bremsstrahlung near the wave length shifter.

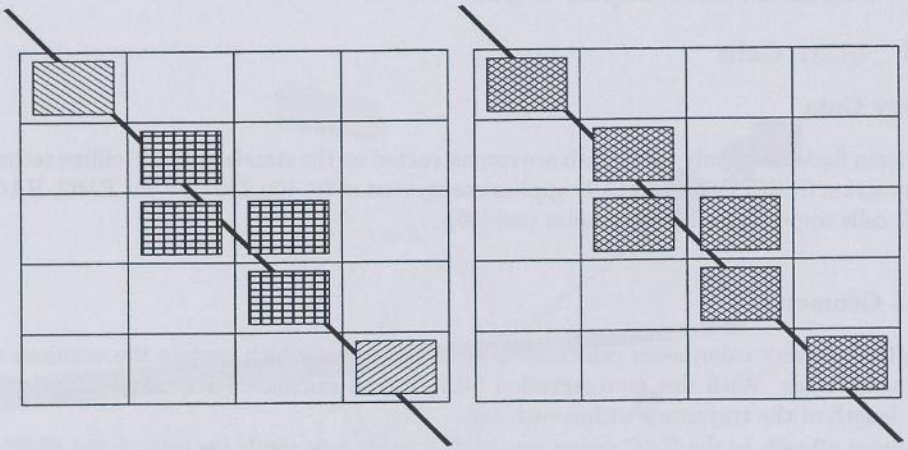

Figure 6.4: Schematic view of a muon traversing *UCAL* cells. From the cells with enough energy to pass the noise cuts CCRECON (on the left) constructs three condensates as shown by differently shaded boxes while CONDENSOR (on the right) only constructs a single condensate.

UCAL Condensates

A "condensate" is an object which contains calorimeter cells which are clustered together. The standard *ZEUS UCAL* reconstruction program CCRECON (see [36]) creates condensates of neighboring cells if they have a common surface.

MUFFIN uses a separate program "CONDENSOR" to construct condensates. Here cells are also neighbors if they touch each other on a common edge or corner (see figure 6.4).

In CONDENSOR the extreme towers of *BCAL* can also have neighbors in *FCAL* or *RCAL*. CONDENSOR knows of two different neighborship relations: Cells are neighbors when either their projections on the $X-Y$ plane overlap or if a straight line through $(X=0,Y=0,Z=0)$ hits both cells. Unlike CCRECON CONDENSOR does not remove condensates with little energy. CONDENSOR also performs a $3-D$ line fit to the cell centers and uses this line to calculate shape parameters such as the "hit ratio" which is the ratio of the number of cells hit by the trajectory over the total number of cells. These parameters are used by the muon finder to speed up calculations.

6.3.2 Muon Chamber Tracks

Barrel and rear muon detector detector tracks are already used in the trigger system to reject some of the cosmic muon background events online. Still many of the cosmic or halo muon events contain tracks of the muon detectors and it turns out that all information coming from the muon detectors is very useful for MUFFIN.

MUFFIN uses full tracks from the *FMUON*, *BMUON* and *RMUON* detectors. A full track has valid information in all 3 coordinates.

MUFFIN also uses tracks for which only wire or strip readout is available Wire or strip readout tracks are only available from *BMUON* and *RMUON*. For these tracks one of the coordinates

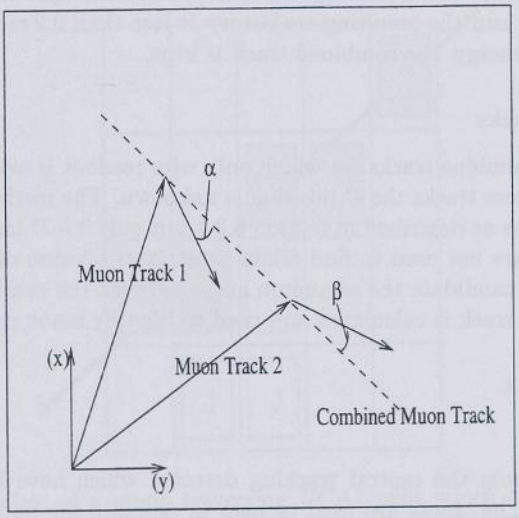

Figure 6.5: The figure shows schematically (in 2D) how MUFFIN combines two muon chamber tracks to one. A muon track consists of an offset and a direction vector, MUFFIN makes a combined muon track as track connecting the two offset vectors but checks if the angles α and β are not too large.

is not known.

Combined Full Muon Chamber Tracks

MUFFIN tries to find combinations of two full muon tracks that are compatible with the combined track as shown in figure 6.5. It calculates a straight line between the two offset vectors of the tracks. This straight line is a better approximation of the muon trajectory than that of the individual muon tracks since the two offset vectors are known to much higher precision than the direction vectors. MUFFIN then removes combined muon tracks for which the angle between the combined track and the individual tracks' direction vector is too large (angles α and β in figure 6.5 have to be less than $10\,^{\circ}$).

Combined Full and Wire Tracks

MUFFIN tries to find combinations of a full muon track with a wire readout track. The wire readout tracks are track segments for which one coordinate is unknown. If the track is found in the barrel region this unknown coordinate is Z, if the track is in the rear region the unknown coordinate is X. MUFFIN tests whether for both tracks the angle between the track and the combined track is smaller than $15\,^{\circ}$. This test is performed in the plane where the coordinates and the direction vectors are known, so either in the X-Y plane for wire tracks from the barrel region or the Y-Z plane for the rear region.

For the combined tracks the missing coordinate is estimated from the full track. Then MUFFIN performs a minimization (MINUIT) [37] using the calorimeter information. It maximizes

the sum of the track trajectories through all calorimeter cells that have energy. If the angle between the full track and the resulting trajectory is less than 0.2 rad and the track hits any calorimeter cells with energy, the combined track is kept.

Combined Wire Tracks

MUFFIN also tries to combine tracks for which only wire readout is available if these tracks are in the *BMUON*. For these tracks the Z position is unknown. The method is the same as is used for combining full tracks as described in section 6.3.2 but only $2-D$ information is used. These combined wire tracks are not used to find muon candidates because of the missing coordinate. Instead for each muon candidate the minimum angle between the candidate trajectory and the $2-D$ combined muon track is calculated and used to identify muon candidates.

6.3.3 Inner Tracks

CTD Tracks

MUFFIN uses tracks from the central tracking detector which have been projected onto the *UCAL* inner surface. The tracks are used to help to separate the pattern of a true traversing muon from a genuine physics or beam gas event. MUFFIN requires the track momentum to be bigger than $1\,\mathrm{GeV}/c$ to select only straight tracks.

Vertex

MUFFIN uses the event vertex (either from the tracking detector, the *C5* run average or nominal vertex) to determine E_t and R_t. It also determines the distance of a muon trajectory from the vertex as one of the candidate parameters.

6.4 Muon Bremsstrahlung

6.4.1 Muon Bremsstrahlung Shower in *UCAL*

A high momentum muon can produce a bremsstrahlung shower in the *UCAL*. If the shower is not localized to the cell it occurred in but hits more cells it can pose a problem to the muon finder because the fitted trajectory does not pass through all cells. In figure 6.6 such a case is illustrated. MUFFIN identifies such a case by requiring that the energy in the shower center cell is bigger than 5 GeV and all the energy in all neighboring cells which are not hit by the fitted trajectory (cells "1", "2" and "3") is less than 10 % of the energy in the shower center.

6.4.2 Muon Bremsstrahlung Shower in a *UCAL* Wave Length Shifter

A muon can produce a bremsstrahlung shower in or near the wave length shifter (*WLS*). Such a shower will not be localized to the cell it occurred in but also cause the photomultipliers of neighboring cells to record energy.

Figure 6.7 illustrates this for two neighboring modules. Since the cells are neighboring and since MUFFIN is largely based on condensates these cells (the *EMC* cells in figure 6.7) which have not been traversed by the muon are part of the candidate. When MUFFIN tries to perform the trajectory fit these cells will reduce the hit ratio of the candidate and thus reduce the efficiency of the finder for such events.

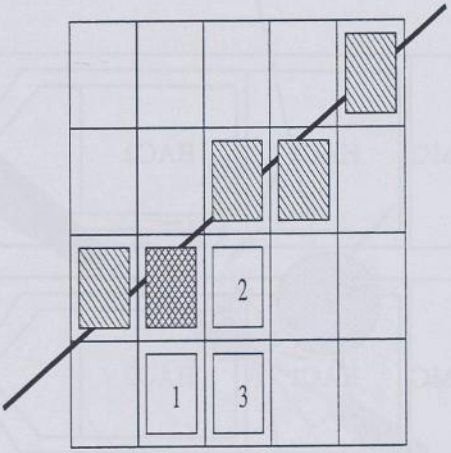

Figure 6.6: Schematic view of a muon traversing *UCAL* cells which caused a bremsstrahlung shower. The cross hatched cell is the shower center, cells "1" through "3" are part of the shower.

One possibility to deal with this problem would be to perform a cut on the imbalance in a cell. This however would compromise the muon finder efficiency for muons which only traverse a few cells.

Instead MUFFIN uses CONDENSOR to find all cells which could have energy just because there was a shower that leaked into their *WLS*:

CONDENSOR first tries to identify the cell that contains the center of the shower. Such a cell has to have imbalance bigger than 0.1 and more than 5.0 GeV energy. The imbalance of the cell points to the side where the shower occurred. Due to the geometric structure of the *UCAL* only cells in front of the cell that contained the shower can be potential candidates for cells with energy due to a shower. Also cells in neighboring towers can be candidates, so MUFFIN scans the next 2 towers.

For this *WLS* shower topology CONDENSOR requires at least one cell on the other side of the *WLS*-gap to have a large imbalance of 0.5. Only then will it use a lower imbalance cut of 0.3 to find the other cells. Moreover CONDENSOR requires that for all candidate cells the channel that is not on the *WLS*-side recorded energy below the noise cut value. This value is the per-cell noise cut value (see section 6.3.1) divided by $\sqrt{2}$.

6.4.3 Muon Bremsstrahlung Showers leaking into the *CTD*

Events where the muon bremsstrahlung occurs just before the muon traverses the *CTD* or inside the *CTD* volume usually cause many tracks to be seen in the *CTD*. Moreover, because of the solenoidal field in *ZEUS*, particles will be bent away from their initial trajectory and cause a wide area of cells to be hit near the region where the muon leaves the inner volume. Figure 6.8 shows such an event. MUFFIN tries to identify the cells which have been hit by such particles by using the trajectory of the muon and the direction of the magnetic field to calculate the plane in which the particles' trajectories are located. MUFFIN allows the vector pointing from the cell

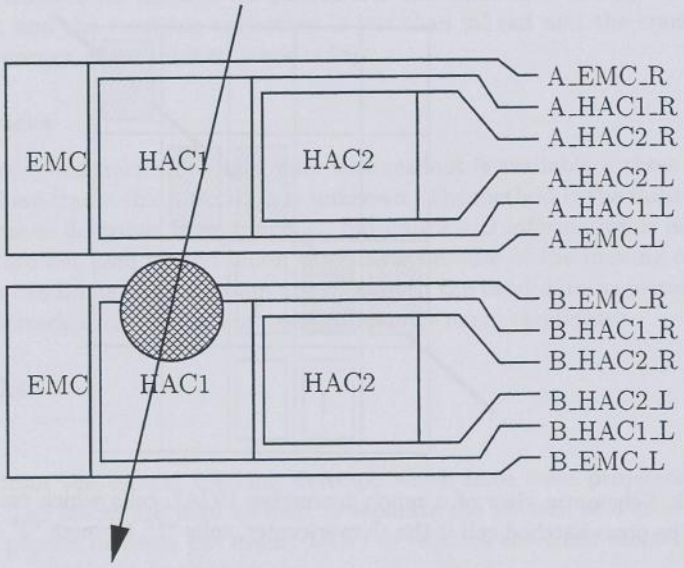

Figure 6.7: Schematic view of two modules (A top, B bottom) and the *WLS* and different channels. If a muon showered in the location given by the hatched circle the *EMC* and *HAC*1 channels near the gap record energy (A_EMC_L, A_HAC1_L, B_EMC_R, B_HAC1_R) while the other channels do not record energy.

to the muon trajectory to deviate 15 ° from the normal to the magnetic field.

6.5 Program Initialization

During the initialization phase of MUFFIN some lookup tables are zeroed and all steering cards are processed. It is possible to create a template of the steering cards file with the current settings, as well as a LaTeX [38] file which contains the steering cards in the default setting and which can be included in a document.

Most of the remaining initialization work is performed when the first event is read because MUFFIN needs to know the event date to select geometry and calibration data valid for that data taking period:

- read all geometry information
- calculate the calorimeter cell geometry
- read the neighborship relation lookup table
- calculate parameters for fast ray tracing through the calorimeter

Normally all this initialization is only performed a single time, but if MUFFIN is used on data stemming from periods with different geometry setup, MUFFIN can be instructed to redo the initialization for every run.

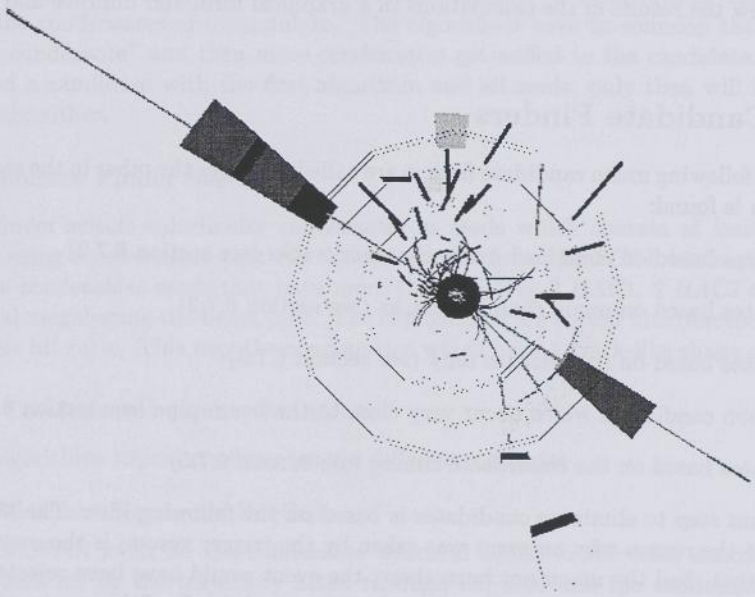

Figure 6.8: Example of a cosmic muon traversing the *ZEUS* detector. The view shows the event seen from the *FCAL*, the beam pipe being in the center. This muon has had a bremsstrahlung near the beam pipe and charged particles have been bent by the magnetic field and hit the *BCAL-EMC*. The muon trajectory is known to high precision because two opposing muon chamber tracks were found.

MUFFIN can perform additional tasks:

- calculate the neighborship relation lookup table.
- create CAR files with the neighborship relation lookup table.
- create a VRML file [39] with the neighborship relation lookup table for every cell type (so not for every cell, but for every neighborship type one file).
- check various geometric algorithms inside the CONDENSOR code.
- check for overlapping cell volumes (which would be a serious mistake in the geometry).
- create a template steering cards file with the current settings.

6.6 VRML File Output

MUFFIN can output the event data as VRML-1.0 files. VRML, "Virtual Reality Modeling Language" [39] is a file format which can be used to describe $3-D$ scenes which can then be looked

at with a VRML-browser. Such browsers are available as so called "plug-in" software for many popular WWW HTML browsers. MUFFIN can also add the candidate information to the data, thus allowing to view the results of the calculations in a graphical form and improve and debug the algorithms.

6.7 Muon Candidate Finders

For every event the following muon candidate finders are called one after the other in the sequence below until a muon is found:

1. Find candidates based on combined muon chamber tracks (see section 6.7.2)
2. Find candidates based on muon chamber tracks (see section 6.7.2)
3. Find candidates based on condensates only (see section 6.7.3)
4. Find halo muon candidates which occur very close to the beam pipe (see section 6.7.4)
5. Find candidates based on the condensate timing (see section 6.7.5)

A very important step to eliminate candidates is based on the following idea: The MUFFIN finder assumes that the reason why an event was taken by the trigger system is the overlapped muon. It assumes that, had the muon not been there, the event would have been rejected.

In the case of the CC sample the traversing muon has increased the $\not{P}_t$ of the event and so the event was triggered. This is an important property for a muon candidate and it is used to reduce the sample of possible candidates significantly: Giving a trigger condition such as $\not{P}_t > X$ GeV MUFFIN temporarily removes all candidate cells and tests the condition. If the condition is not fulfilled anymore it means that the candidate might be a traversing muon. Should the condition still be fulfilled it means that the candidate is just a random combination of cells which happened to look like a traversing muon. This check is done at an early stage of the calculation in order to avoid unnecessary calculations.

6.7.1 Muon Energy Deposit Connected to *FCAL* Beampipe Energy Deposit

For most physics events and beam gas collisions particles hit the *FCAL* beam pipe region. The cells in this region usually form a single large condensate. If the traversing muon hits this condensate MUFFIN is unable to identify the muon because there are too many cells in the condensate which are not hit by the muon.

MUFFIN finds the muon in such events by removing successively rings of cells around the *FCAL* beam pipe hole and rerunning all of its algorithms.

6.7.2 Muon Track Based Finder

Both the finder that is based on combined muon tracks as well as the finder based on single muon tracks work in the same way: A muon candidate consists of all calorimeter condensates which are hit by the muon track. If a candidate is found all candidate parameters are calculated at highest precision. For the finder based on combined muon tracks the trajectory fit is not redone because the muon chamber tracks are the best estimate for the trajectory. For the finder based on single muon tracks the offset vector is not refitted but only the direction of the trajectory.

6.7.3 Condensate Based Finder

This finder is based on calorimeter condensates only. It uses several different algorithms to find the condensates of a candidate. The algorithms have in common that they begin with a "seed condensate" and then more condensates get added to the candidate. MUFFIN first tries to find a candidate with the first algorithm and all seeds, only then will it continue with the next algorithm.

Condensate Finder Seed

The finder selects calorimeter condensates as seeds which contain at least 2 cells.It will also avoid using a condensate that has too many cells from the *FCAL* beam pipe region: MUFFIN rejects condensates seeds that have more than 7 *EMC*, 2 *HAC*1, 2 *HAC*2 or more than 4 cells in total neighboring the beam pipe. The condensates are sorted into descending order according to their hit ratio. This way the condensates which have a track-like shape come first.

Add Condensates to the Candidate

The algorithms to add condensates use different methods:

1. Maximize Number of Hit Cells

   MUFFIN looks for the condensate which, if added to the seed, maximizes the number of cells hit by the trajectory fitted through the seed and the condensate. It then declares both condensates as the new seed and looks for the next condensate which maximizes the number of hit cells. MUFFIN only allows candidates for which the fitted trajectory hits all condensates.

2. Maximize Number of Hit Cells Blown Up

   This algorithm is just like the algorithm described above but the cell volumes are artificially increased by projecting the corners along the line connecting them with the cell center by a constant value. This improves the finders efficiency because during the candidate search only the quick linear regression line fit can be used which is not accurate enough.

3. Maximize Occupancy

   This algorithm is just like the one described above only that instead of adding the condensate which maximizes the number of cells hit this algorithm adds the condensate which maximizes the occupancy, i.e. the ratio of the number of cells of this candidate hit by the fitted trajectory over the number of cells of the calorimeter hit by the trajectory.

4. Add Condensates with Minimum Hit Ratio

   In this algorithm a condensate is added to a candidate if the hit ratio of the sum of condensate and candidate is bigger than 0.5. The hit ratio is the ratio between the number of cells of a candidate hit by the fitted trajectory over the total number of cells in the candidate.

Candidate Veto

Before the candidate is evaluated further it has to pass a number of veto conditions to prevent excessive, unnecessary calculations:

1. Candidate already calculated

   The muon finder algorithm is made such that it is unavoidable that certain combinations of condensates are found several times. In this case a new candidate is vetoed to avoid duplication.

2. Candidate has too many cells

   The muon finder rejects candidates with too many cells in order to avoid unnecessary calculations.

3. Candidate hit ratio is too low

   Candidates with hit ratio less than 0.6 are rejected. The hit ratio is a measure for the shape of the candidate, a bad hit ratio suggests that it does not stem from a traversing particle.

4. Candidate occupancy is too low

   Candidates with occupancy less than 0.15 (occupancy is the ratio of number of candidate cells hit by the trajectory over the total number of calorimeter cells hit by the trajectory) are rejected. This cut is not executed for candidates which have a long and narrow shape or which are parallel to the beam axis but far away from it and for which the velocity is near the speed of light.

5. Not all condensates hit by trajectory

   Candidates for which not all condensates are hit by the fitted trajectory are rejected if the distance of the condensates which are not hit to the trajectory is smaller than 100 cm.

6. Event without candidate still passes trigger

   MUFFIN tests whether the event, if the candidate cells were removed, would still pass the trigger condition. For a charged current event sample it would test whether the P_T of the event is below the trigger cut of 9 GeV after the cells are removed. The candidate is rejected if the event still passes the trigger.

   This test is not performed if MUFFIN has found the event likely to be a multiple muon shower: MUFFIN calls an event a muon shower candidate if one or more of the following conditions is true:

   - There are parallel trajectories fitted to long and narrow condensates.
   - There are parallel muon chamber tracks.
   - There are more than 6 parallel two dimensional muon chamber tracks.

A candidate that fails any of the veto conditions is removed and will not appear on the output. (the NTUPLE).

Precise Calculation of Candidate Parameters

MUFFIN calculates the precise candidate parameters, the trajectory is fitted with a minimization fit (see section 6.8.4). If after this fit the trajectory hits another, not yet added condensate this condensate gets added to the candidate and all parameters are recalculated. Should the fitted trajectory not hit all of the condensates, the condensates which are not hit are removed and all parameters are recalculated.

Candidate Classification

MUFFIN calls a user-supplied routine to classify candidates. In this routine the candidates are compared to a set of parameters and it is determined if they indeed stem from a traversing muon. Should the classification be positive the candidate is removed from the event and processing ends. If the candidate is not positively identified it will be stored in the output for further study, but processing continues. Table 6.2 lists the muon classification cuts together with a description of the type of muon candidate found by the cut.

6.7.4 Beampipe Halomuon Finder

This muon finder is specialized on halo muons which are close to the beam pipe and hit both *FCAL* and *RCAL*. In principle the condensate based muon finder should find these halo muons too but for some cases the vetoing of candidates removes a beam pipe halo muon candidate.

This finder simply searches pairs of condensates, one in the *FCAL* ($Z > 200.0cm.AND.\rho < 100.0cm$) and one in the *RCAL* ($Z < -100.0cm.AND.\rho < 100.0cm$).

In this finder a candidate is vetoed if the event, when the candidate is removed, still passes the trigger conditions.

For each such pair MUFFIN calculates the candidate parameters precisely and then calls the user-supplied classification routine (see section 6.7.3) to positively identify the candidate.

6.7.5 Condensate Timing Based Finder

This muon finder looks for pairs of condensates which are far away from each other (distance of the condensate centers of more than 100 cm). It then calculates the velocity at which a particle would need to travel between the two condensates from the average condensate times. Then the candidate parameters are determined. If additional condensates are hit by the fitted trajectory they are added and the parameters are recalculated.

Candidates are vetoed if one of the following conditions is true:

1. The event would still pass the trigger if the candidate cells were removed.

2. The candidate contains a positron candidate (see section 6.7.6).

After calculating the muon candidate parameters at highest precision the user-supplied classification routine (see section 6.7.3) is called to positively identify the candidate.

6.7.6 Final State Positron vs. a Shower in *EMC*

Kernbremsstrahlung of a muon in the *EMC* section produces a high energy gamma which showers in the *EMC*. This can result in a shower very similar to that of a final state positron of a genuine positron-proton collision event.

In order to avoid misidentification MUFFIN tries to find a final state positron prior to execution if the $E - P_z$ value of the event is compatible with an NC event: If $E_{tot} - P_z > 35\,\text{GeV}$ and $E_{tot} - P_z < 70\,\text{GeV}$ then MUFFIN runs the `SINISTRA` positron finder [40]. If a positron has been found by that finder and if there is a condensate that contains nothing but those cells then this condensate is tagged. Should a muon candidate be found that contains this condensate the candidate will be tagged too, this tag can then be used in the muon classification (see section 6.7.3) to reject the candidate.

6.8 Trajectory Fits

MUFFIN returns information about the muon trajectory. It assumes this trajectory to be a straight line.

During candidate search a quick 3D line fit is necessary while for a final classification (see section 6.7.3) of a candidate a more precise fit is necessary.

6.8.1 Linear Regression Fit

Two consecutive linear regression fits to the coordinates of the cell centers are used to get a 3D line that follows the trajectory of the candidate.

First the coordinates are sorted according to the size of the candidate in the coordinate direction. The coordinate corresponding to the maximum size is used as the ordinate for the first fit, the second biggest is used as the abscissa. For the second fit the ordinate is the projection of the cell onto the line obtained with the first fit. The abscissa is the third unused variable.

The fit algorithms take care of special cases where a candidate has no size in one or two coordinate directions.

The fits are performed eight times with all possible combinations of the following algorithms:

1. Energy weighted: $w_x = w_y = w_z = E_{\text{cell}}$
2. Cell size weighted: $w_x = w_x/\text{size}_x; w_y = w_y/\text{size}_y; w_z = w_z/\text{size}_z;$
3. Correction of the cell position based on the cell imbalance: $\vec{c_{\text{new}}} = \vec{c_{\text{old}}} + \vec{WLS} * Imbalance$ where $\vec{WLS}$ is the direction perpendicular to the WLS corresponding to positive cell energy imbalance.

Of those fitted lines the one with the best *HitRatio* is selected. To allow for problems with the fit accuracy the hit ratio is calculated using the blown up cell geometry.

6.8.2 Minimisation Fit

The straight line fits described above have a couple of disadvantages:

- There are candidate cell configurations which can hardly be fitted properly. This might decrease the *Occupancy* and thus make the identification more difficult.
- The treatement of cells that are close to a bremsstrahlung shower is not clear. A possibility would be to omit them for the fit, but then cases with only few cells hit become very difficult to detect. If those cells were always taken into account the linefit would sometimes produce incorrect results.

A more complex fit using MINUIT is used to make a precise fit of the muon trajectory.

If the entire calorimeter readout information was available offline one could calculate the probability for a muon to deposit a certain amount of energy in a cell. This could be used to define a function MINUIT has to minimize.

The data available to MUFFIN only contain zero-suppressed calorimeter information (see section 6.3.1). Also here bremsstrahlung showers pose a problem because the cell energy can be very high and consequently the probability for a muon to have caused such a signal very low.

The following function is minimised by modifying the trajectory parameters (offset and direction).

$$F_{\mathsf{MINUIT}} = 5918 - \sum_{\mathrm{cell}_{\overline{\mathrm{sig}}}} P_{\overline{\mathrm{sig}}} - \sum_{\mathrm{cell}_{\mathrm{sig}}} P_{\mathrm{sig}} \tag{6.1}$$

5918 is the number of cells in the *UCAL*. P_{sig} is the probability for a cell to have a signal for a given trajectory. $P_{\overline{\mathrm{sig}}}$ is the probability for a cell not to have a signal for a given trajectory. These probabilities are calculated using the estimated energy loss of a muon in the *UCAL* material and the energy cut value of each cell (see also section 6.8.4 for a detailed description).

By splitting up the sums into sums of cells hit and not hit by the fitted trajectory one can write:

$$F_{\mathsf{MINUIT}} = 5918 - \sum_{\mathrm{cell}^{\overline{\mathrm{hit}}}_{\overline{\mathrm{sig}}}} P_{\overline{\mathrm{sig}}} - \sum_{\mathrm{cell}^{\mathrm{hit}}_{\overline{\mathrm{sig}}}} P_{\overline{\mathrm{sig}}} - \sum_{\mathrm{cell}^{\mathrm{hit}}_{\mathrm{sig}}} P_{\mathrm{sig}} - \sum_{\mathrm{cell}^{\overline{\mathrm{hit}}}_{\mathrm{sig}}} P_{\mathrm{sig}} \tag{6.2}$$

The first sum is the number of cells that have not been hit, for those cells the probability for no signal $P_{\overline{\mathrm{sig}}} = 1.0$ and the sum is simply the number of cells which have no signal and have not been hit: $N^{\overline{\mathrm{sig}}}_{\overline{\mathrm{hit}}}$

The fourth sum contains the cells which have not been hit, for those cells the probability for a signal $P_{\mathrm{sig}} = 0.0$ so the term disappears.

So we have

$$F_{\mathsf{MINUIT}} = 5918 - N^{\overline{\mathrm{sig}}}_{\overline{\mathrm{hit}}} - \sum_{\mathrm{cell}^{\mathrm{hit}}_{\overline{\mathrm{sig}}}} P_{\overline{\mathrm{sig}}} - \sum_{\mathrm{cell}^{\mathrm{hit}}_{\mathrm{sig}}} P_{\mathrm{sig}} \tag{6.3}$$

This can be simplified by writing:

$$\begin{aligned} 5918 - N^{\overline{\mathrm{sig}}}_{\overline{\mathrm{hit}}} &= \underbrace{N^{\mathrm{sig}}_{\mathrm{hit}} + N^{\overline{\mathrm{sig}}}_{\mathrm{hit}}} + N^{\mathrm{sig}}_{\overline{\mathrm{hit}}} + \underbrace{N^{\overline{\mathrm{sig}}}_{\overline{\mathrm{hit}}} - N^{\overline{\mathrm{sig}}}_{\overline{\mathrm{hit}}}} \\ &= N^{\mathrm{hit}}_{\mathrm{tot}} + N^{\mathrm{sig}}_{\overline{\mathrm{hit}}} + 0 \end{aligned}$$

And so the function to be minimized is:

$$F_{\mathsf{MINUIT}} = N^{\mathrm{hit}}_{\mathrm{tot}} + N^{\mathrm{sig}}_{\overline{\mathrm{hit}}} - \sum_{\mathrm{cell}^{\mathrm{hit}}_{\overline{\mathrm{sig}}}} P_{\overline{\mathrm{sig}}} - \sum_{\mathrm{cell}^{\mathrm{hit}}_{\mathrm{sig}}} P_{\mathrm{sig}} \tag{6.4}$$

The individual terms are:

$N^{\mathrm{hit}}_{\mathrm{tot}}$	The total number of cells hit by the fitted trajectory.
$N^{\mathrm{sig}}_{\overline{\mathrm{hit}}}$	The number of cells of the candidate which have a signal but are not hit by the fitted trajectory.
$\sum_{\mathrm{cell}^{\mathrm{hit}}_{\overline{\mathrm{sig}}}} P_{\overline{\mathrm{sig}}}$	The sum of the probabilities for recording no signal for the cells which have no signal but are hit by the fitted trajectory.
$\sum_{\mathrm{cell}^{\mathrm{hit}}_{\mathrm{sig}}} P_{\mathrm{sig}}$	The sum of the probabilities for recording a signal for the cells which have a signal and are hit by the fitted trajectory.

The minimization function in (6.4) expresses the following ideas:

- It does not really matter if a muon hits a cell and does not cause a signal as long as it only traverses a small volume of that cell: In that case the total number of cells hit increases by 1.0 but at the same time the probability for **not** causing a signal in that cell is also close to 1.0.

- If a muon hits a cell with a signal it would be good to traverse so much volume that it is possible for the muon to cause a signal in the cell.

MINUIT modifies the line parameters direction and offset such that F_{MINUIT} becomes minimal.

If a candidate cell (per definition with signal) is not hit by the trajectory F_{MINUIT} increases by 1.0. There is however a reason why a cell might belong to a muon candidate but still not have been traversed by the muon: The reason for this is muon bremsstrahlung showers. Here a cell can have energy without being traversed by the muon. MINUIT will try to put the candidate trajectory through these cells too. Sometimes though this is geometrically impossible. MUFFIN tries to identify cells that have possibly only energy because there was a bremsstrahlung shower. It uses the algorithm described in section 6.4.1 and 6.4.2 to tag all cells that might have energy only because there was a bremsstrahlung shower. If such a cell is not hit by the trajectory fit to the cells F_{MINUIT} is not increased by 1.0.

To get the start value for the track parameters MUFFIN chooses one of the following trajectory estimates depending on which estimate gives the best *HitRatio*:

- A muon chamber track.

- An inner track.

- The result of the linear regression line fit.

6.8.3 Candidate Velocity Fit

The calorimeter is capable of a very precise measurement of the time of the energy deposit with a resolution in the nanosecond range. Since the dimensions of the calorimeter are in orders of meters it is possible to use the time information to calculate the velocity of the traversing muon.

The candidate velocity is then calculated through a weighted linear regression fit using the position of each cell along the fitted line and the cell time. The cell time is in addition corrected for the distance of the cell center from the line. The weight is calculated using the prescription explained in [18].

Even though the velocity of a candidate seems like a good identification tool it should only be used with care: An event with a prompt muon and opposing it some very low energy deposit might result in a muon candidate with a velocity close to the speed of light because the low energy deposit might not contribute enough to the linear regression line fit.

Figure 6.9 shows a histogram of the velocity for all positively identified muon candidates, the histogram is restricted to ($v < 100\,\text{cm/ns}$) but only 19 of the 648 candidates have a velocity outside the shown region. The mean value of the distribution is at $34.2\,\text{cm/ns}$ which is very close to the speed of light indicating that indeed the observed signal stems from highly energetic particles traversing the detector.

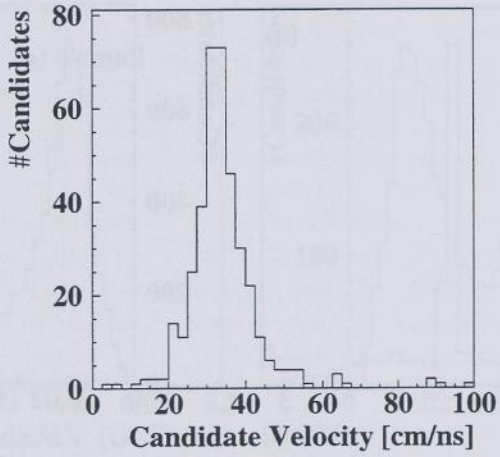

Figure 6.9: The distribution of the absolute value of the velocity for the muon candidates found in the CC event sample. The mean value of the distribution is at 34.2 cm/ns which is very close to the speed of light indicating that indeed the observed signal stems from highly energetic particles traversing the detector.

6.8.4 The Probability for a Muon Signal in a Cell

The calorimeter segmentation into cells has been chosen such that a MIP particle like a muon deposits enough energy to be above noise cuts. This is true for muons that traverse the entire volume of a cell almost perpendicularly to the uranium plates of the cell, like prompt muons.

A muon that traverses only a part of the cell might not deposit enough energy and so the signal might be suppressed by the noise cuts.

The energy loss of a muon in the calorimeter follows a Landau distribution. This has been shown in many measurements of the calorimeter prototype modules as well as with halo muons in *HERA*.

In most of those tests though the muon traversed the calorimeter perpendicularly to the uranium plates.

It is possible to show this distribution also for muons traversing the detector at different angles. In figure 6.10 the opening angle between the muon trajectory and the direction perpendicular to the uranium plates (the sampling direction) is shown. This histogram contains data from muon candidates found in the charged current event sample.

Clearly three peaks can be identified. At 0, $\pi/2$ and π. They correspond to cells coming from halo muon events. For those events the cells in *BCAL* are penetrated from the side while for *FCAL* and *RCAL* the muon hits the cells in sampling direction.

In figure 6.10 the energy deposited in a cell is divided by the length of the muon trajectory through active material. Clearly two peaks can be identified. A cut on the angle under which the cell is traversed shows the reason for those two peaks. In figure 6.11 only cells with the muon hitting the cells almost perpendicularly is shown. The secondary peak has completely

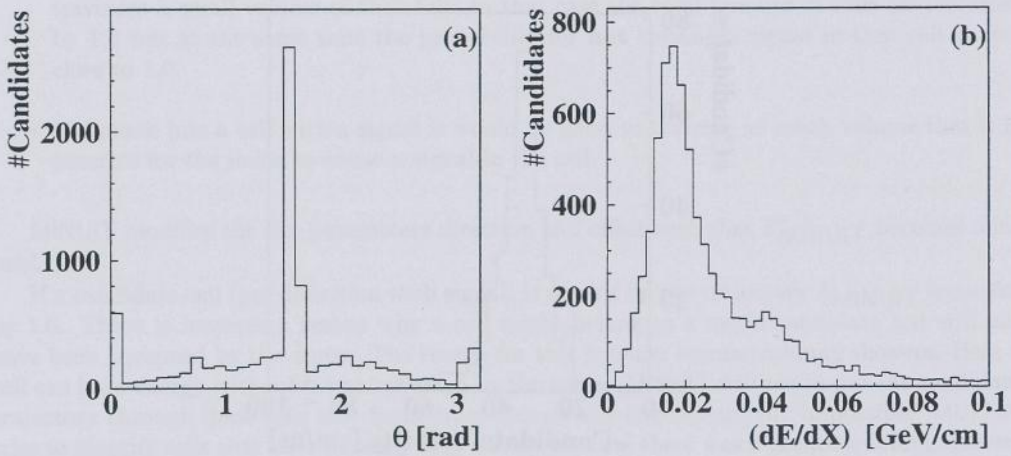

Figure 6.10: For all cells of muon candidates found in the CC event sample, histogram (a) shows the angle between the muon direction and the sampling direction θ and histogram (b) shows the energy loss dE/dX for these cells, two peaks are visible.

disappeared. In figure 6.11 only cells where the muon traverses from the side is shown. Here the secondary peak is very much enhanced.

The second peak stems from muons that only traverse scintillator material. The energy loss is smaller but more light is produced.

In figure 6.12 (a) cells with angles $0.1 < \theta < 1.56$ or $1.58 < \theta < 3.04$ are selected. In the same figure a Landau distribution is shown that has been fitted to the experimental data:

To fit a Landau distribution the following formula is used with a and b as free parameters:

$$L(dE/dX, a, b) = e^{-0.5(a(x-b)+e^{(-a(x-b))})} \tag{6.5}$$

The following parameterization results:

$$a = 270.0\ cm/GeV \tag{6.6}$$

$$b = 0.15\ GeV/cm \tag{6.7}$$

This parameterization is used for the calculation of the probability to cause a signal. The reason is that MUFFIN has no problem detecting halo muons, muons in general if they run along a module. That is a very clear pattern. More difficult are muons that traverse the detector at other angles. And for those muons the ideal parameterization for the Landau distribution has to be found.

From the dE/dX distribution it is possible to calculate the probability for a muon to deposit so much energy in a cell that the measured cell energy is bigger than the noise cut. For a known length l of the muon trajectory in the cell and a cell cut E_{cut} the probability is simply the integral of the Landau distribution from E_{cut}/l to infinity:

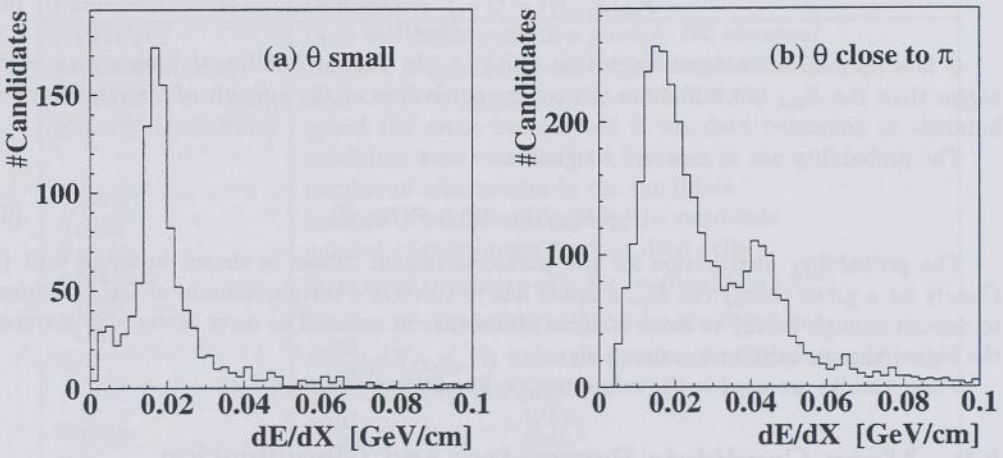

Figure 6.11: For all cells of muon candidates found in the charged current event sample, histogram (a) shows dE/dX for cells with θ small: ($\theta < 0.1$ or $\theta > 3.04$). The peak at higher dE/dX from figure 6.10 (b) has disappeared. Histogram (b) shows dE/dX for cells with θ close to $\frac{\pi}{2}$: ($|\theta - 1.57| < 0.1$). The peak at higher dE/dX from figure 6.10 (b) is more pronounced.

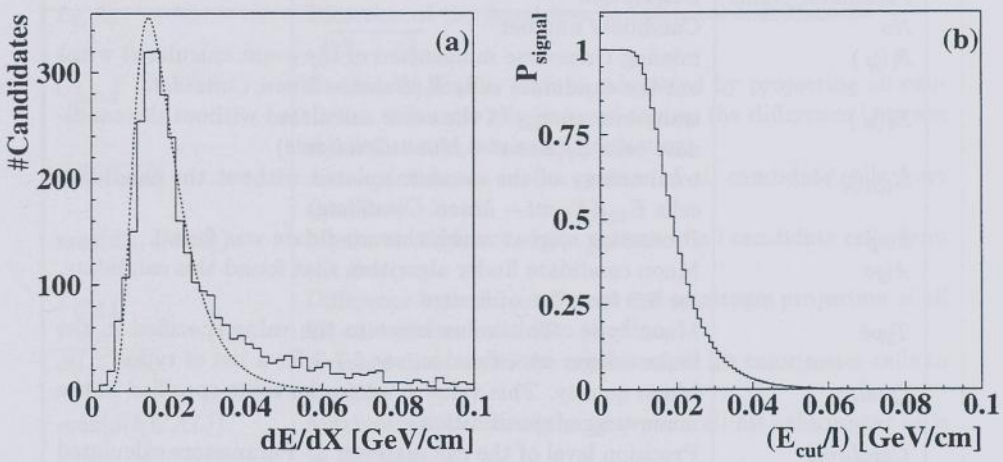

Figure 6.12: dE/dX for all cells of muon candidates found in the CC event sample for angles $0.1 < \theta < 1.56$ and $1.58 < \theta < 3.04$ together with the Landau distribution that has been fitted to the data (a), and the integral of the Landau distribution (b) which gives the probability for a signal in a cell with an energy cut E_{cut} if the muon traverses l material.

$$P_{\text{sig}}(E_{\text{cut}}/l) = C * \int_{E_{\text{cut}}/l}^{\infty} L(\rho)d\rho \tag{6.8}$$

C is a normalization factor such that $P(0.) = 1.0$: The probability to measure an energy bigger than the E_{cut} is 1.0 if either the energy cut is zero or the amount of material traversed infinite.

The probability not to measure a signal is:

$$P_{\overline{\text{sig}}}(E_{\text{cut}}/l) = 1.0 - P(E_{\text{cut}}/l) \tag{6.9}$$

The probability distribution for the parameterization chosen is shown in figure 6.12 (b): Clearly for a given energy cut E_{cut} a muon has to traverse a certain amount of *UCAL* material to deposit enough energy to cause a signal above the cut value. The more material is traversed, the higher the probability to cause a signal.

These results are used in the minimization line fit (see section 6.8.2).

6.9 Muon Candidate Parameters and Classification

Table 6.1 shows the parameters that are calculated for every muon candidate. These parameters are used by the candidate classification routine (see section 6.7.3). Some of the parameters are calculated when only a linear regression line fit (see section 6.8.1) is available some require that the MINUIT based minimization fit has been done (see section 6.8.2). Table 6.2 gives a list of the muon classification cuts used in the presented analysis. In total 90 different combinations of cuts are used.

Parameter Name	Description
No	Candidate number
$\not{E}_t(\not{\mu})$	missing transverse momentum of the event calculated without the candidate cells $\not{E}_t(Event - Muon\ Candidate)$
$E_t(\not{\mu})$	transverse energy of the event calculated without the candidate cells $E_t(Event - Muon\ Candidate)$
$E_{tot}(\not{\mu})$	total energy of the event calculated without the candidate cells $E_{tot}(Event - Muon\ Candidate)$
Step	Processing step at which this candidate was found.
Algo	Muon candidate finder algorithm that found this candidate, see 6.7 for a list of finders.
Type	Muon type. This value is set to the value specified in the muon trigger specification, see 6.7.3 for a list of types.
Quality	Muon quality. This value is set to the value specified in the muon trigger specification.
CalcLevel	Precision level of the calculations: 1: Parameters calculated based on linear regression linefit. 2: Parameters calculated based on a MINUIT minimisation linefit.

continued on next page

continued from previous page

Parameter Name	Description
$NCElCand$	Does this muon contain a possible NC electron?
$LineHitsAllCond$	does the fitted line hit all the condensates?
$LineHitsOtherCond$	does the fitted line hit other condensates?
$EventWouldBeKilled$	would the event be removed if the data belonging to the candidate were removed?
N_{Cond}	number of condensates in the candidate
N_{Cells}	number of calorimeter cells in the candidate
N_{Holes}	number of calorimeter readout dead cells
N^{Hit}_{Cells}	number of candidate cells hit by fitted line ($N^{\text{hit}}_{\text{tot}}$).
N^{Hit}_{CAL}	number of calorimeter cells hit by the fitted line.
$\mathcal{R}$	$N^{Hit}_{Cells}/N_{Cells}$. A hit ratio of 1.0 means that all candidate cells are hit by the line.
$\mathcal{R}_{WLS}$	$N^{Hit}_{Cells}/(N_{Cells} - N^{WLS}_{Cells})$.
$\mathcal{R}_{S}$	$N^{Hit}_{Cells}/(N_{Cells} - N^{Shower}_{Cells})$.
$\mathcal{R}_{NB}$	$N^{Hit}_{Cells}/(N_{Cells} - N^{NB}_{Cells})$.
$\mathcal{R}_{\bar{B}}$	$N^{Hit}_{Cells}/(N_{Cells} - N^{\bar{B}}_{Cells})$.
$\mathcal{R}_{\bar{B}S}$	$N^{Hit}_{Cells}/(N_{Cells} - N^{\bar{B}}_{Cells} - N^{Shower}_{Cells})$.
$\mathcal{O}$	Occupancy $N^{Hit}_{Cells}/N^{Hit}_{CAL}$. An occupancy of 1.0 means that the candidate contains all calorimeter cells which have been hit by the line.
L_X, L_Y, L_Z	Fitted line offset vector. It is in the centre of the candidate.
L_θ, L_ϕ	Direction of the fitted line, in spherical coordinates.
L_ρ	$\sqrt{L_X^2 + L_Y^2}$
l_{Cand}	Candidate length. This is calculated by projecting all candidate cells onto the line and taking the difference between maximum and minimum projection.
$\overline{d(l, Cand)}$	Average distance of the centers of all candidate cells from the line.
$max(d(l, Cand))$	Maximum distance of the centers of all candidate cells from the line.
L_{CAL}	Difference between maximum and minimum projection of all hit calorimeter cells onto the line.
$\overline{d(l, CAL)}$	Average distance of the centers of all hit calorimeter cells to the line.
$max(d(l, CAL))$	Maximum distance of the centers of all hit calorimeter cells to the line.
$d(l, BP)$	Distance of the line to the beam line.
$d(l, Vtx)$	Distance of the line to the event vertex.
$l(l, InnerDet)$	Length of the trajectory through the inner detector volume which is approximated as a cylinder of 120 cm radius from $z = -140$ cm to $z = 210$ cm.

continued on next page

continued from previous page

Parameter Name	Description
$STSlop$	Slope of "candidate velocity fit", should be close to $1/c$ for a traversing muon.
V_{fit}	$(1/STSlop)$ except for candidate finder based on condensate timing (6.7.5), here it conains the velocity based on the average time of the two condensates and their distance.
N_{Cells}^{Shower}	Number of candidate cells that are not hit but that are part of a bremsstrahlung shower (see 6.4.1).
N_{Cells}^{WLS}	Number of candidate cells that are not hit but that have one of the WLS hit by a bremsstrahlung shower (see 6.4.2).
$N_{Cells}^{\vec{B}}$	Number of candidate cells that are not hit but might have been hit by particles from a bremsstrahlung shower that were bent away from the muon trajectory by the magnetic field (see 6.4.3).
N_{Cells}^{NB}	Number of cells that are not hit but have at least one neighbor cell hit by the line.
N_{MuTrk}^{max}	Maximum number of candidate cells hit by any muon track.
$N_{MuTrk}^{max\text{-}1}$	second biggest number of candidate cells hit by any muon track.
$\mathcal{R}_{MuTrk}^{max}$	hit ratio for the best muon track
$\mathcal{R}_{MuTrk}^{max\text{-}1}$	hit ratio for the second best muon track
$\Delta\alpha_{MuTrk}^{max}$	maximum angular difference between the direction of the fitted line and any muon track that hits any candidate cell.
$\Delta\alpha_{MuTrk}^{min}$	minimum angular difference between the direction of the fitted line and any muon track that hits any candidate cell.
Δd_{MuTrk}^{max}	minimum distance of the fitted line to any muon track
$\Delta d_{MuTrk}^{max\text{-}1}$	second smallest distance of the fitted line to any muon track.
Δd_{MuWire}^{min}	minimum distance of the fitted line to any muon wire track, this value is calculated in the $2-D$ coordinate system which is given by the wire track orientation.
$\Delta\alpha_{MuWire}^{min}$	minimum angular difference between the fitted line and any muon wire track.
$\Delta d_{MuStrip}^{min}$	minimum distance of the fitted line to any muon strip track, this value is calculated in the $2-D$ coordinate system which is given by the strip track orientation.
$\Delta\alpha_{MuStrip}^{min}$	minimum angular difference between the fitted line and any muon strip track.
N_{InTrk}^{max}	maximum number of cells hit by any inner track. The track is used as an arrow pointing from the inside of the detector to the outside.
$N_{InTrk}^{max\text{-}1}$	second biggest number of cells hit by any inner track, the track has to point in the opposite direction to the one that hit the maximum number of cells

continued on next page

continued from previous page	
Parameter Name	Description
$\mathcal{R}_{InTrk}^{max}$	hit ratio for the best inner track
$\mathcal{R}_{InTrk}^{max\text{-}1}$	hit ratio for the second best inner track
$\Delta\alpha_{InTrk}^{max}$	maximum angular difference between the direction of the fitted line and any inner track that hits any candidate cell

Table 6.1: List of the parameters calculated by MUFFIN for all muon candidates. The parameters are used by the muon identification algorithm to select muon candidates.

Type	Description, Cuts
Muon types found using muon chamber tracks:	
Muon with good occupancy and hit ratio	
1	$P_t(\mu) < 9 \wedge \mathcal{O} > 0.9 \wedge \mathcal{R} > 0.9$
2	$P_t(\mu) < 9 \wedge \mathcal{O} > 0.9 \wedge \mathcal{R}_{WLS} > 0.9$
3	$P_t(\mu) < 9 \wedge \mathcal{O} > 0.9 \wedge \mathcal{R}_{S} > 0.9$
4	$P_t(\mu) < 9 \wedge \mathcal{O} > 0.9 \wedge \mathcal{R}_{\bar{B}} > 0.9$
5	$P_t(\mu) < 9 \wedge \mathcal{O} > 0.9 \wedge \mathcal{R}_{\bar{B}S} > 0.9$
Muon candidate that traverses all of *UCAL*	
11	$P_t(\mu) < 9 \wedge \mathcal{O} > 0.9 \wedge \mathcal{R} > 0.7 \wedge (l_{Cand} - L_{CAL}) > -20$
12	$P_t(\mu) < 9 \wedge \mathcal{O} > 0.9 \wedge \mathcal{R}_{WLS} > 0.7 \wedge (l_{Cand} - L_{CAL}) > -20$
13	$P_t(\mu) < 9 \wedge \mathcal{O} > 0.9 \wedge \mathcal{R}_{S} > 0.7 \wedge (l_{Cand} - L_{CAL}) > -20$
14	$P_t(\mu) < 9 \wedge \mathcal{O} > 0.9 \wedge \mathcal{R}_{\bar{B}} > 0.7 \wedge (l_{Cand} - L_{CAL}) > -20$
15	$P_t(\mu) < 9 \wedge \mathcal{O} > 0.9 \wedge \mathcal{R}_{\bar{B}S} > 0.7 \wedge (l_{Cand} - L_{CAL}) > -20$
101	$P_t(\mu) < 9 \wedge \mathcal{O} > 0.8 \wedge \mathcal{R} > 0.8$
102	$P_t(\mu) < 9 \wedge \mathcal{O} > 0.8 \wedge \mathcal{R}_{WLS} > 0.8$
103	$P_t(\mu) < 9 \wedge \mathcal{O} > 0.8 \wedge \mathcal{R}_{S} > 0.8$
104	$P_t(\mu) < 9 \wedge \mathcal{O} > 0.8 \wedge \mathcal{R}_{\bar{B}} > 0.8$
105	$P_t(\mu) < 9 \wedge \mathcal{O} > 0.8 \wedge \mathcal{R}_{\bar{B}S} > 0.8$
Muon candidate hit by two muon tracks	
201	$P_t(\mu) < 9 \wedge Algo = 2 \wedge N_{MuTrk}^{max} > 0 \wedge N_{MuTrk}^{max\text{-}1} > 0 \wedge \Delta\alpha_{MuTrk}^{max} < 0.1 \wedge \mathcal{R}_{\bar{B}S} > 0.5 \wedge \mathcal{O} > 0.7$
Muon candidate far away from beampipe and vertex	
301	$P_t(\mu) < 9 \wedge Algo = 1 \wedge d(l, BP) > 120 \wedge d(l, Vtx) > 200$
Event only consists of muon	
302	$P_t(\mu) < 1 \wedge E_{tot}(\mu) < 5 \wedge \mathcal{O} > 0.85 \wedge \mathcal{R}_{\bar{B}S} > 0.3 \wedge V_{fit} > 20 \wedge V_{fit} < 50 \wedge \Delta\alpha_{MuTrk}^{max} < 0.1$
continued on next page	

continued from previous page	
Type	Description, Cuts
Muon candidate very far away from vertex	
303	$P_t(\mu) < 5 \wedge \mathcal{O} > 0.7 \wedge d(l, Vtx) > 350 \wedge \mathcal{R}_{WLS} > 0.3 \wedge N^{max}_{MuTrk} > 0 \wedge \Delta\alpha^{max}_{MuTrk} < 0.1$
Muon candidate very far away from beampipe	
304	$P_t(\mu) < 2 \wedge \mathcal{O} = 1 \wedge V_{fit} > 20 \wedge V_{fit} < 40 \wedge d(l, BP) > 80 \wedge \mathcal{R} > 0.2 \wedge \mathcal{R}_{\bar{B}S} > 0.25 \wedge \mathcal{R}_{NB} > 0.35 \wedge \Delta\alpha^{max}_{MuTrk} < 0.1$
Muon candidates found by removing rings of cells around *FCAL* beampipe hole	
901	$Step > 0 \wedge P_t(\mu) < 1 \wedge \mathcal{R}_{NB} > 0.8 \wedge \mathcal{O} > 0.8 \wedge (l_{Cand} - L_{CAL}) > -20$
902	$P_t(\mu) < 1 \wedge V_{fit} > 20 \wedge V_{fit} < 40 \wedge (l_{Cand} - L_{CAL}) > -20 \wedge Algo = 1 \wedge \Delta\alpha^{max}_{MuTrk} < 0.1$
Muon types found using condensates only:	
Halo muon with or without showers	
1001	$\mathcal{O} > 0.9 \wedge \mathcal{R} > 0.9 \wedge 0.15 < L_\theta < (\pi - 0.15) \wedge L_\rho > 110$
1002	$\mathcal{O} > 0.9 \wedge \mathcal{R}_{WLS} > 0.9 \wedge 0.15 < L_\theta < (\pi - 0.15) \wedge L_\rho > 110$
1003	$\mathcal{O} > 0.9 \wedge \mathcal{R}_S > 0.9 \wedge 0.15 < L_\theta < (\pi - 0.15) \wedge L_\rho > 110$
1004	$\mathcal{O} > 0.9 \wedge \mathcal{R}_{NB} > 0.9 \wedge 0.15 < L_\theta < (\pi - 0.15) \wedge L_\rho > 110$
1101	$\mathcal{O} > 0.8 \wedge \mathcal{R} > 0.8 \wedge 0.15 < L_\theta < (\pi - 0.15) \wedge L_\rho > 110$
1102	$\mathcal{O} > 0.8 \wedge \mathcal{R}_{WLS} > 0.8 \wedge 0.15 < L_\theta < (\pi - 0.15) \wedge L_\rho > 110$
1103	$\mathcal{O} > 0.8 \wedge \mathcal{R}_S > 0.8 \wedge 0.15 < L_\theta < (\pi - 0.15) \wedge L_\rho > 110$
1104	$\mathcal{O} > 0.8 \wedge \mathcal{R}_{NB} > 0.8 \wedge 0.15 < L_\theta < (\pi - 0.15) \wedge L_\rho > 110$
1201	$\mathcal{O} > 0.7 \wedge \mathcal{R} > 0.7 \wedge 0.15 < L_\theta < (\pi - 0.15) \wedge L_\rho > 110$
1202	$\mathcal{O} > 0.7 \wedge \mathcal{R}_{WLS} > 0.7 \wedge 0.15 < L_\theta < (\pi - 0.15) \wedge L_\rho > 110$
1203	$\mathcal{O} > 0.7 \wedge \mathcal{R}_S > 0.7 \wedge 0.15 < L_\theta < (\pi - 0.15) \wedge L_\rho > 110$
1204	$\mathcal{O} > 0.7 \wedge \mathcal{R}_{NB} > 0.7 \wedge 0.15 < L_\theta < (\pi - 0.15) \wedge L_\rho > 110$
Halo muon traversing *BCAL EMC*, many cells hit but occupancy bad	
1301	$N^{Hit}_{Cells} > 20 \wedge L_\rho > 110 \wedge l_{Cand} > 50 \wedge 0.15 < L_\theta < (\pi - 0.15) \wedge \mathcal{R} > 0.65$
Muon candidates hit by *CTD* tracks	
1011	$\mathcal{O} > 0.9 \wedge \mathcal{R} > 0.9 \wedge N^{max}_{InTrk} > 0 \wedge \Delta\alpha^{max}_{InTrk} < 0.2$
1012	$\mathcal{O} > 0.9 \wedge \mathcal{R}_{WLS} > 0.9 \wedge N^{max}_{InTrk} > 0 \wedge \Delta\alpha^{max}_{InTrk} < 0.2$
1013	$\mathcal{O} > 0.9 \wedge \mathcal{R}_S > 0.9 \wedge N^{max}_{InTrk} > 0 \wedge \Delta\alpha^{max}_{InTrk} < 0.2$
continued on next page	

continued from previous page	
Type	Description, Cuts
1014	$\mathcal{O} > 0.9 \wedge \mathcal{R}_{NB} > 0.9 \wedge N^{max}_{InTrk} > 0 \wedge \Delta\alpha^{max}_{InTrk} < 0.2$
1111	$\mathcal{O} > 0.8 \wedge \mathcal{R} > 0.8 \wedge N^{max}_{InTrk} > 0 \wedge \Delta\alpha^{max}_{InTrk} < 0.2$
1112	$\mathcal{O} > 0.8 \wedge \mathcal{R}_{WLS} > 0.8 \wedge N^{max}_{InTrk} > 0 \wedge \Delta\alpha^{max}_{InTrk} < 0.2$
1113	$\mathcal{O} > 0.8 \wedge \mathcal{R}_{S} > 0.8 \wedge N^{max}_{InTrk} > 0 \wedge \Delta\alpha^{max}_{InTrk} < 0.2$
1114	$\mathcal{O} > 0.8 \wedge \mathcal{R}_{NB} > 0.8 \wedge N^{max}_{InTrk} > 0 \wedge \Delta\alpha^{max}_{InTrk} < 0.2$
Muon candidates hit by $3-D$ muon chamber tracks	
1012	$\mathcal{O} > 0.9 \wedge \mathcal{R} > 0.9 \wedge N^{max}_{MuTrk} > 0$
1022	$\mathcal{O} > 0.9 \wedge \mathcal{R}_{WLS} > 0.9 \wedge N^{max}_{MuTrk} > 0$
1023	$\mathcal{O} > 0.9 \wedge \mathcal{R}_{S} > 0.9 \wedge N^{max}_{MuTrk} > 0$
1024	$\mathcal{O} > 0.9 \wedge \mathcal{R}_{NB} > 0.9 \wedge N^{max}_{MuTrk} > 0$
1121	$\mathcal{O} > 0.8 \wedge \mathcal{R} > 0.8 \wedge N^{max}_{MuTrk} > 0$
1122	$\mathcal{O} > 0.8 \wedge \mathcal{R}_{WLS} > 0.8 \wedge N^{max}_{MuTrk} > 0$
1123	$\mathcal{O} > 0.8 \wedge \mathcal{R}_{S} > 0.8 \wedge N^{max}_{MuTrk} > 0$
1124	$\mathcal{O} > 0.8 \wedge \mathcal{R}_{NB} > 0.8 \wedge N^{max}_{MuTrk} > 0$
Muon candidate hit by muon chamber tracks that does not traverse the inner detector volume	
1125	$\mathcal{O} > 0.7 \wedge \mathcal{R}_{NB} > 0.7 \wedge N^{max}_{MuTrk} > 0 \wedge \Delta\alpha^{max}_{MuTrk} < 0.1 \wedge l(l, InnerDet) = 0$
Muon candidate hit by muon chamber tracks with velocity near c	
1126	$\mathcal{O} > 0.75 \wedge \mathcal{R}_{S} > 0.75 \wedge N^{max}_{MuTrk} > 0 \wedge \Delta\alpha^{max}_{MuTrk} < 0.2 \wedge V_{fit} > 20 \wedge V_{fit} < 40$
Muon candidates hit by muon wire chamber $2-D$ tracks	
1031	$\mathcal{O} > 0.9 \wedge \mathcal{R} > 0.9 \wedge \Delta d^{min}_{MuWire} < 20$
1032	$\mathcal{O} > 0.9 \wedge \mathcal{R} > 0.9 \wedge \Delta\alpha^{min}_{MuWire} < 0.2$
1033	$\mathcal{O} > 0.9 \wedge \mathcal{R}_{WLS} > 0.9 \wedge \Delta d^{min}_{MuWire} < 20$
1034	$\mathcal{O} > 0.9 \wedge \mathcal{R}_{WLS} > 0.9 \wedge \Delta\alpha^{min}_{MuWire} < 0.2$
1035	$\mathcal{O} > 0.7 \wedge \mathcal{R}_{WLS} > 0.5 \wedge \Delta\alpha^{min}_{MuWire} < 0.1 \wedge \Delta d^{min}_{MuWire} < 40 \wedge d(l, BP) > 120$
1036	$\mathcal{O} > 0.9 \wedge \mathcal{R}_{S} > 0.9 \wedge \Delta d^{min}_{MuWire} < 20 \wedge \Delta\alpha^{min}_{MuWire} < 0.1$
1037	$\mathcal{O} > 0.65 \wedge \mathcal{R} > 0.7 \wedge 0.15 < L_{\theta} < (\pi - 0.15) \wedge L_{\rho} > 110 \wedge \Delta d^{min}_{MuWire} < 5 \wedge \Delta\alpha^{min}_{MuWire} < 0.1$
Muon candidates that are **not** hit by an inner track	
1041	$\mathcal{O} > 0.9 \wedge \mathcal{R} > 0.9 \wedge N^{max}_{InTrk} = 0$
1042	$\mathcal{O} > 0.9 \wedge \mathcal{R}_{WLS} > 0.9 \wedge N^{max}_{InTrk} = 0$
1141	$\mathcal{O} > 0.9 \wedge \mathcal{R} > 0.8 \wedge N^{max}_{InTrk} = 0$
1142	$\mathcal{O} > 0.9 \wedge \mathcal{R}_{WLS} > 0.8 \wedge N^{max}_{InTrk} = 0$
continued on next page	

continued from previous page

Type	Description, Cuts
Muon candidates far away from vertex and beampipe	
1151	$\mathcal{O} > 0.7 \wedge \mathcal{R}_{WLS} > 0.5 \wedge d(l, BP) > 120$
Muon candidates with velocity near c	
1501	$\mathcal{O} > 0.8 \wedge \mathcal{R}_{WLS} > 0.6 \wedge V_{fit} < 50 \wedge \Delta\alpha^{min}_{MuWire} < 0.1 \wedge \Delta d^{min}_{MuWire} < 20$
1502	$P_t(\mu) < 1 \wedge E_{tot}(\mu) < 5 \wedge \mathcal{O} > 0.9 \wedge \mathcal{R}_{\bar{B}S} > 0.6 \wedge V_{fit} > 20 \wedge V_{fit} < 60$
1503	$P_t(\mu) < 1 \wedge E_{tot}(\mu) < 2 \wedge \mathcal{O} > 0.7 \wedge \mathcal{R}_{\bar{B}S} > 0.7 \wedge V_{fit} > 20 \wedge V_{fit} < 60$
1504	$P_t(\mu) < 1 \wedge \mathcal{O} > 0.8 \wedge \mathcal{R}_{\bar{B}S} > 0.9 \wedge \mathcal{R} > 0.7 \wedge V_{fit} > 20 \wedge V_{fit} < 60 \wedge d(l, Vtx) > 50$
1505	$P_t(\mu) < 5 \wedge \mathcal{O} > 0.85 \wedge \mathcal{R} > 0.75 \wedge d(l, Vtx) > 50 \wedge V_{fit} > 20 \wedge V_{fit} < 60$
Event consists only of muons	
1506	$P_t(\mu) < 1 \wedge E_{tot}(\mu) < 2 \wedge \mathcal{O} > 0.7 \wedge \mathcal{R}_{\bar{B}S} > 0.5 \wedge \Delta d^{min}_{MuWire} < 20 \wedge \Delta\alpha^{min}_{MuWire} < 0.1 \wedge \Delta d^{min}_{MuStrip} < 20 \wedge \Delta\alpha^{min}_{MuStrip} < 0.1 \wedge d(l, Vtx) > 100 \wedge V_{fit} > 20 \wedge V_{fit} < 60$
Muon candidates found by removing rings of cells around *FCAL* beampipe hole	
1901	$Step > 0 \wedge P_t(\mu) < 3 \wedge \mathcal{O} > 0.9 \wedge \mathcal{R}_{WLS} > 0.6 \wedge \Delta d^{min}_{MuWire} < 10 \wedge \Delta\alpha^{min}_{MuWire} < 0.1 \wedge \Delta d^{min}_{MuStrip} < 10 \wedge \Delta\alpha^{min}_{MuStrip} < 0.1 \wedge V_{fit} > 20 \wedge V_{fit} < 40$
1902	$Step > 0 \wedge P_t(\mu) < 1 \wedge \mathcal{O} > 0.9 \wedge \mathcal{R} > 0.75 \wedge \mathcal{R}_{NB} > 0.85$
1903	$Step > 0 \wedge P_t(\mu) < 1.5 \wedge \mathcal{O} > 0.95 \wedge \mathcal{R} > 0.65 \wedge \mathcal{R}_{\bar{B}S} > 0.9 \wedge V_{fit} > 20 \wedge V_{fit} < 40 \wedge \Delta d^{min}_{MuWire} < 5 \wedge \Delta\alpha^{min}_{MuWire} < 0.1$
1904	$Step > 0 \wedge P_t(\mu) < 1 \wedge \mathcal{O} > 0.75 \wedge \mathcal{R} > 0.7 \wedge \Delta d^{min}_{MuWire} < 40 \wedge \Delta\alpha^{min}_{MuWire} < 0.1 \wedge d(l, Vtx) > 300$
1905	$Step > 0 \wedge P_t(\mu) < 1.5 \wedge \mathcal{O} > 0.85 \wedge \mathcal{R}_{\bar{B}S} > 0.75 \wedge V_{fit} > 10 \wedge V_{fit} < 50 \wedge d(l, Vtx) > 250$
Halo muons close to the beampipe:	
2001	$P_t(\mu) < 9 \wedge \mathcal{O} > 0.9 \wedge \mathcal{R} > 0.9 \wedge (L_\theta < 0.1 \vee L_\theta > (\pi - 0.1))$
2002	$P_t(\mu) < 9 \wedge \mathcal{O} > 0.9 \wedge \mathcal{R}_{NB} > 0.9 \wedge (L_\theta < 0.1 \vee L_\theta > (\pi - 0.1))$

continued on next page

continued from previous page	
Type	Description, Cuts
2011	$R_t(\mu) < 9 \wedge \mathcal{O} > 0.9 \wedge \mathcal{R}_{NB} > 0.6 \wedge (L_\theta < 0.1 \vee L_\theta > (\pi - 0.1))$
2012	$R_t(\mu) < 9 \wedge \mathcal{O} > 0.8 \wedge \mathcal{R}_{NB} > 0.8 \wedge (L_\theta < 0.1 \vee L_\theta > (\pi - 0.1))$
2013	$R_t(\mu) < 1 \wedge E_{tot}(\mu) < 5 \wedge \mathcal{O} > 0.8 \wedge \mathcal{R}_S > 0.3 \wedge (L_\theta < 0.1 \vee L_\theta > (\pi - 0.1))$
2014	$R_t(\mu) < 1 \wedge E_{tot}(\mu) < 5 \wedge \mathcal{O} > 0.75 \wedge \mathcal{R}_{\bar{B}S} > 0.2 \wedge (L_\theta < 0.1 \vee L_\theta > (\pi - 0.1))$
2015	$R_t(\mu) < 1.5 \wedge \mathcal{O} = 1 \wedge \mathcal{R}_{\bar{B}S} = 1 \wedge (L_\theta < 0.1 \vee L_\theta > (\pi - 0.1)) \wedge V_{fit} > 30 \wedge V_{fit} < 36$
Muons found by condensate timing based finder:	
3001	$R_t(\mu) < 2 \wedge \mathcal{R} > 0.3 \wedge \mathcal{O} > 0.8 \wedge V_{fit} < 60$
3002	$R_t(\mu) < 4 \wedge \mathcal{O} > 0.9 \wedge (N^{Hit}_{Cells} + N^{NB}_{Cells})/N_{Cells} > 0.7 \wedge N^{max}_{MuTrk} > 0 \wedge N^{max\text{-}1}_{MuTrk} > 0 \wedge N^{max}_{InTrk} > 0 \wedge N^{max\text{-}1}_{InTrk} > 0 \wedge V_{fit} < 60$
3003	$R_t(\mu) < 1 \wedge (N^{Hit}_{Cells} + N^{NB}_{Cells})/N_{Cells} > 0.5 \wedge N^{max}_{MuTrk} > 0 \wedge \Delta\alpha^{max}_{MuTrk} < 0.1 \wedge V_{fit} < 60 \wedge \lvert l_{Cand} - L_{CAL}\rvert < 100$
3004	$R_t(\mu) < 9 \wedge \mathcal{R} > 0.9 \wedge \mathcal{O} > 0.7 \wedge \Delta\alpha^{max}_{MuTrk} < 0.1$
3005	$R_t(\mu) < 1 \wedge E_{tot}(\mu) < 5 \wedge \mathcal{R} > 0.2 \wedge \mathcal{O} > 0.9 \wedge V_{fit} < 60$
3006	$R_t(\mu) < 1.5 \wedge E_{tot}(\mu) < 5 \wedge \mathcal{R} > 0.15 \wedge \mathcal{O} > 0.95 \wedge N^{max}_{MuTrk} > 0 \wedge \Delta\alpha^{max}_{MuTrk} < 0.2 \wedge V_{fit} < 60$
3007	$R_t(\mu) < 2 \wedge E_{tot}(\mu) < 5 \wedge \mathcal{R} > 0.1 \wedge \mathcal{O} > 0.90 \wedge \Delta d^{min}_{MuWire} < 20 \wedge \Delta\alpha^{min}_{MuWire} < 0.1 \wedge \Delta d^{min}_{MuStrip} < 20 \wedge \Delta\alpha^{min}_{MuStrip} < 0.1 \wedge V_{fit} < 60 \wedge d(l, Vtx) > 50$
3008	$R_t(\mu) < 2 \wedge \mathcal{R} > 0.2 \wedge \mathcal{O} = 1 \wedge N^{max}_{MuTrk} > 0 \wedge \Delta\alpha^{max}_{MuTrk} < 0.1 \wedge \Delta d^{min}_{MuStrip} < 20 \wedge \Delta\alpha^{min}_{MuStrip} < 0.2 \wedge V_{fit} > 20 \wedge V_{fit} < 40 \wedge d(l, Vtx) > 50$
Muon candidates found by removing rings of cells around *FCAL* beampipe hole	
3901	$Step > 0 \wedge L_\theta < 0.1 \wedge R_t(\mu) < 1 \wedge V_{fit} > 20 \wedge V_{fit} < 40 \wedge \mathcal{O} = 1 \wedge \mathcal{R}_{\bar{B}S} > 0.3 \wedge N^{max}_{InTrk} > 0 \wedge \Delta\alpha^{max}_{InTrk} < 0.1$
continued on next page	

continued from previous page	
Type	Description, Cuts
3902	$Step > 0 \wedge L_\theta < 0.1 \wedge P_t(\mu) < 1 \wedge V_{fit} > 20 \wedge V_{fit} < 40 \wedge \mathcal{O} = 1 \wedge \mathcal{R}_{\bar{B}S} > 0.55$
3903	$Step > 0 \wedge P_t(\mu) < 1 \wedge V_{fit} > 20 \wedge V_{fit} < 40 \wedge \mathcal{O} > 0.95 \wedge \mathcal{R} > 0.8 \wedge \mathcal{R}_{\bar{B}S} = 1$

Table 6.2: Cuts used to classify muon candidates.

6.10 Summary

Of the 693 candidate CC events 489 are rejected due to being identified as events with overlapping muons. Table 6.3 gives a breakdown of the number of events rejected by each of the muon finder algorithms.

Muon Finder Algorithm	Number of Events
Muon track based finder	241
Condensate based finder	195
Beam pipe halomuon finder	28
Condensate timing based finder	25

Table 6.3: The table gives a breakdown of the number of events rejected by each of the muon finder algorithms.

Figure 6.9 shows the velocity distribution of all candidates while figure 6.13 shows the orientation of the fitted trajectory. The peaks in histogram (a) at very small and high azimuthal angles θ stem from halo muons. The halo muon events have been removed from histogram (b) for the polar angle ϕ. Histogram (b) only has entries for ϕ values between $0°$ and $180°$. This is due to the fact that during the trajectory fits ϕ is chosen such that the trajectory points upwards, away from earth. The velocity fitted to almost all of these candidates is negative, indicating that cosmics come from above.

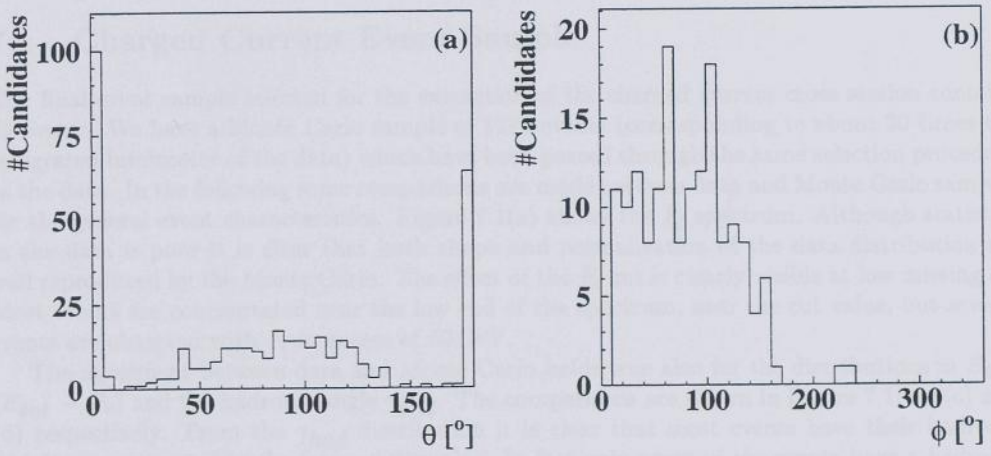

Figure 6.13: Figure (a) shows the distribution of the polar angle θ for all identified muons. The peaks at low and high angles correspond to halo muons, these have been omitted in figure (b) which shows the distribution for the azimuthal angle ϕ. Histogram (b) only shows ϕ values between $0°$ and $180°$. This is due to the fact that during the trajectory fits ϕ is chosen such that the trajectory points upwards, away from earth.

Chapter 7

Results

7.1 Charged Current Event Sample

The final event sample selected for the extraction of the charged current cross section contains 49 events. We have a Monte Carlo sample of 1275 events (corresponding to about 30 times the integrated luminosity of the data) which have been passed through the same selection procedure as the data. In the following some comparisons are made between data and Monte Carlo samples for the general event characteristics. Figure 7.1(a) shows the $\not{P}_t$ spectrum. Although statistics in the data is poor it is clear that both shape and normalization of the data distribution are well reproduced by the Monte Carlo. The effect of the $\not{P}_t$ cut is clearly visible at low missing P_t. Most events are concentrated near the low end of the spectrum, near the cut value, but several events are observed with $\not{P}_t$ in excess of 50 GeV.

The agreement between data and Monte Carlo holds true also for the distributions in E_{tot}, $(E_{tot} - P_z)$ and the hadronic angle γ_{had}. The comparisons are shown in Figure 7.1(b), (c) and (d) respectively. From the γ_{had} distribution it is clear that most events have their hadronic activity concentrated in the forward direction. In fact only seven of the events have a hadronic angle larger than 90°. At small forward angles the effect of the beam pipe hole is clearly visible. All events have large total energies ranging from 50 GeV to over 300 GeV.

Figures 7.2 through 7.5 show event pictures of some typical events from the sample, shown with the *ZEUS* event display program LAZE [41]. The kinematic variables for those events are listed in table 7.1.

Figure	$\not{P}_t$ (GeV)	Q^2_{jb} (GeV^2)	x_{jb}	y_{jb}
figure 7.2	64.8	6026.5	0.302	0.221
figure 7.3	11.2	134.3	0.23	0.062
figure 7.4	15.4	533.9	0.01	0.554
figure 7.5	63.9	4983.0	0.181	0.304

Table 7.1: $\not{P}_t$, Q^2_{jb}, x_{jb} and y_{jb} for the events shown in figures figure 7.2 through 7.5.

In general the events in the final sample have characteristics which are in good agreement with the expectation we have for charged current scattering events.

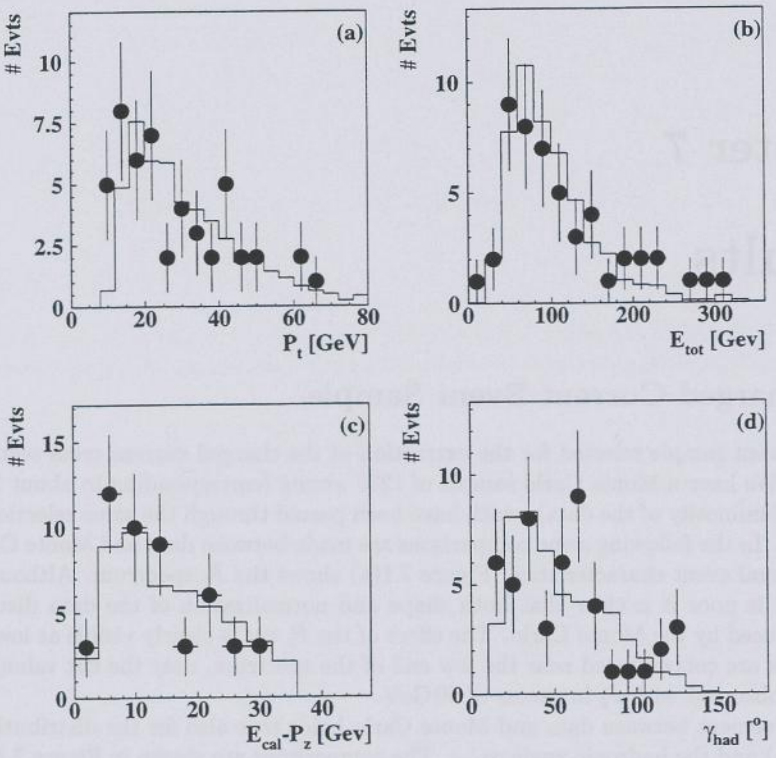

Figure 7.1: The distributions show the missing transverse momentum $\not{P}_t$ (a), total energy in the calorimeter E_{tot} (b), $(E_{tot} - P_z)$ (c) and the hadronic angle γ_{had} (d) of the final data (circles) together with the statistical errors in comparison to the Monte Carlo data (histogram).

We now turn to the reconstruction of the kinematic variables x and Q^2 for the events in the final sample. As mentioned previously (see section 2.4) the absence of a measurable lepton in the final state in charged current scattering forces us to reconstruct the kinematics of the events from the hadronic system alone. Therefore the only reconstruction method available is that of the Jacquet-Blondel estimators:

$$
\begin{aligned}
y_{jb} &= \frac{E_{tot} - P_z}{2 * E_e} \\
Q^2_{jb} &= \frac{{P_t}^2}{1 - y_{jb}} \\
x_{jb} &= \frac{Q^2_{jb}}{4 * E_e * E_p * y_{jb}}
\end{aligned}
$$

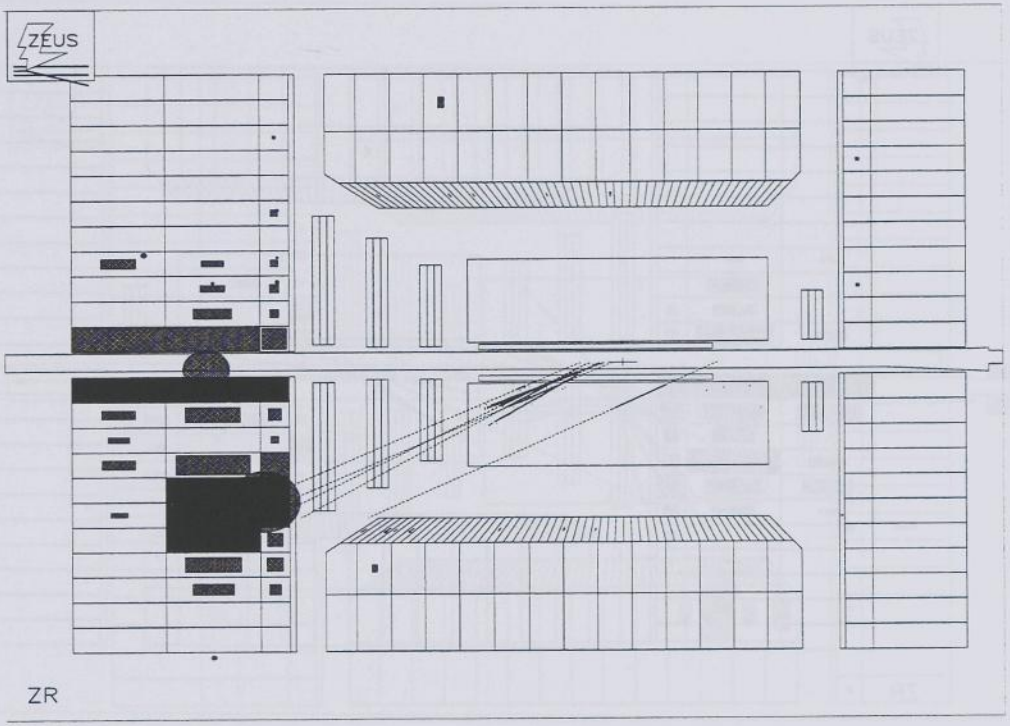

Figure 7.2: The charged current event shown has the highest $\not{P}_t$ in the sample. $\not{P}_t = 64.8\,\mathrm{GeV}$.

In our case the value of $(E_{tot} - P_z)$ is calculated from the energy deposits in the calorimeter and the angle of the center of the calorimeter cells with respect to the measured vertex, i.e.:

$$y_{jb} = \frac{1}{2 * E_e} \sum_{cell} E_{cell}(1 - \cos\theta_{cell}) \tag{7.1}$$

$$P_x = \sum_{cell} E_{cell} \sin\theta_{cell} \cos\phi_{cell} \tag{7.2}$$

$$P_y = \sum_{cell} E_{cell} \sin\theta_{cell} \sin\phi_{cell} \tag{7.3}$$

$$P_t^2 = (P_x^2 + P_y^2) \tag{7.4}$$

Figure 7.6 and figure 7.7 show the distribution in x_{jb} and Q^2_{jb} of the final event sample and the selected Monte Carlo events respectively. The events are distributed at Q^2 values greater than $100\,\mathrm{GeV}^2$ due to the $\not{P}_t$ cut required in the selection of the data. Shown by the dotted lines in the figure are the lines of constant $P_t = 9, 12, 15, 18\,\mathrm{GeV}$ indicating the range over which the selection efficiency turns on. Also shown (dash dotted) is the line for $\gamma_{had} = 15\,^\circ$, where the effect of the beam pipe restricts our selection. The beam pipe hole does not result in a strict angle cut because it depends on the event topology, whether or not an event with γ_{had} close to the cut leads to the rejection of the event. Finally the dashed line indicates the line $y = \frac{35}{2E_e}$,

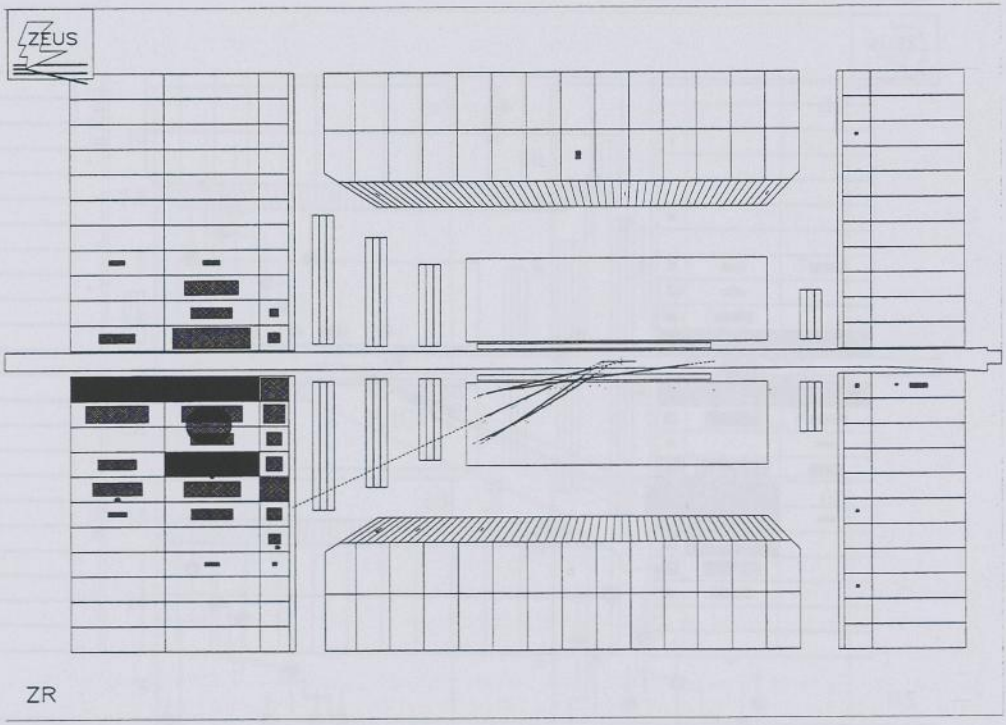

Figure 7.3: The charged current event shown has $P_t = 11.2\,\text{GeV}$.

above which the $(E_{tot} - P_z)$ of the event would be greater than the cut of $E_{tot} - P_z > 35\,\text{GeV}$.

7.2 Measurement of the Differential Cross Sections

To measure the differential cross sections we have divided the data in bins of x and in bins of Q^2. The present statistics does not allow for the determination of the double differential cross section. The bins in Q^2 have been chosen as indicated in table 7.2. The number of selected data events in the bins is also given. The bins have been chosen equidistant in $logQ^2$, in such a way that the statistics in each bin is acceptable and the widths are relatively large compared to the resolution in Q^2. Figure 7.8 shows the distribution of the deviation of the reconstructed Q^2 from the true value for each of the chosen bins for events in the selected sample of Monte Carlo events. The r.m.s. width of the distributions is also indicated in table 7.2. Figure 7.8 shows that even though the distributions are reasonably Gaussian and the r.m.s. is relatively small, the central value is shifted, indicating a reconstruction of Q^2 which is systematically low. This is an effect of the energy loss in the hadronic system due to inactive material in the detector in front of the calorimeters. The relative bias is also given for each bin in table 7.2.

Table 7.3 gives the chosen bins in x together with the number of reconstructed events from the final data sample in each. Figure 7.9 shows the distributions for the deviation of reconstructed x from the true value again for the final selected Monte Carlo sample. Particularly in the higher

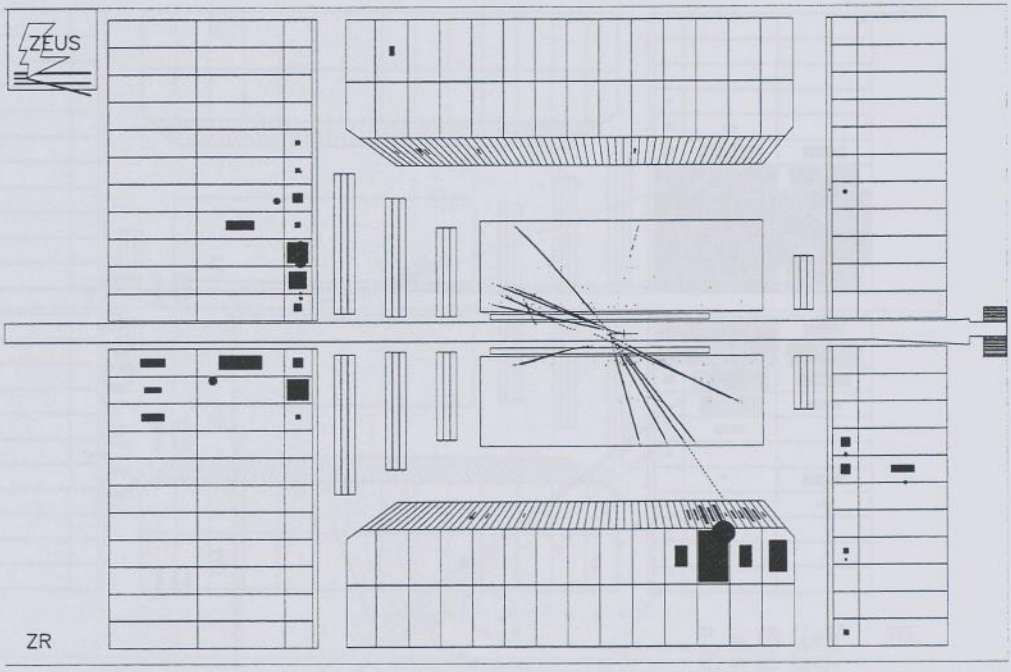

Figure 7.4: The charged current event shown has the largest hadronic angle γ_{had} in the sample: $\gamma_{had} = 126.3°$.

x bins the distributions become asymmetric and are again biased towards lower reconstructed values. Table 7.3 also lists the r.m.s. width of the distributions and the mean deviation.

7.3 Reconstruction of the True Distributions

The reconstructed x and Q^2 are biased and spread. Consequently one is forced to correct for this using the Monte Carlo. The method we use here is to calculate a transport matrix which quantifies the migration of events: It gives for all true bins the fraction of the events that end up in a certain bin of the measured distribution.

Figure 7.10 shows the transport matrix for Q^2. Obviously the inverse of this matrix, applied to the events in reconstructed bins gives the measured true number of events in the Q^2 bins. Table 7.2 gives the corrected number of events in bins of Q^2.

Figure 7.11 shows the transport matrix for x which has been obtained in the same way as for Q^2. Table 7.3 gives the corrected number of events in the x bins.

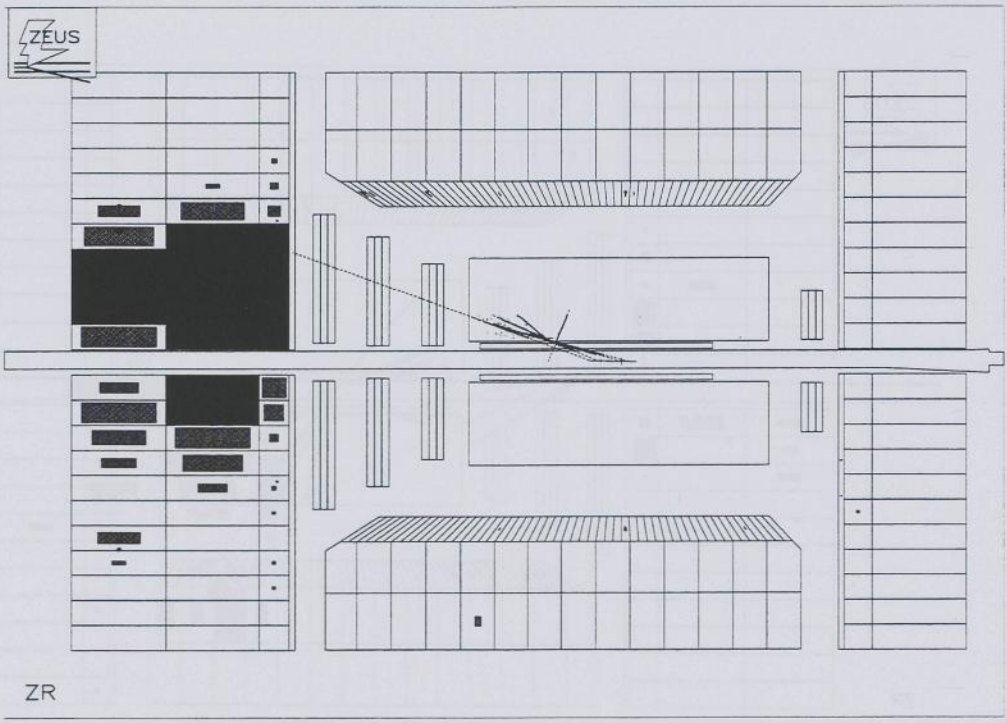

Figure 7.5: The charged current event shown has the lowest hadronic angle γ_{had} in the sample: $\gamma_{had} = 18.2°$.

7.4 Detector and Trigger Acceptance

The detector and trigger acceptance can be determined with the Monte Carlo data sample. The detector acceptance is defined as the fraction of generated events which pass the trigger and all selection cuts. The acceptance of the trigger and selection cuts is shown in figure 7.12 in bins of Q^2 and x respectively.

For Q^2 the acceptance grows from $Q^2 = 100\,\mathrm{GeV}^2$ reaching a maximum acceptance of 60 % at $Q^2 = 300\,\mathrm{GeV}^2$.

The acceptance loss of 40 % is due to the loss of events at high x due to the beam pipe hole.

In x the acceptance starts at $x = 10^{-2.5}$ and rises to a maximum of 55 % at $x = 10^{-1.5}$ falling again at large x due to the beam pipe cut.

The measured distributions (see tables 7.2 and 7.3) need to be corrected for acceptance. This is done by multiplying each bin with the inverse of the acceptance measured for the Monte Carlo data sample. The final columns in tables 7.2 and 7.3 show the number of events corrected for acceptance together with the statistical error. The measured differential cross section is then determined by dividing the corrected number of events by the luminosity and the bin width. The point at which we quote the cross sections is determined as the mean value of x and Q^2 from the Monte Carlo *true* distributions. Tables 7.4 and 7.5 give the differential cross sections as a function of Q^2 and x respectively.

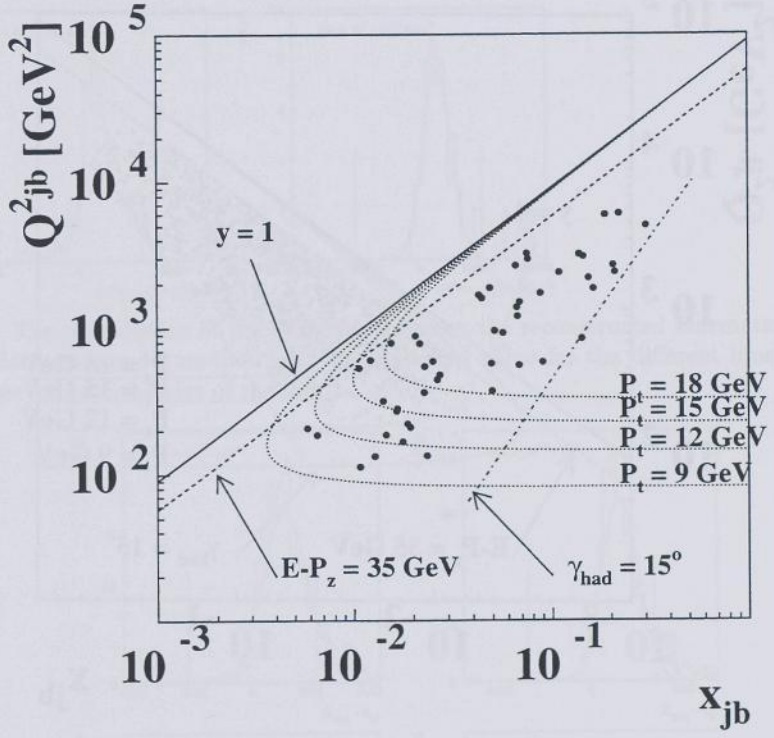

Figure 7.6: The distribution of the kinematic variables Q^2 versus x for the selected data, calculated using the Jacquet-Blondel estimators. The lines indicate the effect of the major various selection cuts: $E_{tot} - P_z = 35\,\mathrm{GeV}$ (dashed), $\gamma_{had} = 15^\circ$ (dash-dotted) and $P_t = 9, 12, 15, 18\,\mathrm{GeV}$ (dotted). The solid line indicates the kinematical limit ($y = 1$).

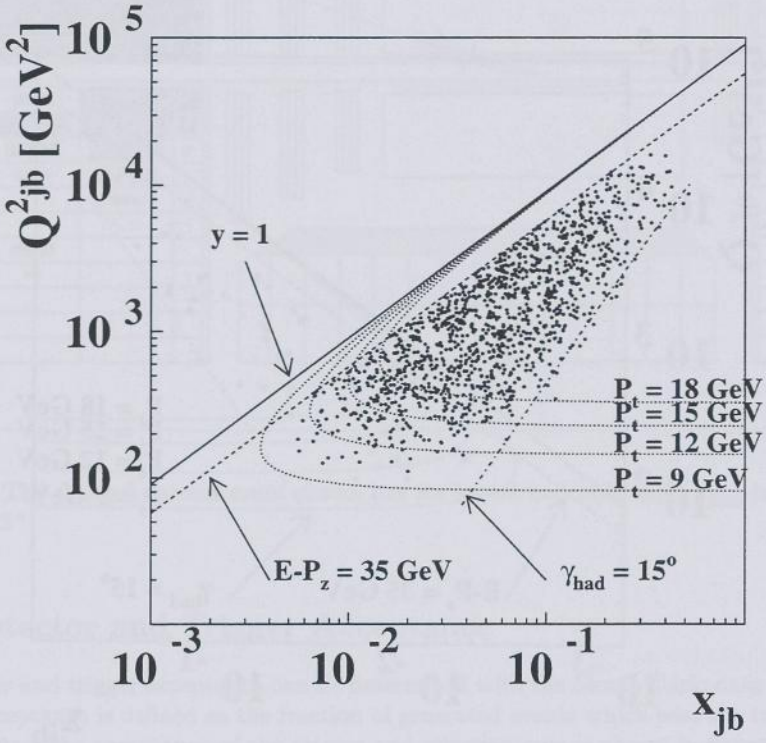

Figure 7.7: The distribution of the kinematic variables Q^2 versus x for the Monte Carlo data that passes the selection cuts, calculated using the Jacquet-Blondel estimators. The lines indicate the effect of the major various selection cuts: $E_{tot} - P_z = 35\,\text{GeV}$ (dashed), $\gamma_{had} = 15^\circ$ (dash-dotted) and $P_t = 9, 12, 15, 18\,\text{GeV}$ (dotted). The solid line indicates the kinematical limit ($y = 1$).

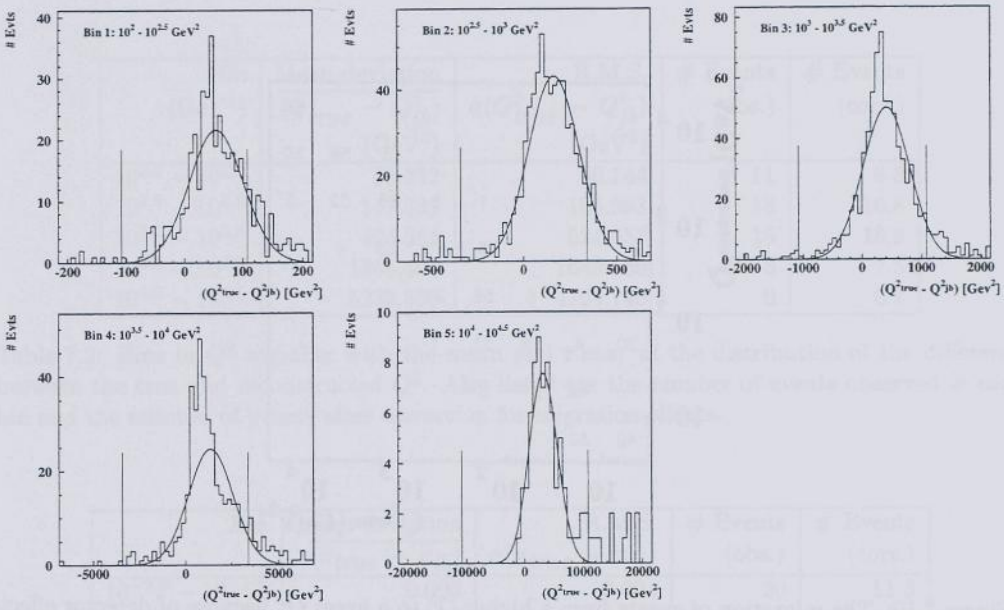

Figure 7.8: The distribution of the difference between the reconstructed kinematic variable Q^2 using the Jacquet-Blondel method and the generated value for the different bins in Q^2. The vertical lines indicate the size of the bin.

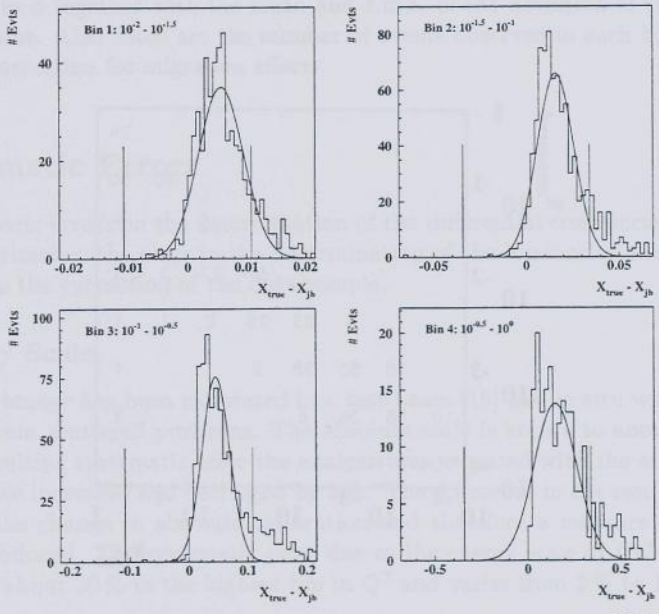

Figure 7.9: The distribution of the difference between the reconstructed kinematic variable x using the Jacquet-Blondel method and the generated value for the different bins in x. The vertical lines indicate the size of the bin.

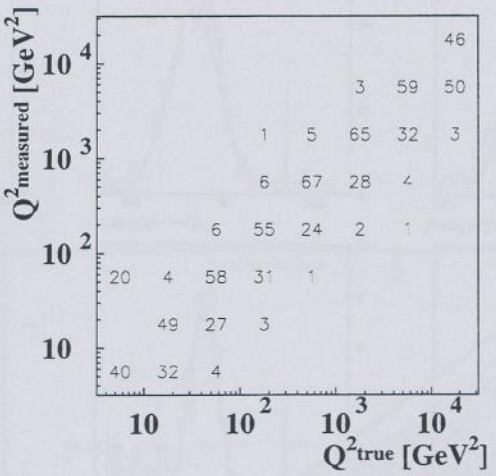

Figure 7.10: The migration of events from a higher Q^2 to a lower Q^2 because of detector effects: For events in a Q^2_{true} bin the numbers in the column above show what percentage of those events is reconstructed in a $Q^2_{measured}$ bin. Only about 50 % of the events remain in their bin. Towards the lower and higher ends of the histogram the statistics are poor and so the numbers inaccurate.

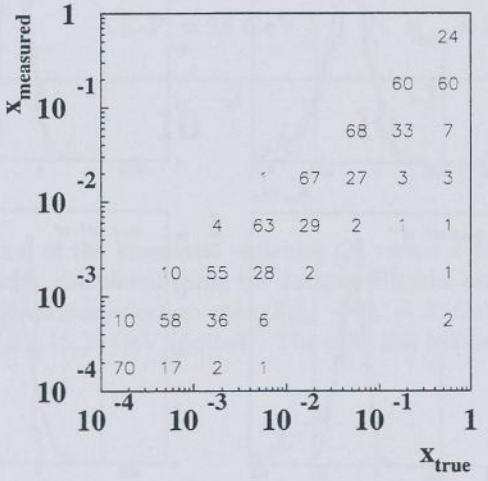

Figure 7.11: The migration of events in x because of detector effects: For events in a x_{true} bin the numbers in that bin show what percentage of those events is reconstructed in a $x_{measured}$ bin. Only about 50 % of the events remain in their bin.

Bin (GeV^2)	Mean deviation $\overline{(Q^2_{true} - Q^2_{jb})}$ (GeV^2)	R.M.S. $\sigma(Q^2_{true} - Q^2_{jb})$ (GeV^2)	# Events (obs.)	# Events (corr.)
$10^{2.0} - 10^{2.5}$	55.322	60.144	11	6.8
$10^{2.5} - 10^{3.0}$	147.833	185.993	18	16.8
$10^{3.0} - 10^{3.5}$	404.364	524.057	15	16.9
$10^{3.5} - 10^{4.0}$	1365.400	1649.530	5	7.5
$10^{4.0} - 10^{4.5}$	5232.350	4764.740	0	0.7

Table 7.2: Bins in Q^2 together with the mean and r.m.s. of the distribution of the difference between the true and reconstructed Q^2. Also listed are the number of events observed in each bin and the number of events after correction for migration effects.

Bin	Mean deviation $\overline{(x_{true} - x_{jb})}$	R.M.S. $\sigma(x_{true} - x_{jb})$	# Events (obs.)	# Events (corr.)
$10^{-2.0} - 10^{-1.5}$	0.006	0.004	20	11.3
$10^{-1.5} - 10^{-1.0}$	0.018	0.014	16	18.0
$10^{-1.0} - 10^{-0.5}$	0.059	0.045	11	15.0
$10^{-0.5} - 10^{0.0}$	0.195	0.134	0	2.5

Table 7.3: Bins in x together with the mean and r.m.s. of the deviation of the reconstructed x from the true value. Also listed are the number of events observed in each bin and the number of events after correction for migration effects.

7.5 Systematic Errors

Relevant systematic errors on the determination of the differential cross sections are the energy scale of the calorimeter, the error in the determination of the luminosity and the effects of the cuts employed in the extraction of the data sample.

7.5.1 Energy Scale

The *ZEUS* calorimeter has been calibrated in a test beam [19] and in situ with halo muons [42] and neutral current scattered positrons. The absolute scale is known to about 3 %. In order to calculate the resulting systematic error the analysis was repeated with the energy in the Monte Carlo data sample increased and decreased by 3 %. The difference in the resulting cross sections is only due to the change in absolute calibration and therefore a measure for the systematic uncertainty introduced. The systematic error due to the energy scale of *UCAL* varies from 2 % in the lowest to about 30 % in the highest bin in Q^2 and varies from 2 % to 10 % in x.

7.5.2 Luminosity

The *ZEUS* luminosity is known to 1 % ([21, 22]). The resulting systematic uncertainty was calculated by changing the total luminosity by the error and taking the difference in the results

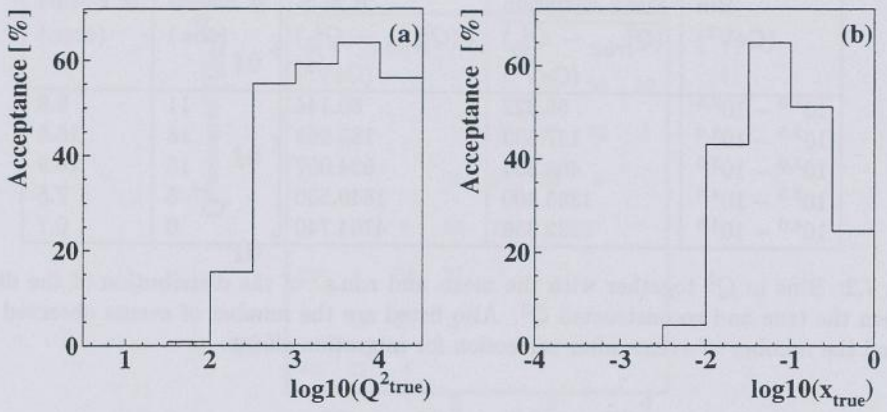

Figure 7.12: The acceptance of the trigger and selection cuts for Monte Carlo events in bins of the measured Q^2 (a) and x (b). Events have been generated with $Q^2 > 10\,\mathrm{GeV}^2$ but through the trigger cuts none of the events at low Q^2 is left in the sample.

as a measure for the systematic uncertainty. Since the resulting differential cross sections are inversely proportional to the luminosity the systematic error due to the uncertainty in the luminosity measurement is 1 %.

7.5.3 Background from Non *e-p*-Collision Events

Beam gas and cosmic muon events are rejected by the online trigger system and in the offline selection through a series of algorithms and cuts which are described in chapter 5. From the vertex distribution and scanning of the events we concluded that there were no obvious non *e-p* events left in the sample. We thus assign an upper limit of 1 event for the non *e-p* background. This corresponds to about 2 % of the sample, so we assign a systematic error of $-2\,\%$ to all bins.

7.5.4 Background from *e-p* Events

Neutral current events are rejected by requiring $\not{P}_t > 9\,\mathrm{GeV}$ and $E_{tot} - P_z < 35\,\mathrm{GeV}$. Photoproduction events are rejected by requiring $\not{P}_t > 9\,\mathrm{GeV}$ and $\frac{P_t}{E_t} > 0.5$. It is not possible due to the low statistics to systematically study these backgrounds. We rely on the scanning of the events and find no events which are inconsistent with CC event topology except in the lowest Q^2-bin.

Here 5 events were found that were not clear background events but are not guaranteed CC-events either. One of these events is shown in figure 7.13. These events are all characterized by two muons in the final state. The momentum of the muon tracks is so large that the momentum measurement by the *CTD* leads to large errors and so it is not possible to calculate whether the muon momentum would balance the $\not{P}_t$ of the event and base a cut on that. Even though it is possible to clearly identify these events through scanning we do not want to use scanning as a means of rejecting events: The efficiency and purity of the scanning method can not be

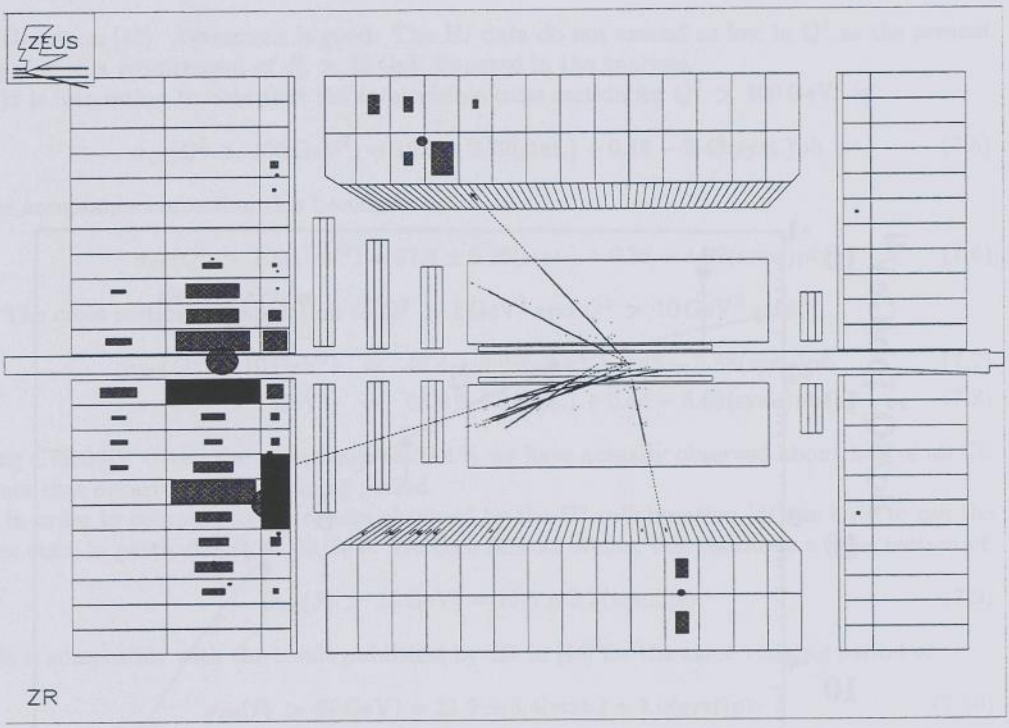

Figure 7.13: The charged current candidate event shown has a jet in the *FCAL* and two prompt muons which enter the *BCAL*.

measured. Moreover it is possible that these events are genuine charged current events. For this reason we choose to keep the events in the sample and assign a systematic error due to these events which contribute to the lowest Q^2-bin.

Scanning of the events rejected by the muon finder showed that in all cases a muon caused the rejection of the event. Furthermore no events were rejected in the Monte Carlo data sample. Therefore we consider the systematic error due to the Muon rejection to be negligible.

7.6 Statistical Errors

The statistical uncertainty was calculated assuming that the distributions in each bin follow a Poisson statistic.

7.7 Results

Table 7.4 lists the differential cross section $\frac{d\sigma}{dQ^2}$ for e^+-p scattering together with the statistical and systematic error and in figure 7.14 the values are shown together with a theoretical calculation using the CTEQ4D parton densities. The results are in good agreement with the theoretical prediction. Also shown are the results for the differential cross section as measured by the *H1*

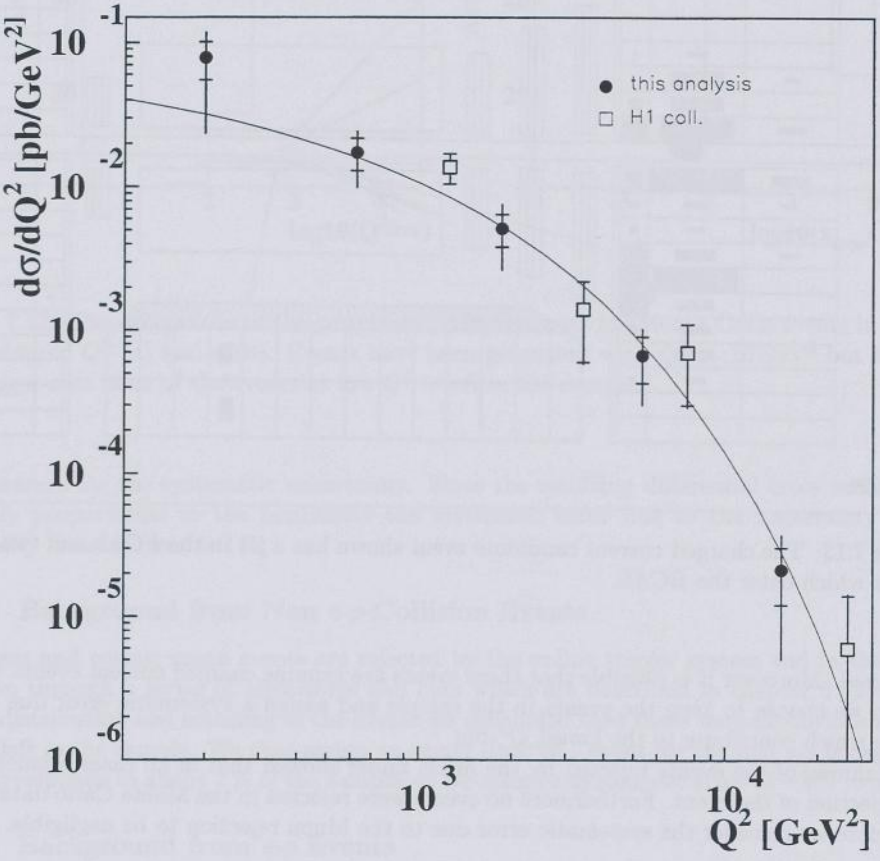

Figure 7.14: The differential cross section for e^+-p CC scattering $\frac{d\sigma}{dQ^2}$ versus Q^2. Also shown are the data obtained by *H1* for the same running period. The outer error bar represents the total error which is the quadratic sum of the systematic error and statistical error given by the inner error bar. The curve shows the theoretical expectation based on the CTEQ4D parton densities.

collaboration [43]. Agreement is good. The *H1* data do not extend as low in Q^2 as the present data due to a requirement of $P_t > 25\,\mathrm{GeV}$ imposed in the analysis.

It is interesting to note that the total visible cross section for $Q^2 > 100\,\mathrm{GeV}^2$ is

$$\sigma_{cc}(Q^2 > 100\,\mathrm{GeV}^2) = 19.0 \pm 2.72(\mathrm{stat.}) + 0.19 - 2.48(\mathrm{syst.})\mathrm{pb} \tag{7.5}$$

after acceptance correction this becomes

$$\sigma_{cc}(Q^2 > 100\,\mathrm{GeV}^2) = 37.4 \pm 5.36(\mathrm{stat.}) + 0.38 - 4.92(\mathrm{syst.})\mathrm{pb} \tag{7.6}$$

The cross section extrapolation to $Q^2 > 1\,\mathrm{GeV}^2$ and $Q^2 > 10\,\mathrm{GeV}^2$ gives

$$\sigma_{cc}(Q^2 > 10\,\mathrm{GeV}^2) = 42.4 \pm 6.08(\mathrm{stat.}) + 0.43 - 5.58(\mathrm{syst.})\mathrm{pb} \tag{7.7}$$

$$\sigma_{cc}(Q^2 > 1\,\mathrm{GeV}^2) = 43.0 \pm 6.2(\mathrm{stat.}) + 0.44 - 5.66(\mathrm{syst.})\mathrm{pb} \tag{7.8}$$

using CTEQ4D. Given the acceptance of 50.4 % we have actually observed about half of all CC events that occurred in the running period.

In order to compare to the results obtained by the *H1* collaboration [44] we have to use the same cuts, in particular $P_t > 25\,\mathrm{GeV}$. We then find 23 events, this results in a cross section of:

$$\sigma_{cc}(P_t > 25\,\mathrm{GeV}) = 15.6 \pm 3.3(\mathrm{stat.})\mathrm{pb} \tag{7.9}$$

This is compatible with the result published by *H1* in [44] for the same running period of

$$\sigma_{cc}(P_t > 25\,\mathrm{GeV}) = 21.9 \pm 3.4(\mathrm{stat.}) \pm 2.0(\mathrm{syst})\mathrm{pb} \tag{7.10}$$

and with the result published by *H1* in [43] for the same running period of

$$\sigma_{cc}(P_t > 25\,\mathrm{GeV}) = 23 \pm 3(\mathrm{stat.}) \pm 2.0(\mathrm{syst})\mathrm{pb} \tag{7.11}$$

Bin (GeV^2)	Acceptance (%)	# Evts. (acc-corr.)	$MC - \overline{Q^2}$ (GeV^2)	$\frac{d\sigma}{dQ^2}$ (pb/GeV^2)	$\Delta\frac{d\sigma}{dQ^2}$ stat. (pb/GeV^2)	$\Delta\frac{d\sigma}{dQ^2}$ sys. (pb/GeV^2)
$10^{2.0}$	15.5	43.6	198.23	$0.78E-01$	$0.23E-01$	$+0.33E-01$
$-10^{2.5}$						$-0.50E-01$
$10^{2.5}$	55.2	30.5	622.20	$0.17E-01$	$0.44E-02$	$+0.56E-02$
$-10^{3.0}$						$-0.61E-02$
$10^{3.0}$	59.2	28.6	1845.52	$0.51E-02$	$0.13E-02$	$+0.21E-02$
$-10^{3.5}$						$-0.21E-02$
$10^{3.5}$	63.7	11.7	5331.69	$0.67E-03$	$0.24E-03$	$+0.28E-03$
$-10^{4.0}$						$-0.28E-03$
$10^{4.0}$	56.2	1.2	15156.20	$0.21E-04$	$0.91E-05$	$+0.13E-04$
$-10^{4.5}$						$-0.13E-04$

Table 7.4: For every Q^2-bin the number of events observed, the acceptance, the number of events after acceptance correction, the average Q^2 of all Monte Carlo Events in this bin, the measured differential cross section $\frac{d\sigma}{dQ^2}$ and statistical and systematical errors.

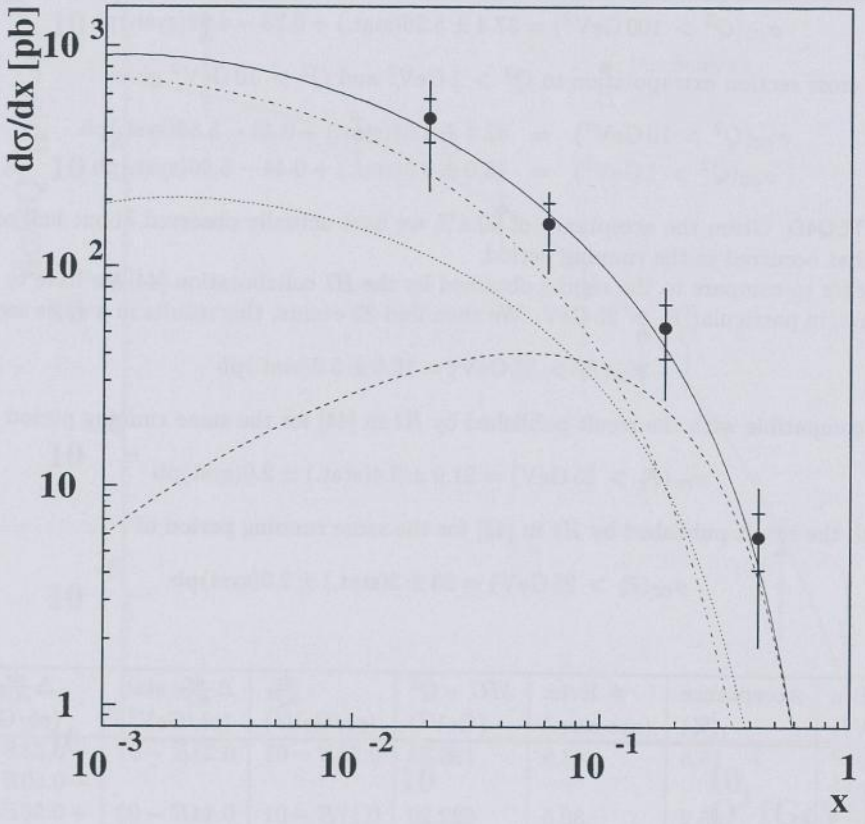

Figure 7.15: The differential cross section for e^+-p CC scattering $\frac{d\sigma}{dx}$ versus x. The outer error bar represents the total error which is the quadratic sum of the systematic error and statistical error given by the inner error bar. The full line shows the theoretical prediction based on the CTEQ4D parton densities, the dashed line the valence quark contribution, the dotted line the $(d+s)_{sea}$ quarks and the dash-dotted line the $(\bar{c}+\bar{u})$ contribution.

Bin	Acceptance (%)	# Evts. (acc-corr.)	$MC - \overline{x}$	$\frac{d\sigma}{dx}$ (pb)	$\Delta\frac{d\sigma}{dx}$ stat. (pb)	$\Delta\frac{d\sigma}{dx}$ sys. (pb)
$10^{-2.0}$	43.2	26.3	0.0199	$0.47E+03$	$0.11E+03$	$+0.23E+03$
$-10^{-1.5}$						$-0.20E+03$
$10^{-1.5}$	65.0	27.7	0.0611	$0.16E+03$	$0.38E+02$	$+0.53E+02$
$-10^{-1.0}$						$-0.50E+02$
$10^{-1.0}$	51.2	29.4	0.1804	$0.53E+02$	$0.15E+02$	$+0.24E+02$
$-10^{-0.5}$						$-0.24E+02$
$10^{-0.5}$	24.6	10.3	0.4271	$0.59E+01$	$0.17E+01$	$+0.36E+01$
$-10^{0.0}$						$-0.36E+01$

Table 7.5: For every x-bin the number of events observed, the acceptance, the number of events after acceptance correction, the average x of all Monte Carlo Events in this bin, the measured differential cross section $\frac{d\sigma}{dx}$ and statistical and systematical errors.

Table 7.5 lists the differential cross section in x and figure 7.15 shows these values together with the theoretical expectation based on the CTEQ4D parton densities.

We can see that the results are in good agreement with the theoretical expectation for charged current scattering. In figure 7.14 we also show the decomposition of the charged current spectrum in valence, $d+s$ and $\bar{u}+\bar{c}$ sea quark densities. It is interesting to see that a substantial fraction of the cross section is due to scattering off the anti-quark sea. Future larger statistics samples may be able to separate the different components.

7.8 Summary

In conclusion we have extracted the charged current cross sections in deep inelastic e^+-p-scattering. The distributions in Q^2 and x show good agreement with the expected distributions indicating that the parton densities in the proton extracted from other processes are applicable to the CC-process. The proton structure is thus understood also in terms of its decomposition in different quark flavors.

Appendix A

UCAL Readout

A.1 Introduction

The *ZEUS UCAL* readout system is described extensively in [45, 46]. In this chapter modifications to this system are detailed.

A.2 Transmission Errors

INMOS Transputers of Type T2x, T4x, T8x communicate via four serial channels with each other. The hardware transmission protocol does however not foresee any kind of check of the transmission. Tests at *NIKHEF* have shown that the transmission between transputers is very reliable [46] and so it was considered unnecessary to protect against transmission errors.

A.2.1 Transmission Error Detection

During comparisons of data produced by the calorimeter second level trigger system and its offline simulation in ZGANA [47] differences were found in the energy sums reported by both sources: The data was transported by different transputer networks to the offline database where the comparison was performed: The second level trigger network sent its results to the global second level trigger system while the readout network sent the data to the event builder.

The differences coincided with the event being processed by a particular sub-farm of the *ZEUS* third level trigger system. This meant that the data had been sent over the same transputer link by the event builder system to the third level trigger. Intensive tests showed that indeed the link was faulty and was replaced.

This error triggered the implementation of test procedures and built awareness of the problem.

Transmission errors were then also found to be the cause of various crashes of the transputer network during data-taking.

A.2.2 Transmission Error Cause and Cure

The transputer transmission errors observed by *ZEUS* were caused by a bug on the *2-TP*-Transputer modules developed for *ZEUS* [48]. The problem was traced to the transputer clock signal being outside of the specifications and all boards were modified.

A.2.3 Transmission Checks

Since transmission errors can systematically affect data, transmission error checks are put in place to detect such errors early enough.

A.2.4 Dedicated Link Tests

Programs are available to test transputer links in situ. Through these test errors can be verified.

Checksums in Offline Data, Offline DQM Tests

Calorimeter data are checked with data banks CxXOR which contain checksums on an event by event basis. The checksums are calculated using a simple XOR of all the data words. Through this checksum single bit failures can be detected. The calorimeter data quality monitoring also includes a check for transmission errors. Moreover the calorimeter reconstruction program CCRECON [49, 36] checks prior to reconstructing an event whether a transmission error occurred. If that is the case the event is not reconstructed.

The calculation of the checksums is done through transputer assembler routines which are highly optimized and perform about 30 % better than the OCCAM equivalent.

Checksums in Online Data

Transmission errors can, apart from corrupting data, cause the transputer network to crash, for example if the length of a data array is transmitted and the receiver receives an incorrect number, the receiving transputer can crash because it will find its buffers too small or will wait for the rest of the data forever. For this reason a number of control messages have been protected via checksums and the transmission will be retried if an error is detected.

Checksums of Calibration Constants

Transmission errors can have much more serious consequences if they occur with calibration constants. In such a case the calorimeter data would be systematically wrong for all events and such errors might not be detected. For this reason calibration data are checksum-protected from the time they are generated on the transputer. Also when the constants are modified on the equipment computer the checksums are tested and recalculated. Finally when they are downloaded to the *DSP* before the beginning of a new run they are checked again by the *DSP*.

Online Checks of Digital Card Output

Transmission errors can also occur when data are transported through *VME* from the digital card memory to the transputers. These errors are detected through a data consistency check which is performed on a regular basis while the system is taking data. This consistency check is possible because the *DSP* code running on the digital cards outputs both the data for the each channel to be shipped by the *CAL-DAQ* to the *TLT* but also the sum of left and right channel and timing sums to be used by the *CALSLT* (see [50, 51]). The transputer simply recalculates on a subset of the events the *CALSLT* data from the *CAL-DAQ* data and compares it to the digital card output. The test is typically performed every 100 triggers on one of the digital cards.

Transmission Errors in *UCAL SLT* Network

The calorimeter second level trigger network consists of a large network of transputers. Also here transmission errors were observed which caused the network to crash. In order to avoid these crashes checks were implemented which ensured the synchronization between transputers. It is however not possible to calculate a checksum for all data because then the throughput of the network would be compromised.

A.3 Exclusion from Readout by Event Builder

Transputers allow processes to be executed at two different priorities, the high priority processes can always interrupt low priority processes. Interrupts can be generated through the arrival of data through a link or through the *EVT* pin of the transputer or through the high priority timer.

It is however possible that a high priority process is descheduled by a low priority process. This was the case for a problem that caused the *UCAL* transputer readout network to be excluded from the run by the event builder: The event builder system distributes the *GSLT* message to all components. Those have to accept the message within a certain timeout, a few milliseconds only. Should the component not accept the data within the timeout it will be excluded from the run. This behavior of the event builder is necessary to ensure a high rate of *GSLT* decisions to be broadcast (design rate 1 kHz). In the *UCAL* case the data are broadcast through the control and switch box (*CSB*) to all *READOUT* transputers. The data are not buffered but each byte is transmitted to all transputers and only if all transputers have acknowledged the receipt an acknowledgement is sent back to the event builder. In order to ensure that the data can be received a high priority process was set up who's only task it was to buffer the data and send it to a low priority process. The high priority process sent the data through a transputer channel. This was the problem though, the low priority process, if it was not capable of receiving the message, caused the high priority process to be descheduled. The problem was only diagnosed when the *GSLT* simulator (see section B.7) was installed and then fixed by enabling a simple round-robin buffer between the high priority and low priority process.

A.4 Features added to the Readout System

A.4.1 Readout of other Subdetectors

The calorimeter readout system was extended to readout more components, *SRTD* (Small Angle Rear Tracking Detector), *PRES* (Forward and Rear Presampler), *FNC* (Forward Neutron Calorimeter), *PRT* (Proton Remnant Tagger), *BPC* (Beam Pipe Calorimeter), *SRTDFLT* (First Level Trigger of the Small Angle Rear Tracking Detector) and *BPRES* (Barrel Presampler). All these components are based on the readout of photomultipliers and use the same or only slightly modified front-end electronics as the *UCAL*. As a result of the use of one readout system for these components the cost as well as number of people necessary for maintenance is greatly reduced.

A.4.2 Testtrigger processing

The calorimeter readout code is capable of calculating the mean and r.m.s. of the readout values for testtriggers. Since most of the detector monitoring is based on these values the monitoring

task could be speeded up dramatically by calculating these values online and only transmitting the result at the end of the run.

A.4.3 Startup Procedures

The startup of the transputer network is significantly improved over older versions because the calibration constants, about 3.8 MByte of data, do not have to be downloaded. Instead the calibration constants are loaded once and stored in the *READOUT* transputer memory. Even when the transputer is rebooted at *SETUP* the data are still present and can thus be downloaded immediately. The data are checked with a *CRC* checksums. The calorimeter network setup time could be reduced from several minutes to only a few seconds.

A.4.4 *UCAL* Electronics Calibration

The calorimeter electronics calibration consists of a number of runs with different settings of the electronics. This way the pedestals and gains of each pipeline chip as well as the gain of each buffer chip can be measured. This process took up to several hours because all the data had to be written to disk and then calibration constants had to be generated. This process was significantly improved by generating the electronics calibration constants directly on the transputers. In order to do that the data had to be stored locally. On the *READOUT* transputer however with its 4 MByte of *RAM* there is not enough space. To solve this problem a system by which the memory of the adjacent "layer-1" trigger transputer could be used had to be developed. Both transputers communicate via the triple ported memory to exchange the data which is then stored in a simple way on the layer-1 trigger transputers' memory.

A.4.5 *CAL-DAQ* Monitoring Task

Some errors in the transputer programs are very difficult to debug. This is due to the fact that the communication is not reliable (see section A.2) and due to the complexity of the task to be performed. Sometimes the system stops without any indication of a reason. To improve this situation, counters were introduced at many processing steps in the system. These counters are written into *TPM*, together with counters produced by the *CALSLT* transputers. A process on the main control transputer of the network monitors the data acquisition. If no events are sent to the *EVB* for several seconds, the process asks all *READOUT* transputers to send the counters and it then analyses the counters to determine if the problem is inside the *CAL-DAQ* or somewhere else and generates appropriate warning messages.

A.4.6 Speedups

Loop Unrolling while Re-Ordering

UCAL second level trigger processing is based on the same data that are used for readout. The *LAYER-1* processing algorithm requires the data to be ordered in a certain way, but the front-end channels are not connected in the same order to the digital cards. The original algorithm foresaw the trigger processors using a double-indexed list to access the data. Since the "*READOUT* transputer" only had to process events at a rate of 100 Hz while the "trigger transputer" has to operate a 1 kHz the job was split into a reordering step performed on the "*READOUT* transputer" while the "trigger transputer" accessed the list through a single indexed list. The

reordering step however was still done using a double-indexed list. By loop-unrolling this step could be speeded up significantly.

Achieved Speed

The calorimeter readout system can send events to the event builder at a rate of 102 Hz which is more than the design rate of 100 Hz. During normal data taking this rate is not achieved however because other *ZEUS* subdetector readout systems and the third level trigger system can not keep up with that rate.

A.4.7 Data Compression

The *ZEUS* calorimeter readout data are compressed to reduce the amount of storage space used offline but also in order to improve the throughput of the higher level trigger systems. The compression leads to a reduction of a factor 5 in size without any loss of data.

A.4.8 Reverse Polish Notation Processor

For the readout of the *LED* and *LASER* components the calculation of the data required the implementation of a reverse polish notation processor. It allows the modification of the online reconstruction algorithm through downloading a parameter file which contains the formulas. These formulas are programmed using reverse polish notation.

A.4.9 Standalone Run-Control

Standalone tests of the calorimeter readout and second level trigger system require a flexible runcontrol system. This was implemented and is now part of the host transputer program. An environmental variable selects whether the host transputer uses the standard runcontrol system or the standalone system.

A.4.10 Multiple *DSP* Code Types

The *DSP* code which calculates energy and time from the samples taken by the front end system is dependent on the component read out. In order to allow several components to be read out, different versions of *DSP* code can be downloaded.

A.4.11 Begin-Of-Run Data Banks

Startup of the calorimeter readout system was delayed by downloading begin-of-run data banks from the equipment computer to the transputer network which were subsequently forwarded into the data stream. The data downloaded included a list of bad channels. This list is available though on each *READOUT* transputer through the calibration constants. So at the beginning of a run each readout transputer generates the bad channel list and enters it into the data stream.

A.5 "Event Player"

A special version of the *DSP* code was developed which uses the memory of the digital cards to be used as event store. Upon a signal the *DSP* starts to act as if it was receiving first level trigger decisions. This feature is used to do performance tests of the readout and second level trigger

network. Before starting event data can be downloaded together with the rate at which the digital cards should "play back" the data. Together with the *GSLT* simulator (see section B.7) this provides the possibility to test the *UCAL* data acquisition and second level trigger system independently of the rest of the *ZEUS* data acquisition system. The only difference is that the digital cards are running asynchronously while for normal *ZEUS* operation all digital cards receive the first level trigger at the same time. As a result during "event player" simulation, if the event player rate is higher than the rate that can be handled by the *CALSLT* some of the digital cards report a "buffer full" condition while others don't. This however does not affect the operation of the *CALSLT* or *CAL-DAQ* algorithms as they have large enough buffers to allow for the event processing on different processing elements of the same level to be out of synch.

Appendix B

UCAL Second Level Trigger

B.1 Introduction

The *ZEUS UCAL* second level trigger system is described extensively in [45, 46]. In this chapter modifications to this system are detailed.

B.2 Second Level Trigger Output

The calorimeter second level trigger calculates the following values online:

Variable Name	Type	Contents
ETotalEmc	REAL	Total Energy in EMC cells
ETotalHac	REAL	in HAC cells
CellsHitEmc	REAL	Number of Cells above threshold EMC
CellsHitHac	REAL	HAC
ETransEmc	REAL	Transverse energy EMC
PxEmc	REAL	Momentum along x-axis EMC
PyEmc	REAL	Momentum along y-axis EMC
PzEmc	REAL	Momentum along z-axis EMC
PlMinEmc	REAL	PlMin EMC
EtransHac	REAL	HAC
PxHac	REAL	HAC
PyHac	REAL	HAC
PzHac	REAL	HAC
PlMinHac	REAL	PlMin HAC
FcalTime	REAL	FCAL time
BcalTime	REAL	BCAL time
RcalTime	REAL	RCAL time
TimeFlag	INTE	Concludes CAL timing results.
NoOfClusters	BITP	number of clusters found: (4 bytes packed)

continued on next page

continued from previous page

Variable Name	Type	Contents
		byte 0: number of muon clusters,
		byte 1: number of hadron jets,
		byte 2: number of em clusters,
		byte 3: number of elec candidates
SltErrors	BITP	Bitpattern of SLT errors,
		bit 0: energies crazy,
		bit 1: timing info crazy ,
		bit 2: global sums on layer1,
		bit 3: hac precluster scan,
		bit 4: emc precluster scan,
		bit 5: precluster merging,
		bit 6: cluster cut on layer1,
		bit 7: timing algo layer1,
		bit 8: global sums on layer2,
		bit 9: cluster merge on layer2,
		bit 10: cluster cut on layer2,
		bit 11: timing algo layer2,
		bit 15: global sums on layer3,
		bit 16: cluster merge on layer3,
		bit 17: cluster cut on layer3,
		bit 18: timing algo on layer3,
		bit 19: converting to gslt,
		bit 29: GSLT-message:dont use global sums,
		bit 30: GSLT-message:dont use clusters,
		bit 31: GSLT-message:dont use the timing
ETotalFCal	REAL	Total Energy FCal
ETotalBCal	REAL	Total Energy BCal
ETotalRCal	REAL	Total Energy RCal
NoPMsFCalTi	REAL	no. of PMs used for FCal time
NoPMsBCalTi	REAL	no. of PMs used for BCal time
NoPMsRCalTi	REAL	no. of PMs used for RCal time
ETotalFEmc	REAL	Total Energy FCal EMC
ETotalBEmc	REAL	Total Energy BCal EMC
ETotalREmc	REAL	Total Energy RCal EMC
UpTime	REAL	av. time of upper regions
DownTime	REAL	av. time of lower regions
NoPMsUpTi	REAL	no. PMs used for up time
NoPMsDownTi	REAL	no. PMs used for down time
UpETotal	REAL	energy in upper regions
DownETotal	REAL	energy in lower regions
GlobTime	REAL	av. time of entire CAL

continued on next page

continued from previous page		
Variable Name	Type	Contents
NoPMsGlobTi	REAL	no. PMs used for global CAL time
FCalBPEEmc	REAL	E in FCAL Emc beampipe region
FCalBPEHac	REAL	E in FCAL Hac beampipe region
FCalBPPxEmc	REAL	Px in FCAL Emc beampipe region
FCalBPPyEmc	REAL	Py in FCAL Emc beampipe region
FCalBPPxHac	REAL	Px in FCAL Hac beampipe region
FCalBPPyHac	REAL	Py in FCAL Hac beampipe region
FCalBPEtEmc	REAL	Et in FCAL Emc beampipe region
FCalBPEtHac	REAL	Et in FCAL Hac beampipe region

Table B.2: List of values calculated for every event by the *ZEUS* calorimeter second level trigger system.

B.2.1 Spark Cut

The calorimeter second level trigger algorithm data are used to reject events which have been triggered on the first level by a sparking photomultiplier.

Two algorithms have been developed:

1. The first algorithm makes parasitic use of the number of photomultipliers used in the timing averages and the clustering algorithm: In order to contribute to the timing averages a channel has to report more than 200 MeV of energy. If only a single channel exceeds this value and if there is only a single calorimeter cluster with only a single cell to be found then this event is classified as spark event.

2. The second algorithm requires that the event was triggered by the calorimeter only, there are no cells with both *PMT*s reporting more than 0.2 GeV and that there is only one cell with energy greater than 2 GeV. In addition it is required that the energy in the calorimeter after removing the cell considered as the spark must be low.

B.2.2 Cosmic Up-Down Timing Cut

The algorithm described in 5.4.1 required calculation of separate timing sums for the upper and lower half of *BCAL*. The values are calculated at the *CALSLT*.

B.3 Speedups and Error Handling

B.3.1 Error Handling

During data taking with beams it is possible that large events trigger overflows in the global sums because they are calculated as integer values with a limited range.

The standard `OCCAM` compiler provides several output modes: The "halt-on-error" mode produces code that, when an error condition occurs, will halt the processor and raise the error flag. The process can then be debugged. The "undefined" mode still recognizes an error condition and a flag is raised, but the processor continues, the results of arithmetic operations are undefined.

If the programs are compiled in "halt-on-error" mode the data acquisition system will stop with loss of valuable beam time as a consequence, so this mode should not be used for data taking.

The programs on the *CALSLT* were modified such that they can be compiled in "undefined" mode but when an error occurs a flag in the output to the *GSLT* indicates that an overflow had occurred for this event and the event is then forced to be stored by the *GSLT*. This way the data acquisition system continues running and even though the data in the global sums is unreliable, the events are saved.

B.3.2 Extend Processing on more Processors

The *CALSLT* processing of a single event consists of two steps: First the global sums are added up and then the clusters are created and combined. Several transputers in the *CALSLT* network were only used to transport data, they just received the data from *LAYER-1* processors and sent them through triple port memory (*TPM*) to the adjacent *LAYER-2* processor where the data was processed before being sent of to the *LAYER-3* processor. Also the *LAYER-3-MON* processor was only used in that role. It is possible however, to add up the global sums on that "communicator" transputer and just send one array of global sums to the other transputer instead of four arrays.

B.3.3 Overlapped Processing

As described above the processing can be split into two steps, the adding up of global sums and the cluster processing. For the transputers in layers 2 and 3 a further improvement is possible: Here one can process the data from the lower layer as soon as it arrives and not only when all data for an event from all lower layer transputers has arrived. This modification did not improve the processing speed but the latency with which the decision arrived at the *GSLT* could be improved by 0.2 ms.

B.4 Enhancements

B.4.1 Monitor *CALSLT* Processing through *TPM*

The monitoring of the *CALSLT* processing is done using the monitoring system of the *CAL-DAQ* (see section A.4.5): Event counters at several points in the processing are stored in the *TPM* and read out by the readout transputer if the data acquisition system stops sending events to the *EVB* for several seconds.

B.4.2 Send *CALSLT* data through *CAL-DAQ*

The data produced by the *CALSLT* was previously sent through the *GSLT* into the data stream. This worked without any problem but had the disadvantage that, if the data format was changed programs also had to be modified in the *GSLT*. Moreover the output data was limited and there was no way to send data for special events into the data stream. The programs have been modified such that the data is stored in the *TPM* of the trigger transputer and picked up by the readout transputer in the same crate.

B.5 ZGANA simulation

The ZGANA simulation of the *CALSLT* network was re-developed and made to agree fully with the online programs. This development led to the discovery of transmission errors (see A.2) and allowed detailed studies of the algorithms.

B.6 Standalone *CALSLT*

The debugging of new online programs for the *CALSLT* requires access to the *CAL-DAQ*. Since *CAL-DAQ* is used by many other sub-detectors of *ZEUS* (see section A.4.1) debugging proved to be difficult to coordinate. A standalone version of the *CALSLT* that runs on a single transputer was developed which acts as a framework for the *CALSLT* algorithms: The algorithms are exactly the same that are run on the *CALSLT* online transputer network, but the data transport routines are replaced by the framework.

B.7 Simulated *GSLT*

The debugging and improvement of the *CALSLT* and *CAL-DAQ* required access to the *GSLT* and *EVB*: Decision data had to be sent to the *GSLT* and were re-distributed to the *CAL-DAQ* via the *EVB*. This proved difficult because both the *GSLT* and *EVB* are central components which are used by many other *ZEUS* sub-detectors. The *UCAL* transputer network was therefore extended to include a simulation of the *GSLT* and *EVB* functions. This was achieved by introducing a new *2-TP* transputer, the *SIM-GSLT* transputer, and routing the connections to the *GSLT* and from the *EVB* through the *CAL-DAQ* control and switch boxes. The resulting system can then, if the "event player" *DSP* code is used, run completely independently of the rest of the system.

If the standalone runcontrol system is used (see section A.4.9) the fraction of events that are rejected by the simulated *GSLT* transputer can be changed during running by simple keyboard commands.

The development of this *GSLT* simulator led to the removal of the "CAL-excluded-by-EVB" error condition (see section A.3) and was used as a prototype for the *GSLT* standalone simulation environment (see section C.2). Furthermore it was possible to improve the performance of the algorithms of both the *CALSLT* and *CAL-DAQ* systems.

Appendix C

Global Second Level Trigger

C.1 Introduction

The *ZEUS GSLT* system is described extensively in [45, 52, 53]. In this chapter modifications to this system are detailed.

C.2 Standalone Simulation Environment

The *GSLT* receives data from many components and sends decisions to the event builder (*EVB*). Prior to the change described here testing of the programs running in the *GSLT* was difficult because it required the components to send the data which had two major disadvantages: First it was impractical because it required that the components were online and functioning, second not all components were actually able to send pre-defined test data and so the *GSLT* would usually only receive empty events or cosmic events at best. With such data however, not all algorithms can be tested correctly.

It was therefore decided to build an environment in which the *GSLT* could be tested standalone and in which the arbitrary data could be downloaded. The modification consisted of routing the connection of the input modules to the filters through the *GSLT* internal switch. Moreover, a previously unused transputer was connected to the switch.

After the modification data can be downloaded to the new transputer and are sent to the filters through the switch. With this facility the verification of *GSLT* online programs are much improved as arbitrary data, for example a mix of previously acquired data or Monte Carlo data can be downloaded and the algorithm response can be compared to the expectations. Another advantage of the modification is that now the filter algorithms can be debugged after a crash: Before the modification the filter transputers were not accessible for debugging.

References

Bibliography

[1] F. Halzen and A.D. Martin, "Quarks and Leptons", Wiley (1984).

[2] G. Altarelli, G. Parisi, "Asymptotic Freedom in Parton Language", *Nucl.Phys.B126:298,1977.*
Yu. L. Dokshitzer, *Sov.Phys. JETP 46(1967)641*;
L. N. Lipatov, *Sov. J. Nucl. Phys. 20 (1975) 94*;
V. N. Gribov, L. N. Lipatov, "Deep Inelastic e p Scattering in Perturbation Theory", *Sov.J.Nucl.Phys.15:438-450,1972.*

[3] M. Vreeswijk, "Measurement of the Structure Function F2 and the Gluon Density of the Proton", University of Amsterdam, 1996, Ph. D. Thesis.

[4] M. Glück, E. Reya, A. Vogt, "Dynamical Parton Distributions of the Proton and Small x Physics", *Z.Phys.C67:433-448,1995.*

[5] J. Botts et al, "CTEQ Parton Distributions and Flavor Dependence of Sea Quarks", *Phys.Lett.B304:159-166,1993.*

[6] A.D. Martin, R.G. Roberts and W.J. Stirling, "Parton Distributions of the Proton", *Phys.Rev.D50(1994)6734-6752.*

[7] H.Plothow-Besch, "PDFLIB: The Parton Density Functions Library", *CERN-W5051(1997).*

[8] Birmingham-CERN-Imperial Coll.-MPI(Munich)-Oxford-University Coll. Collaboration (G.T. Jones et al.), "A Measurement of the Proton Structure Functions from Neutrino - Hydrogen and Anti-Neutrino - Hydrogen Charged Current Interactions", *Z.Phys.C44:379,(1989).*

[9] CHARM Collaboration (J.V. Allaby et al.), "Total Cross-Sections of Charged Current Neutrino and Anti-Neutrino Interactions on Isoscalar Nuclei", *Z.Phys.C38:403-410,(1998).*

[10] P.S.Auchincloss et al., "Measurement of the Inclusive Charged Current Cross-Section for Neutrino and Anti-Neutrino Scattering on Isoscalar Nucleons", *Z.Phys.C44:379,(1989).*

[11] C.F.Weizsäcker, *Z.Phys.88(1934)612*;
E.J.Williams,*Phys.Rev.45(1934)729*;
S.Frixione et al., *Phys.Lett.B319(1993)339.*

[12] H1 Collaboration, I.Abt et al., "Measurement of the Total Photon Proton Cross section and its Decomposition at 200 GeV Centre of Mass Energy", *Z.Phys. C69 (1995) 27.*

[13] S. Bentvelsen, J. Engelen and P. Kooijman, "Reconstruction of (x,Q^2) and extraction of structure functions in neutral current scattering at HERA", *Proc. Workshop on Physics at HERA, vol. 1(1992)23.*

[14] F. Jacquet and A. Blondel, *Proceedings of the study of an ep facility for Europe, ed. U. Amaldi, 79/48(1979)391.*

[15] H1 Collaboration, I.Abt et al., "The H1 Detector at HERA", *DESY preprint, 93-103(1993).*

[16] ZEUS Collaboration, M.Derrick et al, *Phys.Lett.B293(1992)465.*

[17] ZEUS Collaboration, M.Derrick et al., "The ZEUS Detector, Status Report 1993", DESY (1993).

[18] A.Freidhof, A.Caldwell, G.Field, L.Hervas, J.N.Lim, B.Oh, S.Ritz, T.Tsurugai, R.Yoshida, "The time calibration of the ZEUS Calorimeter", *ZEUS internal note 93-021 (1993).*

[19] J. Krüger, "The Uranium Scintillator Calorimeter for the ZEUS Detector at the Electron-Proton Collider HERA - The Heart of ZEUS", January 1992. Habilitationsschrift Universität Hamburg, published as Internal Report *DESY F35D-92-02 (1993).*

[20] H. Bethe and W. Heitler, *Proc.Roy.Soc.A146(1934)83.*

[21] J. Andruszków et al., "First Measurements of HERA Luminosity by ZEUS Lumi Monitor", *DESY 92-066, May 1992.*

[22] K. Piotrzkowski, "Experimental Aspects of the Luminosity Measurement in the ZEUS Experiment", *DESY-F35D-93-06, Oct 1993, Ph.D. Thesis.*

[23] K. Piotrzkowski and M. Zachara, "Determination of the ZEUS Luminosity in 1994", *ZEUS internal note 94-176 (1994).*

[24] K. Piotrzkowski and M. Zachara, "Determination of the ZEUS Luminosity in 1994", *ZEUS internal note 95-138 (1995).*

[25] K. Charchula, G.A. Schuler, H. Spiesberger, "Combined QED and QCD Radiative Effects in Deep Inelastic Lepton - Proton Scattering: The Monte Carlo Generator DJANGO6",*Comput.Phys.Commun.81:381-402,(1994)*

[26] A. Kwiatkowski, H. Spiesberger, H.J. Mohring, "HERACLES: An Event Generator for e p Interactions at HERA Energies Including Radiative Processes: Version 1.0", *Comput.Phys.Commun.69:155-172,(1992)*

[27] G. Ingelman, "LEPTO", *Proc. of the Workshop on Physics at HERA vol. 3, (1992)1366.*

[28] G. Gustafson, "Dual Description of a Confided Color Field", *Phys.Lett.175B:453,(1986)*; G. Gustafson, U. Pettersson, "Dipole Formulation of QCD Cascades", *Nucl.Phys.B306:746,(1988)*;
B. Andersson, G. Gustafson, L. Lönnblad, "Gluon Splitting in the Color Dipole Cascades", *Nucl.Phys.B339:393-406,(1990).*

[29] L. Lönnblad, "ARIADNE Version 4: A Program for Simulation of QCD Cascades Implementing the Color Dipole Model", *Comput.Phys.Commun.71:15-31,(1992).*

[30] B. Andersson, G. Gustafson, B. Söderberg, "A General Model for Jet Fragmentation", *Z.Phys.C20:317,(1983).*

[31] T. Sjöstrand, "High-Energy Physics Event Generation with PYTHIA 5.7 AND JETSET 7.4",*Comput.Phys.Commun.82:74-90,(1994).*

[32] "MOZART - Zeus Detector Simulation", *ZEUS internal document.*

[33] R. Brun et al., "GEANT", *CERN DD/EE/84-1(1984).*

[34] F. Chlebana, "Description of the ZEUS Global Second Level Trigger in 1994", *ZEUS internal note 94-102 (1994).*

[35] D. Bandyopadhyay, "MUTRIG: A Third Level Trigger Muon Finder", *ZEUS internal note 93-013 (1993).*

[36] P. de Jong, "The Measurement of the Hadronic Energy Flow and Jet Production with the ZEUS Calorimeter in Deep Inelasitc Scattering Events at HERA", University of Amsterdam, (1993), Ph.D. Thesis.

[37] F. James, M.Roos, "MINUIT function minimization and error analysis", *CERN-D506, (1992).*

[38] Leslie Lamport, "LaTeX: A Document Preparation System", Addison-Wesley Publishing Company, 2nd edition, 1994.

[39] "VRML97, Virtual Reality Modeling Language", *International Standard ISO/IEC 14772*

[40] R. Sinkus, H. Abramowicz, "Electron Identification with Neural Networks at ZEUS", *ZEUS internal note 93-117 (1993).*

[41] W. Dorth, "LAZE", *ZEUS internal note 91-069 (1991).*

[42] A. Fuertjes, "Calibration of the ZEUS Forward and Rear Calorimeters with Muons.", University of Hamburg, 1993, Ph.D. Thesis, published as Internal Report *DESY - F35D-93-03 (1993).*

[43] H1 Collaboration, T.Ahmed et al., "Measurement of the e+ and e- induced charged current cross sections at HERA", *Z.Phys.C67(1995)565.*

[44] H1 Collaboration, I.Abt et al., "First Measurement of the Charged Current Cross Section at HERA", *Phys.Rev. B324(1994)241.*

[45] S. J. de Jong, (1990), University of Amsterdam, Ph.D. Thesis.

[46] H. van der Lugt, "The Data-Acquisition and Second Level Trigger System for the ZEUS Calorimeter", University of Amsterdam, (1993), Ph.D. Thesis.

[47] "ZGANA", *ZEUS internal document.*

[48] H. Boterenbrood et al., "A two-transputer VME module for data acquisition and on-line event selection in ZEUS", *Nucl.Instrum.Meth.A332:263-268,1993*

[49] M. de Kamps, "Diffractive Vector Meson Production in Deep Inelastic Scattering", (1997), University of Amsterdam, Ph.D. Thesis.

[50] Steve Ritz, "DAQ4.DSP: The DSP Code for Taking Data with the ZEUS Calorimeter", *ZEUS internal note 92-070 (1992).*

[51] Steve Ritz, "DAQ5.DSP", *ZEUS internal note 92-076 (1992).*

[52] H. Uijterwaal, "The Global Second Level Trigger for ZEUS", University of Amsterdam, (1992), Ph.D. Thesis.

[53] R. van Woudenberg, "Study of charm production at HERA using the ZEUS detector", University of Amsterdam, (1995), Ph.D. Thesis.

[54] S. Fisher and P. Palazzi, "The ADAMO data system, Programmers manual, Version 3.2" (1992).

[55] Eds. L. S. Brown, D. L. Nordstrom, "Monte Carlo Techniques", *Phys.Rev.D50(1994)1283.*

Summary

In this thesis we have shown a first analysis of charged current positron proton collision events at *HERA* using the *ZEUS* detector. *HERA* extends the previously measured region for CC deep inelastic scattering by more than three orders of magnitude. Since the cross section for the CC DIS interaction is very small compared to the cross section for other processes at *HERA*, the selection of charged current events poses the biggest challenge in this analysis. In the running period used for this analysis, only about 98 events with $Q^2 > 10\,\mathrm{GeV}^2$ were expected. This number has to be compared to the total number of events triggered by the *ZEUS FLT* during that period ($\sim 1.07 \times 10^9$). The task was therefore to design a selection algorithm that finds those events with high efficiency and purity. The main selection trigger for CC events is based on the large missing transverse momentum $\not{P}_t$ of those events which is due to the final state scattered neutrino that escapes undetected. This is one of the few "selection" cuts used to select CC events. Most other cuts were developed using the strategy to first identify a source of background and then reject this source with a specially designed cut: On the trigger level the rejection of background events is mostly based on event timing and global event properties, while the offline selection employs more sophisticated cuts. An important source of background is due to proton beam-wall collision events which were rejected using the fact that for such events many charged particles emerge from a vertex at the beam-wall. Another important source of background stems from cosmic or halo muon events overlapping with beam gas or genuine positron proton collision events. These events were rejected by a muon finder that was specifically developed for this analysis. It is based on identifying the characteristic patterns of energy deposit in the detector caused by traversing muons.

The two sources of background from positron proton collisions, from NC and PHP events are due to the fact that for such events, a mismeasurement of the final state, though rare, combined with the much larger cross section, results in background that is as large as the CC signal. We reject these events by cuts on $(E_{tot} - P_z)$ for NC and $\frac{P_t}{E_t}$ for PHP respectively.

We finally end up with an event sample of 49 events which represents about 50 % of the total number of CC events that occurred in *HERA* at the *ZEUS* interaction point. The efficiency of 50 % is a very good value that has been achieved owing to our careful selection procedure, that allows us to employ a rather low $\not{P}_t$ cut.

The distributions of the differential cross section for x and Q^2 show good agreement with the theoretical prediction based on standard model weak interaction cross section calculations and the CTEQ4D parameterization of the parton density functions. The measurement also agrees with the data from *H1* but extends to much lower Q^2 ($Q^2 > 100\,\mathrm{GeV}^2$ compared to $Q^2 > 625\,\mathrm{GeV}^2$ at *H1*).

With these results *ZEUS* has measured at Q^2 values previously unexplored by other experiments. We have also seen that the parameterizations of the parton density functions which are extracted from NC DIS interactions also give reliable results for CC DIS, where only a subset of

the quarks participate in the interaction.

This thesis also demonstrates that *ZEUS* can be used to produce results for very low cross section physics which will allow future measurements of exotic low cross section processes.

Samenvatting

In dit proefschrift presenteren wij de eerste analyse van geladen stroom gebeurtenissen in positron proton verstrooiing bij de *HERA* versneller, gemeten met de *ZEUS* detector. Bij *HERA* is de beschikbare faseruimte, waarin metingen aan geladen stroom diep inelastische verstrooiing gedaan kunnen worden, meer dan drie ordes van grootte groter dan bij voorgaande experimenten. In deze analyse is de grootste uitdaging het selecteren van de gewenste gebeurtenissen, aangezien de werkzame doorsnede voor geladen stroom diep inelastische verstrooiing vele malen kleiner is dan voor andere processen, die plaatsvinden bij *HERA*. In de periode, waarin data voor deze analyse werden vergaard, werden in totaal slechts 98 gebeurtenissen verwacht. Dit moet vergeleken worden met de bijna twee miljard gebeurtenissen, die de *ZEUS* eerste niveau trigger in dezelfde periode registreerde. De algoritmen, waarmee de geladen stroom gebeurtenissen werden geselecteerd, dienden daarom niet alleen zeer efficient te zijn maar moesten tevens een zeer grote onderdrukking van de achtergrond opleveren.

Het belangrijkste criterium voor de selectie van geladen stroom gebeurtenissen is de grote ontbrekende transversale impuls, veroorzaakt door het ontbreken van het geproduceerde neutrino in de gemeten eindtoestand. De snede op deze grootheid is een van de weinige gebruikte snedes, die de specifieke topologie van de geladen stroom gebeurtenissen selecteert. De meeste andere snedes zijn ontworpen door eerst een bron van achtergrond te identificeren en deze dan met een speciaal toegesneden algoritme te onderdrukken. Op het trigger niveau werd voornamelijk informatie van de tijdsregistratie van de gebeurtenissen gebruikt om achtergronden die niet met positron proton verstrooiing overeenkwamen te verwijderen. Ook werden globale kenmerken van de gebeurtenissen, op hogere trigger niveaus telkens met toenemende precisie gereconstrueerd, gebruikt om de geladen stroom gebeurtenissen te selecteren. In de "offline" analyse werden meer verfijnde algoritmen gebruikt om de achtergrond te onderdrukken. Zo bleken de interacties van protonen met het materiaal van de bundelpijp een belangrijke bron van achtergrond te zijn. Deze achtergrond werd onderdrukt op basis van het aantal sporen dat niet consistent was met een oorsprong op de positie waar de positron en proton bundels met elkaar botsen. Een volgende belangrijke bron van achtergrond bleken "halo" en cosmische muonen te zijn, die samen met een gewone (niet geladen stroom) gebeurtenis geregistreerd werden. Hiervoor werd een speciaal programma ontwikkeld om het specifieke patroon van een muon binnen een gewoon gebeurtenis te herkennen.

Twee andere bronnen van achtergrond werden gevormd door neutrale stroom diep inelastische verstrooiing en fotoproductie. Deze beide processen produceren alleen achtergrond voor geladen stroom gebeurtenissen doordat de eindtoestand niet volledig of foutief gereconstrueerd wordt. De waarschijnlijkheid hiervoor is zeer klein, maar, omdat de werkzame doorsnedes van deze processen aanzienlijk groter zijn dan die voor geladen stroom interacties leveren deze processen toch achtergronden op van dezelfde orde van grootte als het signaal van de geladen stroom. De neutrale stroom kan onderdrukt worden door te eisen dat het verschil van de totale

energie en de z-component van de impuls van de gebeurtenis aanzienlijk verschilt van dat in de begintoestand. De fotoproductie wordt verwijderd met een snede op de verhouding van de transversale impuls tot de totale transversale energie.

Uiteindelijk resteren er 49 gebeurtenissen, hetgeen ongeveer de helft van alle geproduceerde geladen stroom gebeurtenissen is. Deze zeer grote efficientie van 50% is te danken aan de zeer secure selectie procedure, die ons in staat stelt een nogal lage ontbrekende transversale impuls snede toe te passen.

De verdelingen van de differentiële werkzame doorsnedes als functie van zowel de vierimpulsfractie, x, als de vierimpulsoverdracht, Q^2, zijn in zeer goede overeenstemming met voorspellingen gebaseerd op berekeningen met behulp van het standaard model van electro-zwakke wisselwerkingen en de CTEQ4 parametrisatie van de quark dichtheden in het proton. De metingen komen eveneens overeen met de metingen van *H1* (het andere botsende-bundelexperiment bij *HERA*), met dien verstande dat onze data bij veel lagere waarden van Q^2 ($Q^2 > 100$ GeV^2) beginnen dan die van *H1* ($Q^2 > 625$ GeV^2) en onze analyse dus een groter gebied in Q^2 bestrijkt.

Deze metingen van geladen stroom lepton-proton verstrooiing bestrijken een gebied in Q^2, waar niet eerder metingen zijn gedaan. Het blijkt uit deze metingen, dat de parametrisaties van quark dichtheden in het proton, die voornamelijk uit metingen aan neutrale stroom interacties zijn geëxtraheerd, betrouwbaar zijn voor het voorspellen van de geladen stroom interacties, waaraan de quarks op een andere wijze bijdragen dan aan neutrale stroom interacties.

Dit proefschrift laat tevens zien dat, indien een zeer gerichte analyse wordt uitgevoerd, het *ZEUS* experiment in staat is metingen te doen aan processen met zeer kleine werkzame doorsneden. In de toekomst zullen wellicht meer exotische processen eveneens onderzocht kunnen worden.

Acknowledgements

First I wish to thank my wife Elaine whose strength and love were integral to my recovery and completion of this thesis. I would like to thank my parents for their continuing support during my education. Special thanks to Denise for all she has done.

I would also like to thank my thesis advisor, Prof. Dr. J. J. Engelen, who gave me the opportunity to take part at an exciting time in *ZEUS*. He also continuously supported me throughout the analysis and writing of this thesis with many valuable comments and moral support.

Furthermore I wish to thank Dr. P. M. Kooijman for his inexhaustive efforts, patience and constructive help through my time at *NIKHEF* and throughout the writing of this thesis.

My thanks also extend to the current and past members of the *NIKHEF ZEUS* group, in particular the group leader Dr. H. Tiecke who has supported my work continuously, and Dr. H. van der Lugt, Dr. R. van Woudenberg, Dr. M. de Kamps, Dr. M. Vreeswijk and A. van Sighem for the many fruitful discussions we had. I would also like to thank Dr. L. Wiggers and Dr. J. Vermeulen for their valuable guidance and Dr. R. Klanner, Dr. R. Yoshida, Dr. S. Ritz, Dr. A. Caldwell and Dr. J. Labs for their support and help during my time at *DESY*.

I wish to express thanks to H. Boterenbrood professionally for his excellent collaboration and personally to him and Anna, his wife, for their friendship and help.

I would like to thank Dr. T. Reichel for his friendship, humor and inspiration.

I gratefully acknowledge the work of many people who have built and run the *HERA* machine and *ZEUS* detector. I realize that as member of the *ZEUS* collaboration my success is built on the work of the collaboration and its members whose contributions often exceed the call of duty.

I would also like to thank Prof. Dr. A. Rubbia, Dr. S. Cittolin, Prof. Dr. G. Zech for their understanding and support.

There are many people I have not mentioned but whose debt I am in for their professional and personal contributions that made my time at *NIKHEF* and *DESY* memorable and successful.